Towards interferometry with ultra-cold atoms in crossed optical waveguides

Richard Peter Brotherton Moore

Department of Physics
University of Liverpool

Thesis submitted in accordance with the requirements of the University of Liverpool for the degree of Doctor in Philosophy

December 2018

Acknowledgements

There are so many people to thank, without them this thesis would not exist. Firstly I would like to thank Jonathon Coleman for his continued hard work in making the entire project viable. I also want to thank Yuri Ovchinnikov for his constant supervision, guidance and advice. To Vera, Carl, Jonathan and all the others who helped me along the way I am truly thankful. Finally to Laura, for all of her love and endless support along the way.

Abstract

The goal of this thesis is to study a novel approach towards all-optical continuous waveguide interferometers based on quasi-Bragg waveguide beam splitters. The Bragg beam splitter for matter waves is comprised of a periodic lattice produced by partial or full interference between two Gaussian laser beams and are used as waveguides for ultra-cold atoms. In the experimental conditions, where both waveguides have wide and deep potentials, atoms are unable to split from a single lattice. Instead, several spatially separated regions of the optical lattice are required, fulfilling the Bragg condition. This thesis will present clear evidence of the detection of discrete quantised momentum states of the atoms, created from a process of ultra-cold atoms undergoing interference in the single arms of a Michelson interferometer. A detailed investigation of the different regimes of the splitter has been completed by varying the initial atom velocity and the amplitude of the optical lattice. The findings from the study have produced optimal parameters where the splitting ratio of the atoms between the two waveguides can be finely controlled by the amplitude of the lattice within certain limits.

A Michelson interferometer configuration is used to test the coherence of the atoms by decelerating them after splitting in the lattice. The return velocity of atoms is set to be equal to the initial velocity and the two clouds are recombined using the original lattice. A sinusoidal oscillation of the atomic momentum between the two output ports of the beam splitter is visible. However, only interference in single Michelson interferometer arms has been observed. The reasons are discussed in detail along with plans to move towards an all-optical design.

Table of contents

List of figures

Chapter 1

Introduction

Interferometry as a method to measure physical properties has existed for over 130 years, originally interfering light [1]. More recently light interferometry was used to detect the existence of gravitational waves in a landmark experiment [2]. Many other particles also exhibit interferometry effects including electrons [3], neutrons [4], neutral atoms [5, 6] and molecules [7]. Major advances in laser technology has enabled a rapid rise in ultra-cold cooling of neutral atoms [8, 9], paving the way for their use in the definition of the second [10] through measurement of atomic transition frequencies of caesium [11]. Additionally, neutral atoms act as test masses for applications such as gravity gradiometry [12] and inertial sensors [13–15]. More recently interferometry of large molecules [16] begins to blur lines between classical and quantum physics and recent successes in gravitational wave detection has led to plans to develop a similar detector using atom interferometry [17].

1.1 Laser Cooling of Atoms

The first lasers were developed in 1960 [18] and have observed remarkable technological advances since. It is partly due to the rapid rise in laser technology that laser cooling has become such a ubiquitous method of rapidly cooling atomic samples. Lasers are now obtainable at a multitude of wavelengths with ever-increasing stability and intensity allowing the hyperfine structures of many different atom species to be probed and subsequently cooled.

One of the first ideas to cool atoms using the radiative pressure of resonant laser light to excite hyperfine transitions was developed by Ashkin in 1978 [19]. In the same year the first experimental evidence of laser cooling was published using Mg atoms held in a Penning trap [20]. Deceleration of an atomic beam of neutral atoms [21, 22], now more commonly referred to as a Zeeman slower, represented the first attempt to create a closed loop cooling transition sequence using sodium atoms. Later the introduction of an optical molasses [23] using orthogonal pairs of equal intensity collimated laser light proved that atoms could be cooled far below the Doppler limit, thought at the time to be a limiting factor to the minimum temperature obtainable.

1.2 Trapping Ultra-Cold Atoms

Relatively recent advances in atom interferometry are a direct result of new techniques to rapidly trap and cool large samples of atoms. Spontaneous absorption and emission of resonant light from laser beams provides a cooling effect and first implemented as an optical molasses [24] and magnetic trap [25] and paved the way for the introduction of the Magneto-Optical Trap (MOT) [26] which is almost ubiquitous in modern atom interferometers. Subsequently, it is commonly referred to as the workhorse of laser cooling experiments due to its ability to provide a robust source in excess of 10^{10} cold atoms at a temperature $T \simeq 100\,\mu\text{K}$ with densities in excess of $10^{10}\,\text{atoms}/\text{cm}^3$.

Further cooling of atoms is achieved using the optical dipole trapping force. The coherent interaction of the electro-magnetic field component of a laser beam induces an electric dipole moment in the atoms [27]. The force is conservative as a result of coherent scattering by absorption and emission of photons in an inhomogeneous light field. This process causes atomic energy levels of the atoms to be shifted and is known as the ac-Stark effect. For laser light far detuned to the red of the atom's resonant frequency, atoms are attracted to areas of high intensity and a trapping potential is formed. The first example of such a trap could only hold 500 sodium atoms for a period of several seconds using a single, tightly focused red detuned laser beam [28]. Later, a far-off-resonance trap (FORT) used a single, linearly polarised focused laser beam detuned from the atomic transition [29] to trap up to 10^4 Rb atoms from a MOT containing 10^6 atoms. The small transfer efficiency results from the small spatial overlap of the dipole beam to the atoms in the MOT owing to the low volume of the dipole trap.

Three main trap types using red detuned lasers have been developed. Already mentioned are the focused-beam traps that use a single laser beam to trap atoms at its focus. Standing-wave traps use two counter-propagating beams to axially confine atoms along the produced standing-wave and have been used to trap individual atoms [30]. Crossed-beam traps use two or more laser beams all focused and intersecting at their focus and are commonly used to create an all-optical Bose-Einstein Condensate (BEC) [31].

1.3 Bose-Einstein Condensation

The concept of a cloud of bosonic particles all descending into the same quantum state when cooled dates back to 1924 when Bose built on the theory of Planck's law of black-body radiation [32]. Einstein expanded the idea further [33] to include matter, eventually developing into the idea of a Bose gas controlled by Bose-Einstein statistics. They concluded that any boson below a critical temperature T_c would naturally fall into the lowest quantum energy state. Crucially the value of T_c is greater than 0. However, the practicalities of cooling a sample to sub-microkelvin temperatures at the time was unthinkable and no further work was considered until 1938 when London theorised that superfluidity in ^{4}He is a consequence of Bose-Einstein statistics [34]. A definitive proof is described by Bogolubov in 1946 [35] that overcomes previous issues where inter-particle collisions were assumed to prevent the formation of a Bose-Einstein gas through the application of a mean field theory. A BEC was first experimentally realised in 1995 independently by two separate groups [36, 37] for which Cornell, Ketterle and Wieman shared the Nobel prize in 2001.

Using the theory of ideal gases, the ground state becomes macroscopically populated as the de Broglie wavelength increases close to the mean separation between particles. The de Broglie wavelength is given as

$$\lambda_{dB} = \left(\frac{2\pi\hbar^2}{m k_B T} \right)^{1/2}, \tag{1.1}$$

where m is the mass of a single particle and T is the temperature. At the critical temperature $T = T_c$ where particles begin to macroscopically occupy the ground state the corresponding phase space density is defined as

$$D = n\lambda_{dB}^3 = 2.612\,, \tag{1.2}$$

where n is the number density of the particles. To achieve a sufficient phase space density cooling of the particles was required. The first experiments used cryogenic techniques combined with magnetic field trapping and evaporative cooling techniques to trap 10^9 hydrogen atoms in a BEC [38]. The rapid development of laser cooling also led to the development of optical traps to cool alkali atoms such as ^{87}Rb and ^{23}Na into a BEC which led to the aforementioned Nobel prize. Other alkali atoms such as ^{7}Li [39] and ^{41}K [40] were observed soon after. More recently a BEC has been developed in atom species with two valence electrons such as ^{174}Yb [41] and ^{84}Sr [42] whilst rare isotopes are also shown to condense to a BEC [43]. Larger particles are also able to reach a condensate, with a molecular BEC created in 2003 [44]. Despite the wide variety of atom species available to condense into a BEC, this experiment uses ^{87}Rb as an atom source. Rubidium is chosen primarily because its behaviour when trapping is well understood from many previous experiments. In addition, there are a large range of lasers operating within the transition wavelength at 780 nm from the rapid rise in diode lasers, making ^{87}Rb and ^{85}Rb trapping more attractive.

The large collection of BECs attained worldwide has led to many wide ranging applications. The development of an atom laser from a BEC was quickly realised through the continuous extraction of atoms, both in continous-wave (cw) [45] and pulsed configurations [46]. Additionally, a BEC has been shown to exhibit interference when split and allowed to recombine using the notion of painted potentials. A time averaged optical dipole force is made using a rapidly moving laser to create a confining potential in the shape of a circular waveguide [47, 48], potentially leading to applications in inertial navigation [49]. Production of a BEC in a microgravity environment is also desirable to enable longer interrogation times, leading to higher sensitivity measurements. Initially, tall buildings such as the ZARM drop tower in Bremen [50] were used to maximise the free-fall time. The tower allows for a 146 m drop, enabling 9.3 s of free-fall when experiments are launched vertically upwards. In early 2017 the first demonstration of a BEC in space using a sounding rocket was performed [51], delivering a microgravity environment of 6 minutes in which a BEC was formed and was coherently split using Bragg diffraction, despite large external temperature fluctuations. On Earth increasing interrogation time T can only be achieved by creating a larger free-fall environment but as $T \propto \sqrt{d}$ where d is the distance travelled, the total length of free-fall interferometers rapidly becomes infeasible. However, a micro-gravity environment such as in a low-Earth orbit will allow for drastically longer interrogation times, leading

to major advances in sensitivity. This represents a clear demonstration of the remarkable progress undertaken in the 22 years since the first discovery of a BEC and promises a wide ranging set of applications in fundamental physics and industry.

The use of BECs in atom interferometry is well documented due to their inherent coherent properties. Commonly an optical or magnetic trap is used to form one or more BECs separated by a potential barrier such as an optical plug. The BECs then fall under gravity and interfere, leading to visible interference fringes. One technique to increase the interference time involves using Ioffe-Pritchard magnetic trap coils as a means to levitate the BEC [52]. Additionally fabrication of atom chips is becoming increasingly common as a means of miniaturising interferometry experiments. An atom chip experiment etches grooves into a silicon wafer to act as waveguides with highly tunable geometries. Again using magnetic traps, a BEC is formed and split by introducing a double potential well before interfering [53].

1.4 Atom Interferometry as a Tool for Inertial Sensing

Interfering matter waves was first conceptualised by the idea of the de Broglie wavelength in 1924, that all particles exhibited wave like behaviour and therefore were free to interfere. The first experimental evidence of matter interferometry came in the 1950s when interference of electrons was observed by different groups [54, 55]. Neutron interference [56] followed soon after.

The idea of an atom interferometer has existed for a while and was patented in 1973 [57], but it took until 1991 for the group at MIT to observe the interference of sodium atoms [58]. Since then a multitude of different atom species have been interfered and provided many wide and varying potential applications in fundamental physics discoveries. Some examples include gravitational wave detection [59], testing of the equivalence principle using dual species interferometers [60] and measuring the gravitational constant G [61]. In addition, many industrial applications based on atom interferometry are actively being explored in the field of gravimetry [62] and inertial sensing [63].

An atom interferometer uses an ultra-cold source of atoms, obtained from a cold vapour or atom laser [64], and coherently splits it into two spatially separated paths. The paths are subject to different forces and upon recombination a phase difference will accumulate between the two. In a Sagnac interferometer atoms are coherently split into two clouds and

sent in opposite directions around a closed loop path before recombining. If the system is rotating atoms will travel different distances to complete the loop, imparting a different phase on one cloud relative to the other. The phase difference for photons or atoms in a Sagnac interferometer is given as

$$\phi_{Sagnac} = \frac{4\pi E}{hc^2} A\Omega, \tag{1.3}$$

where A is the area of the enclosed loop and E is the energy of the particle given as $E = \hbar\omega$ for a photon and $E = Mc^2$ for a particle with rest mass M. The matter wave interferometer will have a phase difference larger than the optical equivalent by a factor $Mc^2/\hbar\omega$ for an equal area. Comparing a ^{87}Rb atom to a photon with $\lambda = 780$ nm yields an increase in sensitivity by a factor of 5×10^{10}. However, this impressive comparison is tempered slightly as classical gyroscopes are able to utilise large enclosed areas using hundreds of metres of fibre optic cables compared to the proposed atom interferometer enclosed area of 1 mm^2. Whilst the sensitivity of the two may seem comparable, issues in minimising vibration and thermal expansion in a large reel of fibre optic cable weighs heavily in the atom interferometers favour, with a much smaller area required to be stabilised.

1.5 Waveguides for Cold Atoms

The idea of a matter wave circuit has long been postulated as a method to launch coherent atoms into waveguides where they can be split, recombined and detected [65]. As an enclosed area is required to measure rotation as an inertial sensor, the atoms have to be coherently split and separated spatially. Atoms must be guided in a manner that creates a consistent and repeatable path. Many methods have been proposed and used to achieve this. One common technique is the use of a painted potential to create a ring gyroscope. Such a device allows atoms to travel several times around a loop before recombining. Other promising applications include the rising field of atomtronics whereby a matter wave version of common electronic components can be created including diodes, transistors and batteries [66].

The advent of the BEC was the first major step in realising coherent matter waves with large de Broglie wavelengths in waveguides. Two primary methods to controlling the path of the matter wave are through the use of a magnetic field gradient or an optical dipole force.

Application of a magnetic field has been used to create a Michelson interferometer with linear arms using a BEC [67]. A circular waveguide has also been demonstrated, again using a BEC [48]. Several experiments using cold atoms also make use of magnetic waveguides and can form Y-junctions to split atoms [68].

An alternative is to use an optical dipole potential, which removes reliance on magnetic fields whilst maintaining a strong confining potential. The first example used hollow core optical fibres to guide atoms, originally predicted in 1993 [69] and realised in 1995 with straight and curved configurations possible [70]. Two overlapping horizontal dipole beams can also be used as a beam splitter [71, 72]. The disadvantage to this approach lies in the inhomogeneous potential of two crossing Gaussian optical dipole potentials. This creates complex splitting behaviour and oscillatory motion of atoms as the strongest potential lies in the centre of the dipole beam. Finally, the implementation of atom chips [73] is leading to interferometry on much smaller scales, an important step towards miniaturisation.

A novel approach to coherently splitting a BEC in optical dipole potentials is explored in this experiment, using two overlapping tightly focussed dipole beams [74]. The all-optical approach will prevent external magnetic fields from affecting the operation of the experiment, improving its long term reliability. The two crossing beams are derived from the same laser and interfere, creating an optical lattice that is able to selectively transmit and reflect atoms from one waveguide to another using the principle of Bragg reflection.

The intended application for this new approach of splitting a BEC is rotation sensing. By splitting atoms along two spatially separated paths and recombining them, a closed loop is created and information regarding any rotation that occurs can be obtained by looking at the interference pattern produced upon recombination. The novel design will allow for more rapid experiment cycles, facilitating an increase in sensitivity over current methods. The new approach is discussed and tested in detail, along with potential improvements and current limitations.

Chapter 2

Theory

2.1 Laser Cooling

Creating a stable source of cold atoms is vital to many modern atom interferometry experiments and to measure the evolution of light-atom interactions. The average velocity of an atom at room temperature is $300\,\mathrm{m\,s^{-1}}$. As interferometry relies on relatively long interaction times of hundreds of milliseconds, it necessitates the requirement to cool atoms to reduce their average velocity and hence kinetic energy $\langle E_k \rangle$, defined as

$$\langle E_k \rangle = \frac{1}{2} m \left\langle v^2 \right\rangle = \frac{3}{2} k_B T \,, \tag{2.1}$$

where m is the mass of the atom, $\left\langle v^2 \right\rangle$ is the average velocity of the atoms and T is the temperature. Laser cooling works on the principle of a momentum transfer from incident light to an atom. Using laser cooling, the average temperature can be reduced from a room temperature of 300 K to a μK level.

Laser cooling relies on an atom with two energy levels which are probed using resonant light to create a cooling cycle using laser light locked to atomic transitions. Considering a simple two level atom, an incident photon tuned to the transition frequency between the two levels will be absorbed, promoting it to the higher energy state. Through spontaneous emission the atom will emit the photon in a random direction and de-excite back to the ground state. This process will continue for as long as the laser light is incident on the atoms and locked to the correct frequency. As incident light from a laser will always impact from the same

direction, the net result is a momentum shift along the axis of the laser light and is shown in Figure 2.1.

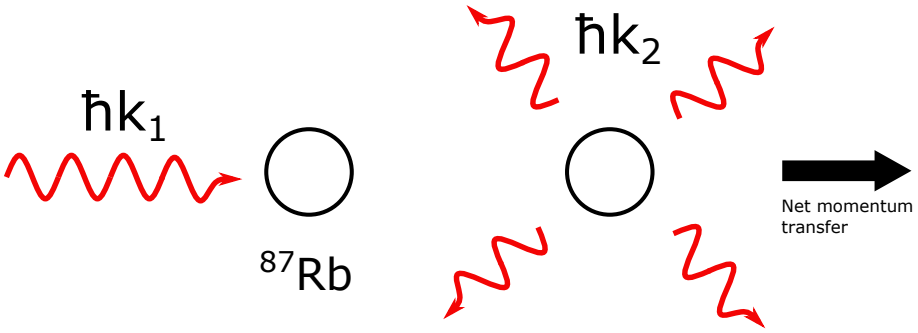

Fig. 2.1 A photon resonant with a transition of ^{87}Rb will be absorbed by an atom and be promoted to an excited state. The atom will then spontaneously decay back to a lower energy state, emitting a photon in a random direction as it does so. If the photons arrive to the atom from a single non-diverging direction such as in a laser, over many cycles between the two energy states the net momentum transfer will be along the axis of the light field.

In Doppler cooling a counter-propagating pair of lasers with light detuned slightly below the resonant frequency is used. The detuning means atoms with a velocity component in the direction of one laser will observe the light blue-detuned onto resonance, with the opposing laser light appearing further from resonance. Thus, the atom will more readily absorb a photon from the laser it is travelling towards and so will experience a momentum shift back towards the centre of the trap. One laser pair will generate cooling along one axis but atoms are still able to escape with velocity components orthogonal to the incident light. Using three such pairs of lasers [24] creates an overlapping region where atoms experience cooling along three dimensions. Over many such absorption and emission cycles the average kinetic energy of the atoms decreases. Using Equation 2.1 this leads to a reduction in the temperature of the atoms and is known as an optical molasses as the atoms experience resistance to movement in all direction. Atoms moving in any direction away from the centre will experience a resistive force from the surrounding light field. Due to the spontaneous nature of the process of absorbing and emitting photons cooling in this manner is limited by the linewidth and detuning of the incident light used to excite atoms and is described as

$$k_B T = \frac{\hbar\Gamma}{4} \frac{1+(2\Delta/\Gamma)^2}{2|\Delta|/\Gamma}, \tag{2.2}$$

where Γ is the linewidth and Δ is the detuning from the atomic transition frequency. The minimum temperature in a molasses is achieved when $2\Delta/\Gamma = -1$ and is given as

$$k_B T_{min} = \frac{\hbar\Gamma}{2}, \tag{2.3}$$

and is known as the Doppler cooling limit, first derived in 1977 by Minogin [75]. For the cooling transition in ^{87}Rb, a minimum temperature of 145.6 µK is achievable based on a linewidth of $2\pi\times$ 6.066 MHz [76].

Interestingly, the measured temperature of atoms in an optical molasses was found to be well below the Doppler limit [23], indicating that an additional previously unknown cooling effect was present. The ultimate cause was determined to arise from the polarisation of the two lasers causing additional cooling, known as polarisation gradient cooling. This can be used to further cool atoms using two separate approaches using either linear or circular polarisations. Linearly polarised counter-propagating light generates a standing wave. Continuing to use the simplified one dimensional model, two counter-propagating laser beams are set up to emit orthogonal linearly polarised light, known as the lin $\perp$ lin configuration. This creates a linear polarisation that rotates around the axis of the light field. As atoms travel up a potential, their kinetic energy is transferred to potential energy. At the summit of the potential the atom is now in either a σ_- or σ_+ polarisation and through optical pumping emits a photon, reducing its energy. Over many such transitions atoms lose enough energy to be cooled below the Doppler limit. The process is known as polarisation gradient cooling [77], or Sisyphus cooling, after the obvious allegory to the Greek myth where Sisyphus is condemned to push a boulder up a hill only for it to roll back down for eternity. A diagram example of Sisyphus cooling is shown in Figure 2.2. Additional cooling is now limited by the recoil energy gained when an atom spontaneously emits a photon and is known as the recoil limit. The minimum temperature is now defined as

$$T_R = \frac{\hbar^2 k^2}{2mk_B}, \tag{2.4}$$

arising from the the momentum of a single photon given as $p = \hbar k$ where k is the wavevector of the light. The recoil temperature for ^{87}Rb is 362 nK, significantly below the Doppler limit.

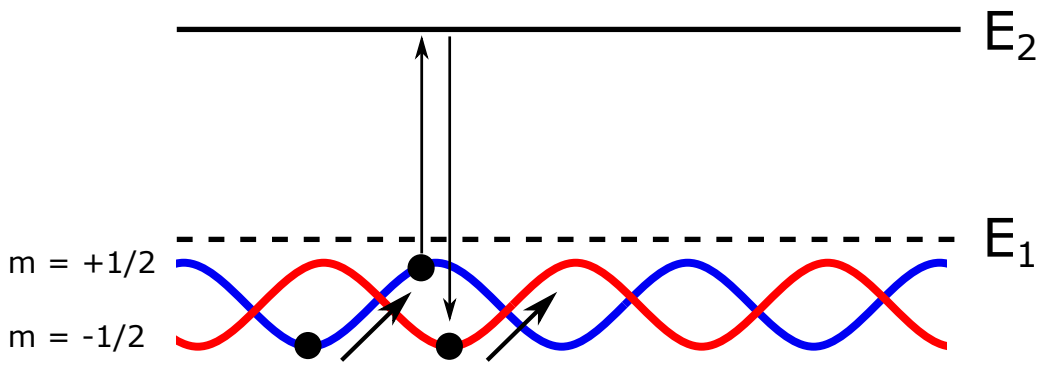

Fig. 2.2 An atom with a given kinetic energy in a standing wave generated by two circularly polarised beams will begin to climb a potential. At the peak the atom will undergo absorption and spontaneous emission of a photon, reducing its total energy.

Alternatively, circularly polarised counter-propagating light can also be used to provide additional cooling to atoms known as the σ_+ σ_- configuration. Two circularly polarised counter-propagating beams σ_+ and σ_- create a linear polarisation rotating around the axis of light propagation. The light shift of the ground state sublevels remains constant when atoms move along the z-axis shown in Figure 2.3. As a result there are no variations in ground state sublevels, meaning no possibility of Sisyphus cooling mentioned in the lin $\perp$ lin configuration. However, a cooling effect is still created from imbalances in the radiation pressure owing to population differences in the ground state as photons are absorbed with different efficiencies related to the polarisation of the beams. This effect dominates at low atom velocities and can again approach the recoil limit.

To understand where the cooling effect arises from, a rotating reference frame is introduced such that the linear polarisation keeps a fixed orientation parallel to the z-axis. An extra inertial term is added as

$$V_{rot} = kvJ_z\,, \tag{2.5}$$

where k is the wave vector of the light, v is the velocity of the atoms and J_z is the angular momentum quantum number. Considering the rotation reference frame and energy exchanges between the atoms and laser light field, and assuming $\Gamma' \ll |\Delta'|$ and $kv \ll |\Delta'|$, it can be shown that for an atom moving towards $z > 0$ with $v > 0$, $|g-1\rangle_z$ is more populated than $|g+1\rangle_z$. A full derivation can be found in [78] and is described more succinctly as

$$v > 0, \delta < 0 \Rightarrow \Pi_{-1} > \Pi_{+1}\,, \tag{2.6}$$

where $\Pi_{\pm 1} = |g \pm 1\rangle_z$ is an eigenstate of J_z. There is a greater probability that an atom in $|g-1\rangle_z$ will absorb a σ_0 photon propagating towards $z < 0$ than a σ_+ photon towards $z > 0$. In this scenario the radiation pressure becomes unbalanced by the ground state population induced by the inertial term from Equation 2.5. Therefore, the force amplitude is linear with respect to atom velocity. In the low velocity regime all coherences between ground state sublevels must be taken into account. However, in a high velocity regime these terms become negligible and the Doppler shift effect dominates.

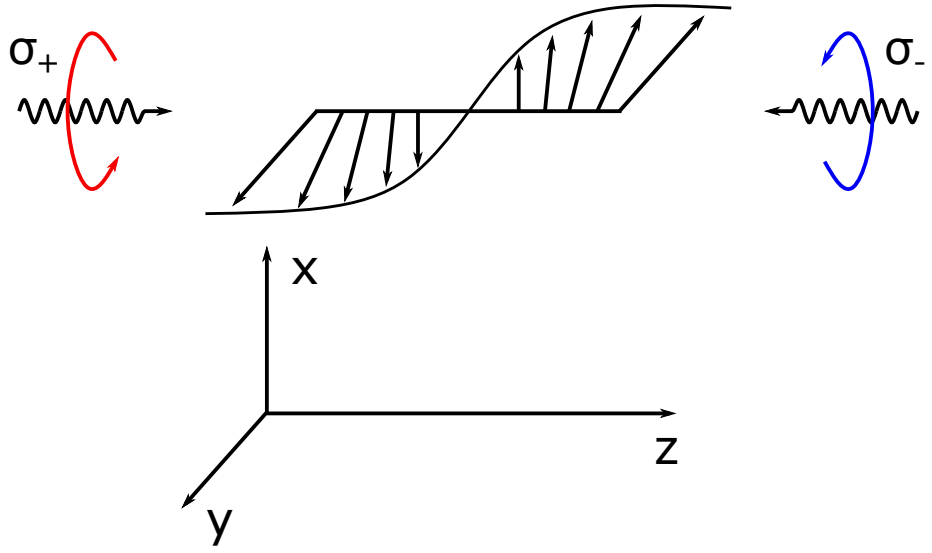

Fig. 2.3 A diagram to show the linear polarisation created when two circularly polarised waves with σ_+ σ_- polarisation are aligned to be counter-propagating. The direction of the linear polarisation rotates around the z-axis.

2.2 Magneto-Optical Trap

Laser cooling in an optical molasses is very effective and rapidly cools atoms from room temperature to the micro-kelvin scale. However, due to the random walk of atoms resulting from spontaneous emission of photons all atoms will eventually exit the molasses given enough time. To prevent this, spatial confinement can be provided using a quadrupole magnetic field gradient in an anti-Helmholtz configuration. This creates a region of zero magnetic field at the centre, the field gradient linearly increases with distance and is aligned

to overlap with the intersection of the laser beams. The first magnetic trap for neutral atoms was realised in 1985 [79] and is now commonly known as a Magneto-Optical Trap (MOT). Applying a magnetic field gradient will shift the energy of a sublevel proportional to the m_F number of the state.

Figure 2.4 displays a one dimensional model of the MOT trapping mechanics with the Zeeman sublevels split by the magnetic field. From the centre of the trap the energy of the three excited sublevels, $m = 0, \pm 1$, are equal. The energy levels shift when travelling away from the trap centre. For an atom existing in a position $z < 0$ from the trap centre, it will be more likely to be excited from the $m = -1$ transition as the laser is detuned from the atomic transition by a frequency Δ. The atom will preferentially absorb a photon from the σ_- beam whilst its position is $z < 0$ and so the net effect creates a momentum transfer in the positive z direction. A similar effect occurs when an atom is in a position $z > 0$, it will preferentially be absorbed by a σ_+ photon and experience a momentum transfer in the negative z direction.

The net result is a continual force pushing atoms towards $z = 0$ and can be expanded to create trapping in 3 dimensions using 3 pairs of retro-reflecting beams as the quadrupole field in an anti-Helmholtz configuration generates a field gradient in three dimensions.

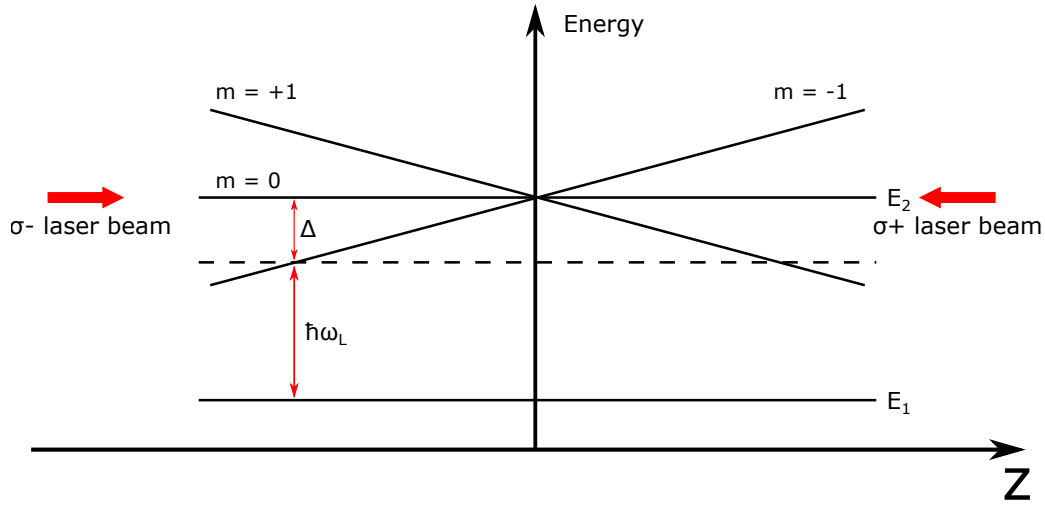

Fig. 2.4 A one dimensional simplified model of a Magneto-Optical Trap displaying the split Zeeman sublevels, increasing with distance from the trap centre.

2.3 Two Level Approximation of a Dipole Potential

The optical dipole force is created from dispersive interactions from an induced atomic dipole moment with the intensity gradient of the light field [80]. The dipole potential can be derived by considering an atom as a simple oscillator in a classical radiation field. An atom placed in laser light experiences an atomic dipole moment $\vec{p}$ induced from the electric field $\vec{E}$ that oscillates with a driving frequency ω. Using the usual complex notation the electric field is described as

$$\vec{E}(r,t) = \hat{e}\tilde{E}(r)exp(-i\omega t) + c.c\,, \tag{2.7}$$

where $\hat{e}$ is the unit polarisation vector. This field induces an atomic dipole moment $\vec{r}$, which is defined as

$$\vec{r}(r,t) = \hat{e}\tilde{p}(r)exp(-i\omega t) + c.c\,, \tag{2.8}$$

And oscillates with a frequency equal to the driving field. The amplitude $\tilde{p}$ of the dipole moment is related to the field amplitude $\tilde{E}$ by

$$\tilde{p} = \alpha\tilde{E}\,, \tag{2.9}$$

where α is the complex polarisability and depends on the driving frequency ω and is only valid when effects from saturation are negligible and the atoms favourably populate the ground state. The interaction potential of the induced dipole moment $\vec{p}$ in the driving field $\vec{E}$ is given by

$$U_{dip} = -\frac{1}{2}\left\langle \vec{p}\vec{E} \right\rangle = -\frac{1}{2\varepsilon_0 c} Re(\alpha) I\,. \tag{2.10}$$

The field intensity is given as $I = 2\varepsilon_0 c \left|\tilde{E}\right|^2$ where ε_0 is the permittivity of free space and c is the speed of light in a vacuum. The potential energy of the atom in the field is proportional to intensity I and to the real component of the polarisability. The dipole force results from the gradient of the interaction potential as

$$\vec{F}_{dip}(r) = -\nabla U_{dip}(r) = \frac{1}{2\varepsilon_0 c} Re(\alpha) \nabla I(r) \,. \tag{2.11}$$

The power absorbed by the oscillator from the driving field and subsequently re-emitted as dipole radiation is given as

$$P_{abs} = \left\langle \dot{p}\vec{E} \right\rangle = 2\omega Im(\tilde{p}\tilde{E}^*) = \frac{\omega}{\varepsilon_0 c} Im(\alpha) I \,. \tag{2.12}$$

This leads to the conclusion that absorption results from the imaginary part of the polarisability, describing the out of phase component of the dipole oscillation. If the laser light is considered as a stream of photons with energy $\hbar\omega$, absorption can be interpreted in terms of photons scattering through cycles of absorption and spontaneous re-emission processes. The scattering rate is therefore given by

$$\Gamma_{sc}(r) = \frac{P_{abs}}{\hbar\omega} = \frac{1}{\hbar\varepsilon_0 c} Im(\alpha) I(r) \,. \tag{2.13}$$

The interaction potential and scattered radiation power are now both expressed in terms of the position dependent field intensity denoted by $I(r)$ and are valid for any polarisable neutral particle existing in an oscillating electric field. To calculate the atom's polarisability α, consider it in Lorentz's model of a classical oscillator. Here an electron is considered to be elastically bound to the core of an atom with an oscillation frequency ω_0 which corresponds to the optical transition frequency. The polarisability can be calculated by integrating the equation of motion $\ddot{x} + \Gamma_\omega \dot{x} + {\omega_0}^2 x = -eE(t)/m_e$ for the driven oscillation of the electron to obtain

$$\alpha = \frac{e^2}{m_e} \frac{1}{{\omega_0}^2 - \omega^2 - i\omega\Gamma_\omega} \,, \tag{2.14}$$

where m_e is the electron mass and e is the elementary charge. Γ_ω is the classical damping rate defined as

$$\Gamma_\omega = \frac{e^2\omega^2}{6\pi\varepsilon_0 m_e c^3} \,. \tag{2.15}$$

Using the on-resonance damping rate $\Gamma \equiv \Gamma_{\omega_0} = (\omega_0/\omega)^2 \Gamma_\omega$ and substituting

$$\frac{e^2}{m_e} = \frac{6\pi\varepsilon_0 c^3 \Gamma_\omega}{\omega^2}, \tag{2.16}$$

Equation 2.14 can be rearranged to show

$$\alpha = 6\pi\varepsilon_0 c^3 \frac{\Gamma/{\omega_0}^2}{\omega_0^2 - \omega^2 - i\left(\omega^3/\omega_0^2\right)\Gamma}. \tag{2.17}$$

Atomic polarisability can also be calculated by considering the atom as a two-level quantum system as it interacts with the radiation field. The damping rate, or spontaneous decay rate of the excited level, denoted as Γ is now determined by the dipole matrix element between ground and excited state given as

$$\Gamma = \frac{{\omega_0}^3}{3\pi\varepsilon_0\hbar c^3} \left|\langle e|\mu|g\rangle\right|^2. \tag{2.18}$$

However, for D lines of alkali atoms Na, K, Rb and Cs the classical result agrees well with the spontaneous decay rate to within a few percent. Therefore, Equation 2.17 provides a good approximation for a quantum-mechanical oscillator. For low saturation and large detuning, the dipole potential and scattering rate are shown as

$$U_{dip}(r) = -\frac{3\pi c^2}{2{\omega_0}^3}\left(\frac{\Gamma}{\omega_0 - \omega} + \frac{\Gamma}{\omega_0 + \omega}\right) I(r), \tag{2.19}$$

and

$$\Gamma_{sc}(r) = \frac{3\pi c^2}{2\hbar{\omega_0}^3}\left(\frac{\omega}{\omega_0}\right)^3 \left(\frac{\Gamma}{\omega_0 - \omega} + \frac{\Gamma}{\omega_0 + \omega}\right)^2 I(r). \tag{2.20}$$

Further approximations can be made as in most experiments the laser is tuned close to the ω_0 resonance such that the detuning $\Delta \equiv \omega - \omega_0$ fulfills $|\Delta| \ll \omega_0$. In this case the rotating-wave approximation [81] can be made, allowing the relation $\omega/\omega_0 \simeq 1$. This simplifies Equation 2.19 and Equation 2.20 to a general expression as

$$U_{dip}(r) = \frac{3\pi c^2}{2{\omega_0}^3}\frac{\Gamma}{\Delta} I(r), \tag{2.21}$$

and

$$\Gamma_{sc}(r) = \frac{3\pi c^2}{2\hbar {\omega_0}^3} \left(\frac{\Gamma}{\Delta}\right)^2 I(r)\,. \tag{2.22}$$

The simple two-level approximation can be expanded to include other energy level contributions by expanding the time-dependent perturbation theory energy shift [82], given as

$$\Delta E = \frac{\hbar \Omega^2}{4\Delta}\,, \tag{2.23}$$

where Ω is the Rabi frequency given as

$$\Omega = \langle i|\mathbf{d}|f\rangle \frac{\varepsilon}{\hbar}\,. \tag{2.24}$$

Summing over all electric-dipole permitted transitions produces

$$\Delta E_i = -\frac{\varepsilon^2}{4\hbar} \sum_{i \neq f} |\langle i|d|f\rangle|^2 \left(\frac{1}{\omega_{if} - \omega} + \frac{1}{\omega_{if} + \omega}\right). \tag{2.25}$$

Two important details of dipole trapping are derived from these equations. Firstly the dipole potential is negative for red detuned laser light, $\Delta < 0$, creating an attractive force for atoms. Consequently, the maximum intensity occurs at the minimum of the potential and atoms are attracted towards regions of high field intensity. Conversely, a positive dipole potential is created for blue detuned light, $\Delta > 0$. Atoms will be repelled from the light field. A second conclusion is the dipole potential is proportional to $1/\Delta$, whereas the scattering rate is proportional to $1/\Delta^2$. Therefore, optical dipole traps use large detunings and high intensities to minimise the scattering rate for a constant potential depth.

2.4 Different Configurations of Dipole Traps

The use of far detuned lasers to confine atoms using a dipole trapping force was developed in 1993 [29], where a single red-detuned focused Gaussian beam was used to trap and cool

1300 ^{85}Rb atoms to sub millikelvin temperatures. This configuration is known as a far-off resonant trap (FORT) and provides trapping in three dimensions. However, the potential is stronger along the radial axis than the axial axis and must be sufficiently deep to hold atoms against gravity. For this reason a single Gaussian beam trap is best implemented along the horizontal axis.

It is also possible to trap atoms using a single blue-detuned Gaussian beam [83], whereby the beam is passed through a phase plate that creates segregated polarisation between the central and outer part of the beam with a phase difference of π. When focused by a lens, destructive interference creates a dark region around the focus and is surrounded by light. Therefore, trapping is generated by a hollow cone of repulsive light around the atoms. The main advantage of using a blue-detuned trap is the reduction in radiation trapping loss and lower atom collision rates. Many iterations of hollow core blue detuned traps exist, with some examples including a doughnut shaped trap [84, 85] known as a Doughnut hollow beam (DHB) and a gravito-optical conical atom trap [86]. Subsequent developments in hollow core technology has led to the development of atom trapping within hollow core fibres [87, 88]. Finally, evanescent waves can also be used to generate a confining potential where a uniform repulsive optical wall is created along several axes to create a trapping region. An evanescent wave is generated from the total internal reflection of a laser from a dielectric-vacuum interface. The amplitude of the wave falls exponentially with increasing distance from the interface. The first experimental example was used as an atom mirror to deflect a beam of atoms [89]. A review of many variations of atom mirrors is given in [90]. Subsequent work has led to trapping within nanofibres [91].

A second dipole beam intersecting the first with opposite polarisation to prevent interference can be added to greatly increase the trapping potential and is known as a crossed beam trap. This experiment uses such a trap and was first developed at Stanford [92], which uses two focused laser beams crossing at their focus. For orthogonal beams, an isotropic trap with strong confinement in all dimensions is created and is a useful compromise between the potential depth and trap volume. Here the dipole potential is estimated as

$$U_{CB}(x,y,z) \simeq -\hat{U}\left(1-\frac{x^2+y^2+2z^2}{{\omega_0}^2}\right). \tag{2.26}$$

This trap configuration is particularly suited to the creation of Bose-Einstein condensates and is the reason why the crossed dipole trap was chosen for this experiment.

Another dipole trap type is a standing wave trap, where a single red-detuned beam can be retro-reflected to generate a standing wave along the length of the beam. Atoms are strongly confined along the anti-nodes of the beam. The confinement is sufficiently great to realise a vertical configuration where the atoms are held against gravity. Such a trap was first proposed by Letokhov in 1968 [93] but it took until 1998 for it to be realised experimentally at Stanford [94] where a red-detuned 1064 nm laser was used to trap 10^7 caesium atoms in a vertical far detuned standing wave trap. One disadvantage to the standing wave trap is the large oscillation frequencies at the centre of the trap arising from the very tight confinement in the anti-nodes.

2.5 Bose-Einstein Condensation in Dilute Gases

A bosonic particle has an integer spin and identical bosons have no limits on the number of particles which can occupy the same quantum state. A Bose-Einstein Condensate is formed when a macroscopic number of bosonic particles occupy a single quantum state and become indistinguishable as the individual de Broglie wavelengths begin to overlap. The de Broglie wavelength is defined as

$$\lambda_{dB} = \left(\frac{2\pi\hbar^2}{m k_B T} \right)^{1/2}, \tag{2.27}$$

where m is the mass of an atom and T is the temperature. The de Broglie wavelength represents a spatial uncertainty of the momentum distribution. From the inverse relationship a reduction in temperature increases λ_{dB}. Despite the high average velocity of atoms at room temperature, their position is well localised with respect to their de Broglie wavelength and behave as point-like objects. As the temperature is decreased, λ_{dB} increases to a point where λ_{dB} is comparable to the interparticle separation and the atoms become increasingly delocalised, known as the critical temperature or T_c. Atoms at this temperature experience a phase transition to form a Bose-Einstein Condensate. Atoms all occupy the same quantum state and are coherent, meaning they exhibit the same phase and frequency.

Bose and Einstein derived an expression [32] for the ground state occupation of atoms at a temperature T and energy ε as

$$\overline{N_0} = \frac{1}{\left[exp\left[\frac{\varepsilon-\mu}{k_B T}\right]-1\right]}, \tag{2.28}$$

where μ is the chemical potential and k_B is the Boltzmann constant. Making the assumption that the cloud is an ideal gas with non-interacting particles is permissible in the case of low atom densities. μ measures the change in energy of the system when a new particle is added. Using Equation 2.28, the population of atoms in the ground state must be positive so it follows that $\mu \leq 0$. For a room temperature gas, μ is large and negative and reduces in line with temperature. $\overline{N_0}$ is maximised when $\mu = 0$, corresponding to a temperature $T \leq T_c$.

Following on it is possible to express the total population of all states by considering the case where all atoms are populated in the ground state, $\varepsilon = \mu = 0$. Here N_0 becomes unphysical. Then the total population N is given as the sum over all states as

$$N = \overline{N_0} + \sum_{\varepsilon \neq 0} \frac{1}{\left[exp\left[\frac{\varepsilon-\mu}{k_B T}\right]-1\right]}. \tag{2.29}$$

The density of states can be calculated from evaluating the integral in three dimensional space to yield

$$g(\varepsilon) = \frac{4\pi\sqrt{2}}{(2\pi\hbar)^3} M^{3/2} \int \sqrt{\varepsilon} d\varepsilon \, d\mathbf{r}^3, \tag{2.30}$$

where $\varepsilon = p^2/2M$. A full derivation can be found in [95].

The density of states is defined as the number of states between ε and $\varepsilon + d\varepsilon$ and is given as

$$g(\varepsilon) = \frac{4\pi\sqrt{2}M^{3/2}V\varepsilon^{1/2}}{(2\pi\hbar)^3}, \tag{2.31}$$

where the volume in three dimensional space $d\mathbf{r}_3$ is represented by $V = \int d\mathbf{r}_3$.

Substituting into Equation 2.29 yields

$$N = \overline{N_0} + \frac{4\pi\sqrt{2}}{(2\pi\hbar)^3} V M^{3/2} \int_0^\infty \frac{\varepsilon^{1/2} d\varepsilon}{\exp\left[\frac{\varepsilon-\mu}{k_B T}\right] - 1}. \tag{2.32}$$

Useful conclusions can be drawn by considering population changes in different states as N increases. As $\mu < 0$, all states are populated according to the density of states in Equation 2.31. If N increases at a constant temperature T and volume V, μ will tend towards 0. At $\mu = 0$, the second term in Equation 2.32 can be simplified and evaluated to find

$$\frac{4\pi\sqrt{2}}{(2\pi\hbar)^3} V M^{3/2} (k_B T)^{3/2} \int_0^\infty \frac{x^{1/2} dx}{e^x - 1}. \tag{2.33}$$

The definite integral has a value of $2.61\sqrt{\pi}/2$. As $\mu \to 0$ the temperature T can be represented as the critical temperature T_c representing the temperature at which atoms will undergo a phase change. Simplifying further generates

$$k_B T c = 3.31 \frac{\hbar^2}{M} \left(\frac{N}{V}\right)^{2/3}, \tag{2.34}$$

which allows a simple calculation of the temperature required for atoms to condense into a Bose-Einstein Condensate. Equation 2.33 represents the maximum chemical potential energy, but the density of particles given as $\rho = N/V$ is still finite. If the density increases for a fixed temperature above the point where $\mu = 0$ and $\rho > \rho_c$ then the states are no longer equally populated, with the extra particles macroscopically occupying the ground state $\overline{N_0}$. Particles in this state are known as the Bose condensate, with a density of $\rho - \rho_c$.

2.6 Thomas-Fermi Approximation

Dynamics of a BEC in a trap can be calculated analytically. The time evolution of the ground state of a quantum system of identical bosons such as a trapped condensate can be inferred from the non linear Schrödinger equation and the Gross-Pitaevskii equation (GPE) [96] given as

$$i\hbar \frac{\partial}{\partial t} \phi(\vec{r}, t) = \left(\frac{-\hbar^2}{2m} \nabla^2 + V_{ext}(r) + g |\phi(\vec{r}, t)|^2 \right) \phi(\vec{r}, t), \tag{2.35}$$

where the number density $n(r) = |\phi(\vec{r},t)|^2$ and V_{ext} is the external potential and considered to be a spherical harmonic oscillator for simplicity. The interaction constant is given as

$$g = \frac{4\pi\hbar^2 a}{m}, \tag{2.36}$$

where a is the scattering length and m is the atomic mass [97]. If interactions are negligible ($g = 0$) this reduces to the standard Schrödinger equation for a single-particle Hamiltonian as $-\hbar^2/2m\nabla^2 + V_{ext}(\vec{r})$.

As the GPE is a non-linear Schrödinger equation with no exact solution it requires simplification to be solved analytically. This is achieved by first considering a harmonic potential

$$V(r) = \frac{m{\omega_0}^2}{2} r^2. \tag{2.37}$$

For a cloud of size ξ an estimate of the average kinetic energy per particle is given as

$$\vec{E}_{kin} \simeq \frac{\hbar^2}{2m\xi^2}. \tag{2.38}$$

Similarly, the average potential energy per particle is

$$\vec{V} \simeq \frac{m{\omega_0}^2}{2} \xi^2. \tag{2.39}$$

Using the virial theorem from Equation 2.38, and Equation 2.39 the typical cloud size when $U_0 = 0$ can be calculated, and is given as

$$\xi = \sqrt{\frac{\hbar}{m\omega_0}}. \tag{2.40}$$

The interaction energy per particle can be defined as a function of particle density $n = N/\xi^2$ where N is the number of particles as

$$\vec{E}_{int} \simeq U_0 n \simeq U_0 \frac{N}{\xi^3}. \tag{2.41}$$

Both the interaction energy and kinetic energy from Equation 2.38 are proportional to the inverse of the cloud size ξ. As the GPE is based on weak interactions and the interaction and kinetic energy act in complementary directions, an assumption can be made to exclude the weaker of the two terms. Comparing the kinetic and interaction energies if U_0 exceeds the critical strength

$$U_{0,crit} \simeq \frac{\hbar\omega_0}{2n}, \tag{2.42}$$

the kinetic term can be ignored. This is known as the Thomas-Fermi approximation and can be used to estimate the typical cloud size of atoms in a BEC in the presence of an interaction R, given as

$$\frac{\partial}{\partial R}\left(\frac{m{\omega_0}^2}{2}R^2 + U_0\frac{N}{R^3}\right) = m{\omega_0}^2 R - 3U_0 N\frac{1}{R^4} = 0. \tag{2.43}$$

This can be rearranged to obtain

$$R \simeq \left(\frac{NU_0}{{\omega_0}^2}\right)^{1/5} \simeq \xi\left(\frac{Na}{\xi}\right)^{1/5}, \tag{2.44}$$

where the interaction constant $U_0 = 4\pi\hbar^2 a/m$ is replaced with the scattering length a to highlight how the non-interacting cloud size is changed by another length scale, Na.

Chapter 3

Cold Atomic Sample Preparation

Generating a repeatable cold source of atoms is essential and the importance of rapidly producing large quantities of atoms condensed into a BEC cannot be understated. Any experimental results will consist of many thousands of repeated measurements, all stemming from the same cold atomic source. For this reason there is a strong desire to design a system capable of delivering a repeatable, similar sized BEC over a period of many days or weeks.

A number of considerations have to be made when building a system for use with ultra-cold atoms. Firstly the choice of atom to experiment on is considered. Recent rapid advances in laser technologies now allow for a plethora of options to cool a wide range of atoms. This experiment uses 780 nm diode lasers to cool down and trap ^{87}Rb atoms due to their property to condense into a Bose-Einstein Condensate and has been widely demonstrated and understood following the first demonstration in 1995 [36] using magnetic evaporative cooling from a TOP trap by ramping down the rf frequency and amplitude of the field [98]. All-optical evaporative cooling is desirable as it generally forms a BEC more rapidly than using a magnetic trap, which often requires an evaporative cooling duration in excess of 30 s [99].

The vacuum chamber design is integral to the success of the experiment. A Low Velocity Intense Source (LVIS) [100] is used to pre-cool the rubidium atoms and help maintain the quality of vacuum in the glass cuvette, designed to give maximum optical access to incident laser beams.

3.1 Vacuum Chamber

A stable ultra-high vacuum is essential for the creation and longevity of ultra-cold atoms. The vacuum chamber consists of two main sections, an LVIS chamber and the main chamber. The two are separated by a differential tube, consisting of a retro-reflecting mirror with a 2 mm diameter hole in its centre. This helps to minimise the background flux of thermal atoms present in the main chamber, thus improving the quality of the vacuum and therefore atom lifetime. The main science chamber is composed of a glass cuvette, providing maximum optical access for the multitude of laser beams required to run the experiment. The glass cell measures 30 x 30 x 130 mm and extends horizontally from the LVIS chamber using a glass to metal transition piece. The pressure inside the main chamber is in excess of 5×10^{-10} mbar, whilst the residual pressure in the LVIS chamber is determined by the pressure of rubidium vapour at room temperature and is roughly 1×10^{-7} mbar.

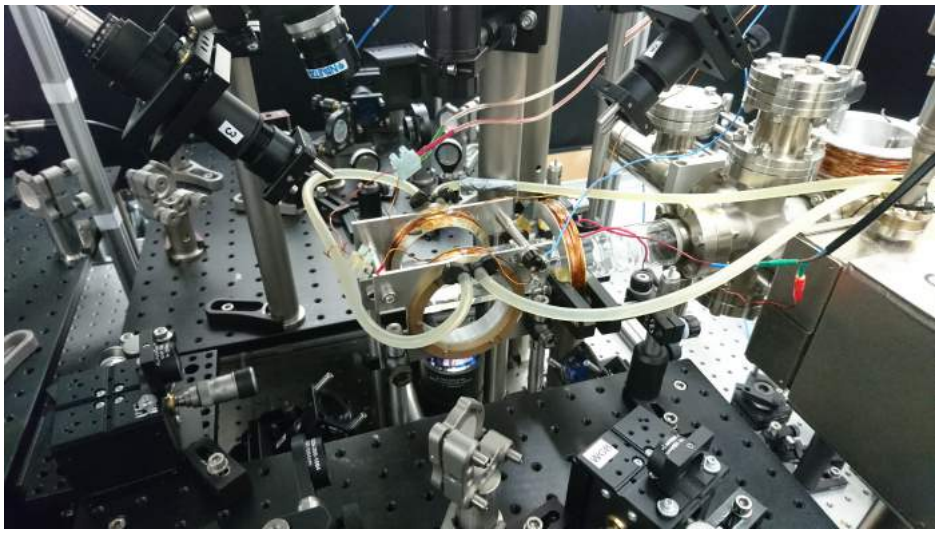

Fig. 3.1 An image to show the 3D MOT chamber. The glass cuvette is surrounded by the scaffolding used to hold the 3D MOT coils in place which are water cooled. The glass to metal transition to the right of the cuvette leads to the LVIS chamber. An ion pump used to maintain a vacuum in the chamber is shown on the far right of the image. Three large magnetic coils arranged in a cube are used to compensate for the Earth's magnetic field and are known as bias coils. One of the legs holding the coils is visible to the left of the image.

Figure 3.1 shows an image of the cuvette where the 3D MOT is formed. Two of the MOT outcouplers are visible in the top of the image, along with a diagnostic camera used for general imaging. Figure 3.2 displays a diagram of the complete double MOT vacuum system.

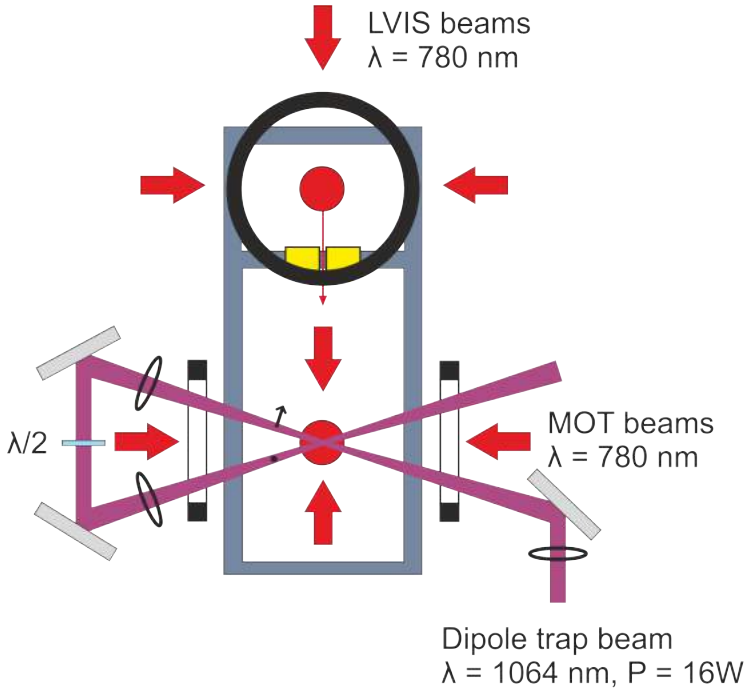

Fig. 3.2 Not to scale. A diagram of the double MOT vacuum chamber with arrows indicating the positions of the MOT beams. The orientation of the magnetic coils is also visible.

3.2 Laser Systems

Lasers used in this experiment were specifically chosen for their high power output and clean wavefront enabling easy coupling to fibres. The frequency of light from a laser is adjusted through modifying its temperature and input current. Therefore, a key requirement is low drift in laser frequency due to thermal and vibrational noise. Control over the laser diode temperature is achieved using an internal peltier cooler attached to a PID control circuit to maintain a constant temperature. Large heat sinks and a stabilised laboratory also help to maintain a consistent diode temperature.

Originally, cooling light locked to the $F = 2 \Rightarrow F' = 3$ transition was generated using a Toptica TA100 which provided up to 1 W of power when new, but was over 10 years old and was limited to a maximum output of 300 mW. As part of a series of upgrades across the experiment it was replaced with a Toptica TA pro, featuring a built in tapered amplifier to produce up to 2 W of continuous-wave (cw) light and a linewidth of 100 kHz. Optics built into the laser housing after the amplifier ensures a Gaussian wavefront enabling easy coupling to fibres. Additionally, an optical isolator is used to prevent any back reflections

from fibres or mirrors re-entering the laser. Finally, the laser is also used to generate light used in absorption imaging of the atomic clouds at the end of an experiment cycle.

Repumper light is required to complete the cooling cycle and is locked to the F = 1 $\Rightarrow$ F' = 2 line. Originally a master and slave laser configuration was used but required regular realignment and provided little power. The laser configuration was replaced with a Moglabs cateye diode laser with up to 100 mW of power available. The cateye diode virtually eliminates noise arising from external vibrations allowing for a stable lock over long time frames. An optical isolator is also required to prevent back reflections.

The dipole trap and subsequent evaporative cooling is produced using an IPG photonics YLR-LP-SF single mode fibre coupled laser providing up to 30 W out of a fibre with λ =1064 nm. Using a fibre coupled laser yields a beam with a Gaussian wavefront and is useful when coupling to other fibres or performing numerical calculations.

3.3 Locking to Atomic Transitions

Atoms in a room temperature gas travel randomly, moving in all directions with a high velocity. The observed frequency of a spontaneously emitted photon will be shifted relative to the atom's observed velocity in accordance with the Doppler effect. Over many emitted photons, the frequency will be broadened into a spectrum known as Doppler broadening. The hyperfine structure of ^{87}Rb has a linewidth much smaller than the Doppler broadened peaks meaning sub-Doppler techniques are required.

Hänsch was influential in developing one of the first examples of saturated absorption spectroscopy in 1971 and is used to overcome the Doppler limit [101] to observe hyperfine structures. Selective absorption of atoms with zero relative velocity removes any frequency spread arising from the Doppler effect. To achieve this, a strong pump beam tuned to the F = 2 $\Rightarrow$ F' = 3 transition is passed through a vapour cell containing gaseous rubidium atoms. A large majority of atoms will be excited to the F' = 3 state, minimising population in the F = 2 state. If the pump beam is sufficiently strong, the atom population in the F' = 3 state becomes saturated. An additional weaker probe beam tuned to the same frequency is implemented counter-propagating to the pump. An atom with a velocity component parallel to the pump or probe will see two separate frequencies, whereas an atom with only a perpendicular velocity component, or a relative velocity of 0 mm s^{-1}, will observe the

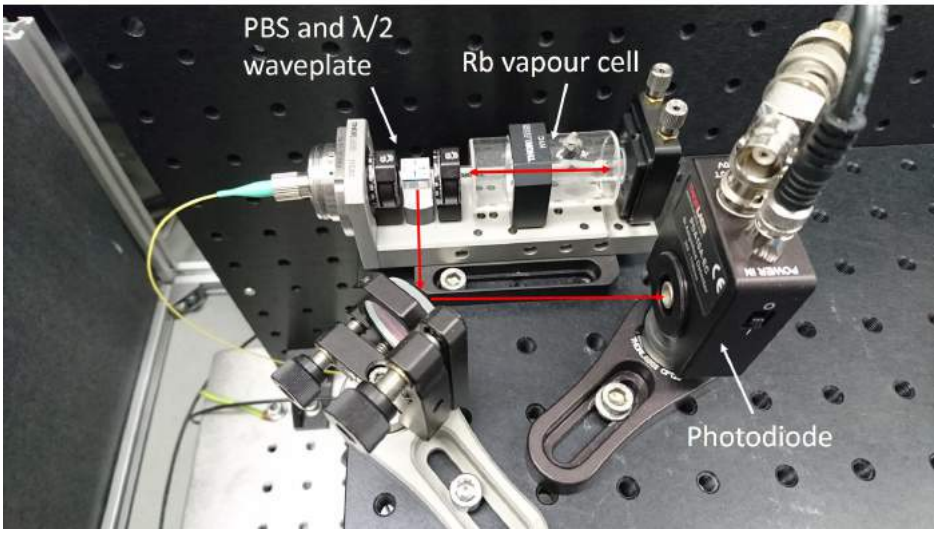

Fig. 3.3 Compact experimental setup of saturated absorption spectroscopy circuit used to lock the laser to a transition of ^{87}Rb. A small fraction of light from the cooling laser exits from a fibre and passes through a rubidium vapour cell before a mirror retroreflects the beam. Light is then sent to a photodiode. Scanning over a range of frequencies reveals the hyperfine structure.

pump and probe as exhibiting the same frequency. As the probe beam encounters an atom, it is likely to be in an excited state and will undergo stimulated emission. As the frequency of the pump and probe beam is modulated around the transition frequency of the atoms, a small dip will be observed at each hyperfine transition. This technique can approach the natural line width of the transitions [102]. The linewidth is now limited by atoms colliding with the walls of the rubidium cell, causing excitations. Figure 3.3 shows an image of the optical components used to observe the hyperfine peaks. A small fraction of light, typically less than 1 mW to avoid saturating the atomic transition, from the cooling laser is coupled into a fibre. The light is collimated and passed through a rubidium vapour cell twice before readout via a photodiode. A small modulation of the laser frequency is required to view the hyperfine structure and is achieved using a fibre coupled electro-optic modulator (EOM). The laser responsible for generating repumper light is also locked using saturated absorption spectroscopy. The voltage applied to the piezo attached to the laser diode is modulated to increase the scanning range. Figure 3.4 displays a typical readout from a saturated absorption spectroscopy setup with a large frequency scan, where two hyperfine structures are visible. Figure 3.5 displays all the transition lines of ^{87}Rb and labels the lines used for the cooling and repumping lasers.

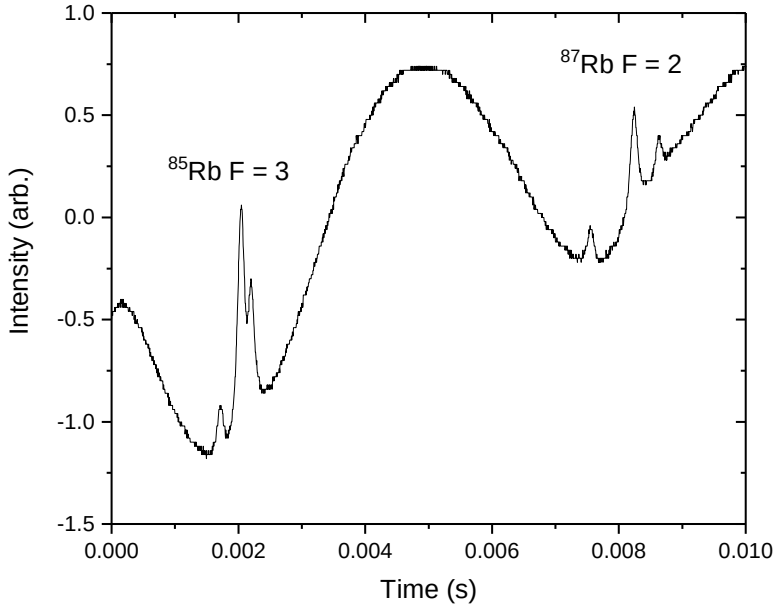

Fig. 3.4 Saturated absorption spectrum showing a broad Doppler peak with two hyperfine structures revealed. From left to right the ^{85}Rb F = 3 and ^{87}Rb F = 2 transition lines are shown.

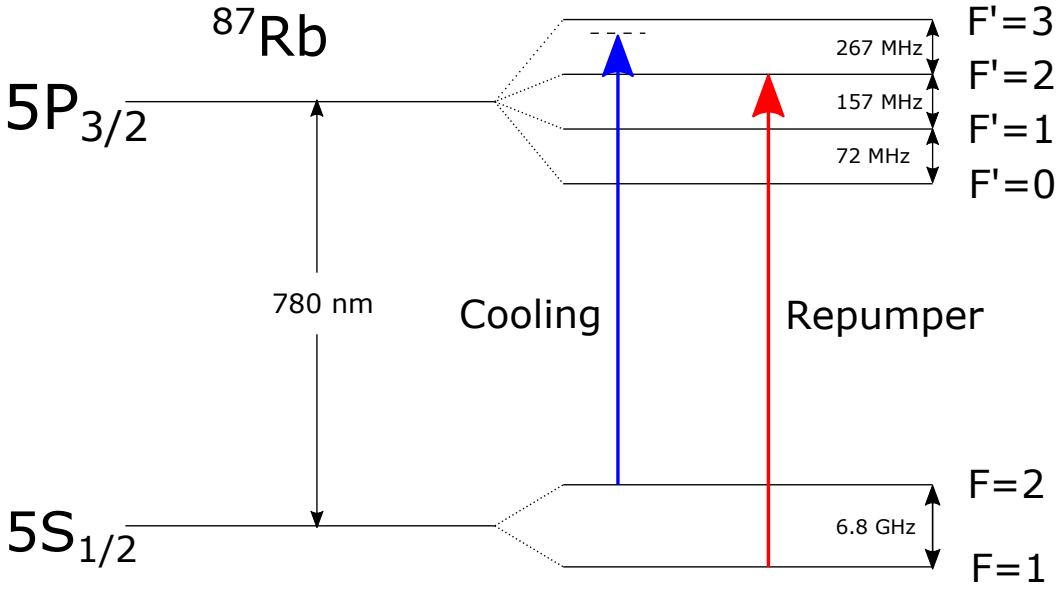

Fig. 3.5 A diagram showing the energy levels of ^{87}Rb. The cooling light is slightly detuned from the F = 2 $\Rightarrow$ F' = 3 transition and the repumper is locked to F = 1 $\Rightarrow$ F' = 2.

3.4 Acousto-Optic Modulators and Shutters

Acousto-optic modulators (AOMs) are used extensively in this experiment for their fast frequency shifting and intensity control ability. An AOM consists of a crystal typically made from quartz through which laser light propagates. Attached is a piezoelectric inducer which generates an RF wave through the crystal with a modifiable frequency and amplitude. The waves cause the refractive index of the crystal to increase, meaning as light passes through the crystal it will diffract with an angle θ_d according to the Bragg diffraction condition as

$$n\lambda_L = 2\Lambda \sin\theta_d \,, \tag{3.1}$$

where the optical and acoustic wavelengths are given as λ_L and Λ respectively and n is an integer. Light is split spatially into many orders with varying intensities. Adjusting the incident angle of the beam can maximise transmission of the different orders. The $n = -1$ order is selected meaning light will be downshifted by the frequency of the applied RF wave. The intensity of light in $n = -1$ is determined by the amplitude of the RF signal. Undiffracted light remains in $n = 0$ thus allowing fast control of power. Separate AOMs are linked to power stabilisation circuits and used as intensity controls for the dipole and waveguide beams. Figure 3.6 shows a typical response curve from an AOM using a photodiode to record intensity of an incident laser beam. The delay in switching is related to the time taken for the RF wave to propagate through the crystal.

AOMs therefore provide quick switching options and a high level of control over the intensity of laser light. However even when the RF signal is completely removed by reducing the input amplitude to zero a small fraction of light still exists in $n = -1$, sufficiently large enough to disrupt the experiment. Roughly 30 dB of suppression can be achieved from the AOM, meaning a typical MOT beam of 40 mW will still contain 40 µW of leaking light. Mechanical shutters are used to completely remove unwanted light. These have orders of magnitude worse temporal response but eliminate all leaking light, up to the sensitivity of the power meter.

Figure 3.7 shows two graphs displaying the response curve of the same mechanical shutter. Figure 3.7b uses a pre-trigger to apply a voltage to the shutter before it is called to ensure light leakage is minimised. Both graphs display a small increases in intensity at 80 ms and 110 ms respectively. These arise from the shutter bouncing when it reaches its new position

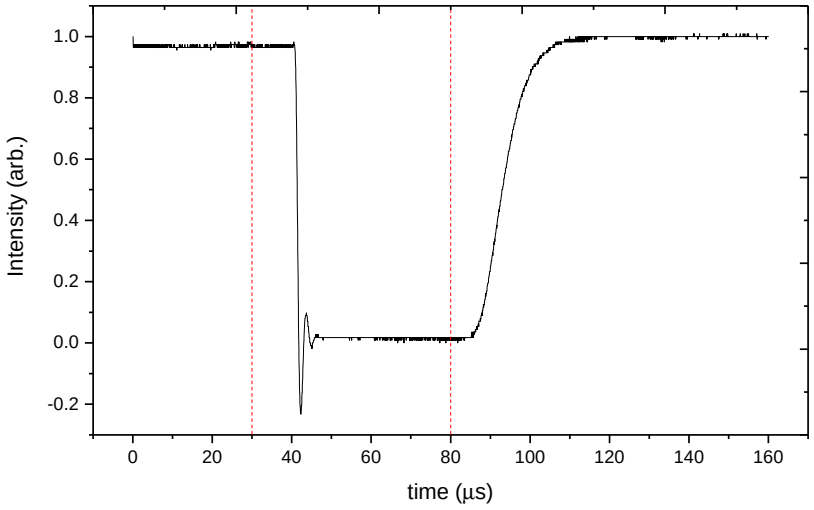

Fig. 3.6 A response curve of an AOM used to rapidly control the power of the incident laser beam. A signal is sent to the AOM to remove the RF sound wave for 50 μs. The two dashed red lines represent the point a signal is sent to the AOM, which indicates the response time is 5 μs. The AOM is adjusted to optimise switch off times as unwanted light in the science chamber is detrimental to trapping atoms.

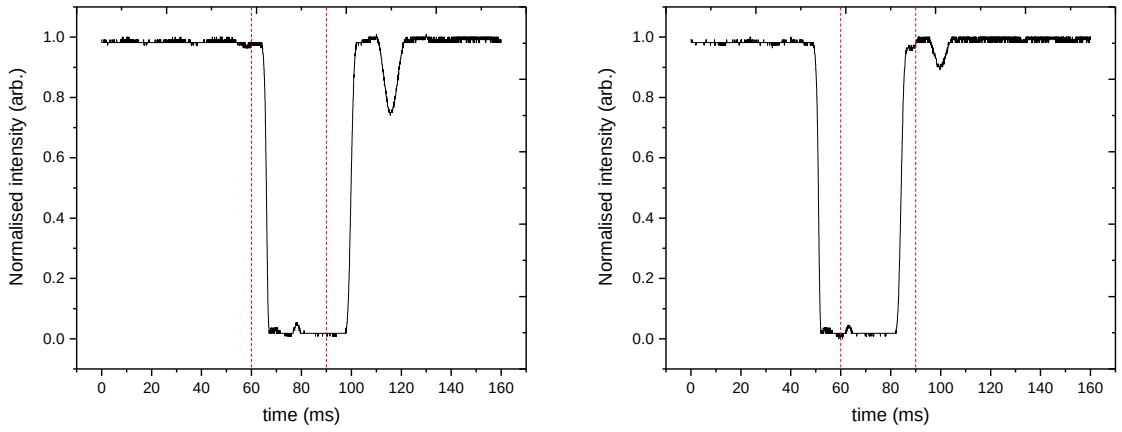

(a) Standard shutter response.

(b) Anticipated delay.

Fig. 3.7 Graphs to show the response of a mechanical shutter switching on for 30 ms. Red dashed lines indicate the point at which a voltage is applied to the shutter. Figure 3.7a displays the normal response of the shutter. Figure 3.7b anticipates the delay in operation of the shutter and pre-emptively applies a voltage to ensure light is blocked when required.

and a small fraction of light momentarily passes through. As this shutter is used to control light for the MOT beams, more care was taken to minimise the effect of bouncing when switching off the light to prevent this impacting later stages of the experiment. However, switching on the MOT lasers is only performed at the beginning of an experiment cycle and is not particularly critical to operations. For this reason, a large shutter bounce is visible when the light is returned to full intensity.

3.5 LVIS Cold Atom Source

The LVIS chamber consists of a DN40 stainless steel cross with five optical viewports of diameter 40 mm. The sixth output port leads to the main chamber and is blocked by a mirror with a gold coating. Attached to the mirror is a $\lambda/4$ waveplate to rotate the polarisation of retro-reflected light by π, necessary for atom trapping [103]. A small aperture in the centre of the mirror allows laser cooled atoms to be extracted into the main chamber. A pair of magnetic coils arranged in an anti-Helmholtz configuration provides a trapping force to the atoms, see Chapter 2.2. Excess heat generated by the MOT coils is removed using a diaphragm pump circulating water cooled to a constant temperature.

The main chamber is shown in Figure 3.1 separated from the LVIS chamber by a distance of 30 cm and is primarily made of glass, designed to give maximum optical access. A steel to glass transition piece extends for 10 cm to account for their different thermal expansion coefficients before the main glass cuvette of length 13 cm allows full optical access from all angles.

3.6 Forming the 3D MOT

The MOT acts as a reservoir of cold atoms and forms the basis of the experiment, therefore it is essential to maintain a good quality MOT at all times with sufficient loading speed and maximum size to provide for the rest of the experiment. Figure 3.8 shows a simplified diagram of the optical table used to generate a total of 10 beams from two lasers locked to separate transitions of ^{87}Rb to form an LVIS and a 3D MOT. Light intensity from both lasers is controlled via separate AOMs and serves a dual-purpose for the cooling light, allowing additional detuning for better MOT loading. As the frequency of cooling light is variable,

a double-pass AOM configuration is used to maintain the alignment of the beam. A small fraction of cooling light is sent to a different double-pass AOM setup, configured to bring light back onto resonance for use in imaging. However, the majority of light is split roughly equally between the LVIS and 3D MOT using a polarising beamsplitter (PBS). The 3D MOT uses 3 pairs of orthogonal beams and are created using a series of polarising beamsplitters to split a fraction of light from the main beam. A final PBS splits light roughly in half which is then coupled to two separate fibres and sent to MOT outcouplers on the main experiment table. Fine control of power balances between a pair of MOT beams is easily achieved in this setup by adjusting the final $\lambda/2$ waveplate to ensure that equal power is emitted by each MOT outcoupler regardless of coupling efficiency.

Light to the LVIS is split in a simpler way as the LVIS uses 3 retro-reflecting beams to form a MOT to reduce the total power requirements, as only 3 beams are required. The repumper only requires a single pass AOM to control the intensity, as its frequency is unchanging and a double pass AOM will only incur more losses. Rempumper and cooling light are overlapped using polarising beamsplitters. This creates a perfect overlap allowing both beams to be coupled into the same fibre. Mechanical shutters are used to ensure light into the fibres is completely off when necessary A separate shutter controls the cooling and repumper light into the LVIS and 3D MOT, as well as an additional shutter to control the probe beam for a total of 5 shutters.

To help achieve a fast loading time, an LVIS is used to provide a continuous flux of pre-cooled atoms [104]. The rubidium source is located in this chamber. A pair of magnetic coils are arranged in an anti-Helmholtz configuration to create a minimum magnetic field strength at the centre of the LVIS chamber. Three pairs of circularly polarised, retro-reflecting beams are arranged orthogonal to each other to provide a cooling effect on the atoms as described in Chapter 2.1. The beams are fibre coupled to ensure a symmetrical Gaussian wavefront and expanded to a diameter of 25 mm at a $1/e^2$ intensity interval to create a large illuminated area to trap many atoms in the MOT. Roughly 30 mW of power is used for cooling light per beam. To complete the cooling cycle, repumper light is sent through a single beam pair with a power of 2 mW.

The LVIS and the 3D MOT are separated by one mirror placed between the two chambers used for retro-reflection that contains a 2 mm diameter aperture at its centre. This creates a dark channel through the centre of the LVIS MOT. Atoms already cooled by the surrounding laser light enter the dark channel and experience a pushing force in one direction as there is no retro-reflection. Cooled atoms are guided through the aperture and into the cuvette

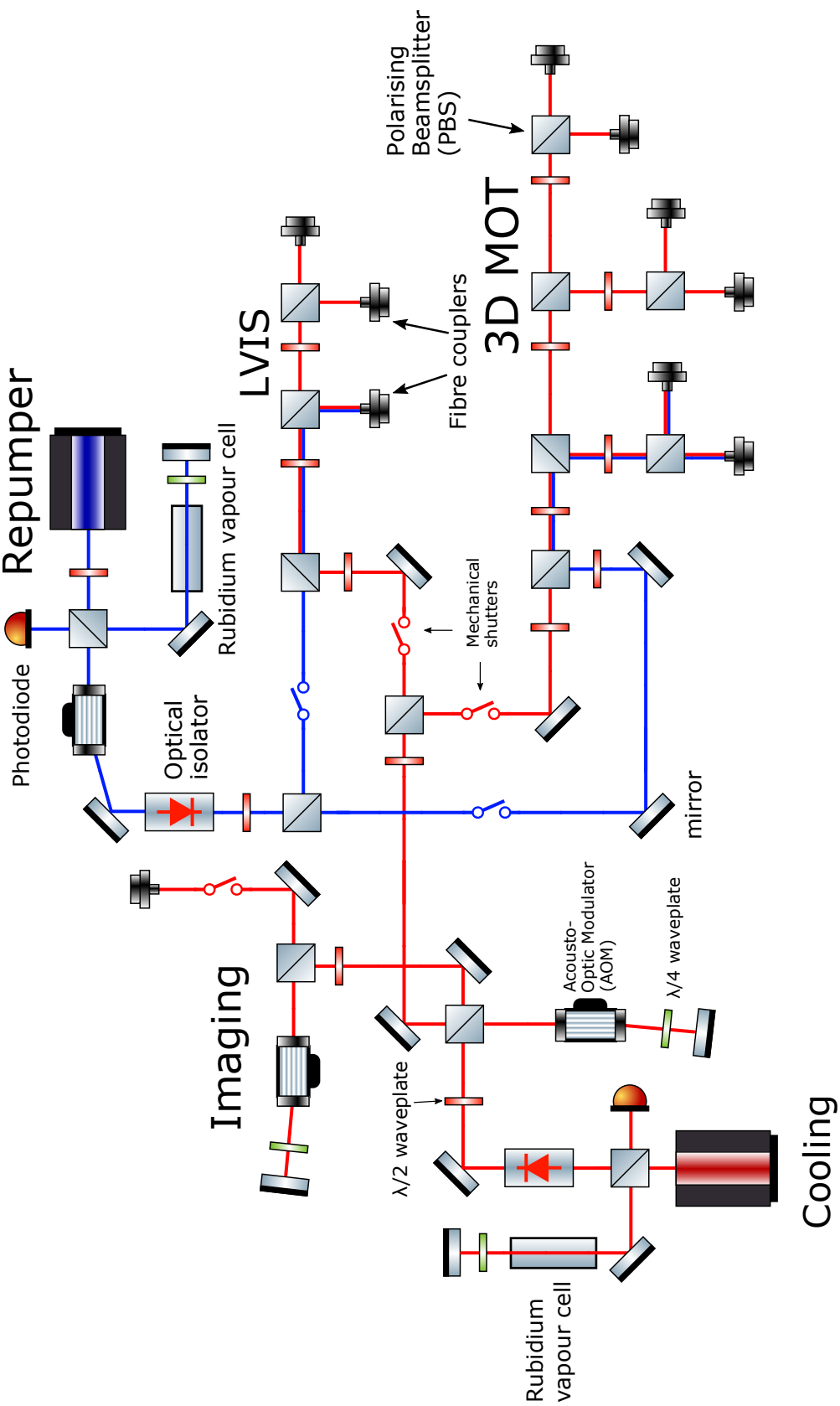

Fig. 3.8 A schematic to show how light from two separate lasers locked to different transitions are split to create 10 separate beams. The different colours represent light from the Toptica and Moglabs lasers used to generate cooling and repumper light respectively. A simplified version of the saturated absorption spectroscopy is shown for both lasers. The 5 mechanical shutters are displayed as a circuit diagram switch for simplicity.

containing the 3D MOT. The other retro-reflected beams are deliberately off-set to be angled slightly towards the 3D chamber to help increase the flux of atoms.

Separating the rubidium source from the cuvette helps to improve the 3D MOT lifetime due to an improved vacuum relative to the LVIS.

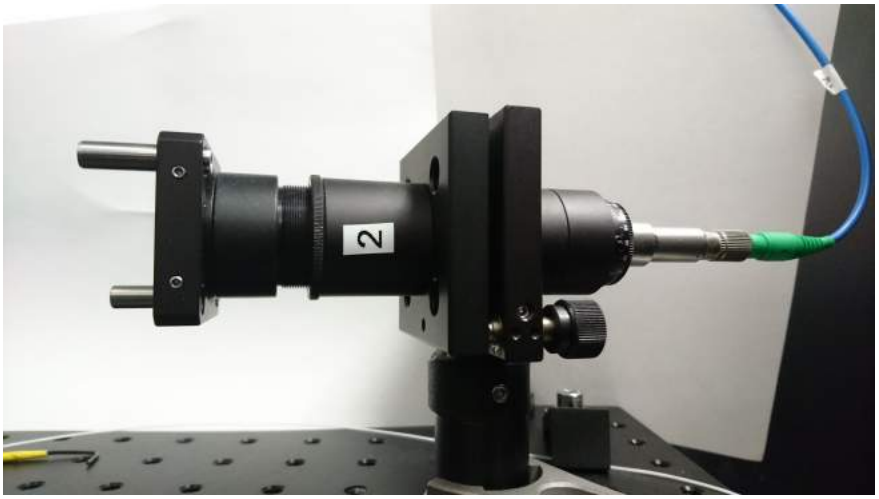

Fig. 3.9 A MOT outcoupler used to expand the beam out of the fibre and collimate it. A total of 6 MOT outcouplers are used to create the 3D MOT. Light from the fibre originates from the fibre couplers shown in Figure 3.8.

The 3D MOT is formed similarly to the LVIS, using one pair of magnetic coils in an anti-Helmholtz configuration which are also cooled using circulating water to prevent overheating. A built in safety switch disconnects the MOT coils if their temperature rises above 50 °C to prevent damage to components. Retro-reflection is not used for the 3D MOT, as balancing power between the pairs of beams is much more critical when transferring atoms to a molasses and later a dipole trap.

Six beams are coupled into separate fibres before being expanded and collimated to a diameter of 18 mm with a power of 20 mW using MOT outcouplers shown in Figure 3.9. The benefit of the outcouplers arises from the lens tube design, ensuring that all optics are aligned to each other and to the beam. Additionally, light out of a fibre has a Gaussian wavefront and the well aligned lenses will only cause small distortions leading to a uniform trap intensity. As space is not a primary concern, a minimal number of lenses are used to further prevent beam distortion. Light is permitted to expand naturally out of the fibre and is collimated using a single lens. As a result, the MOT outcouplers produce uniform near identical beams. The lens tube is fixed on a kinematic mount, allowing for high precision positioning in two dimensions. No finer adjustment is required due to the robustness of the MOT. Equal power

is sent to each pair of MOT outcouplers by using a $\lambda/2$ waveplate combined with a polarising beamsplitter to send equal amounts of light to each fibre.

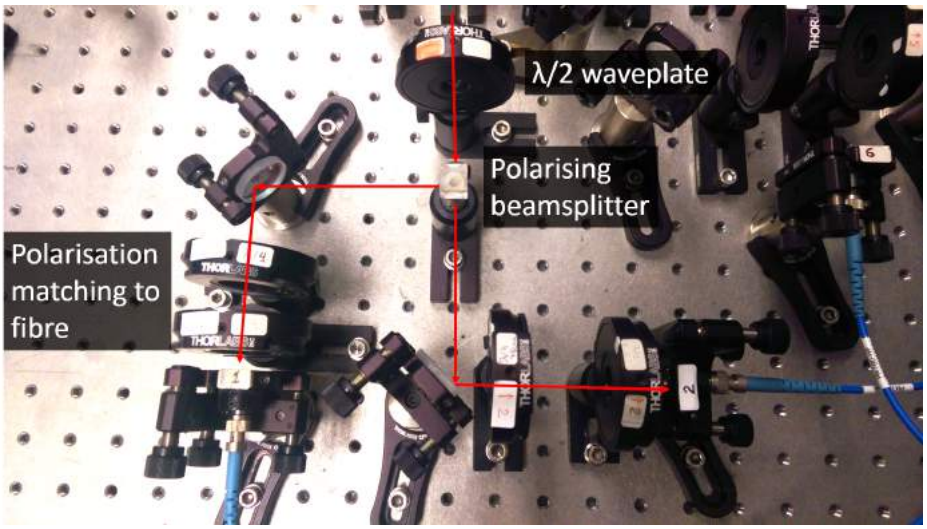

Fig. 3.10 An image of optics used to split light between two fibres in a manner that creates equal output power in both MOT beams after the fibre. The $\lambda/2$ and $\lambda/4$ waveplates before the fibre are used to match the polarisation of the incident light.

One such configuration is shown in Figure 3.10. Linearly polarised light enters from the top of the image into the first waveplate. Adjustment of the waveplate allows full control over the fraction of light split into each fibre using the polarising beamsplitter in the centre of the image. A combination of a mirror and fibre fixed to a kinematic mount are adjusted to find the greatest coupling efficiency of light into the fibre. Finally, the $\lambda/2$ and $\lambda/4$ waveplates are used to match the polarisation axis of the light to the fibre. Akin to the LVIS MOT, repumper light is combined with the cooling light and sent through one pair of outcouplers with 2 mW power each. Due to the large diameter and good collimation of the beams the resulting MOT is large, approximately 10 mm in diameter. The MOT is also visible to the naked eye, due to the fluorescence of photons from the cooling cycles explained in Chapter 2.2. An image showing the visible MOT during a loading sequence is shown in Figure 3.11.

3.7 Sequencing

Reliable imaging requires a very specific sequence of events that has to be repeatable with a high time resolution in order to generate accurate statistics about qualities of the trap such as size and temperature. To do this, the program Cicero Word Generator [105] is used to

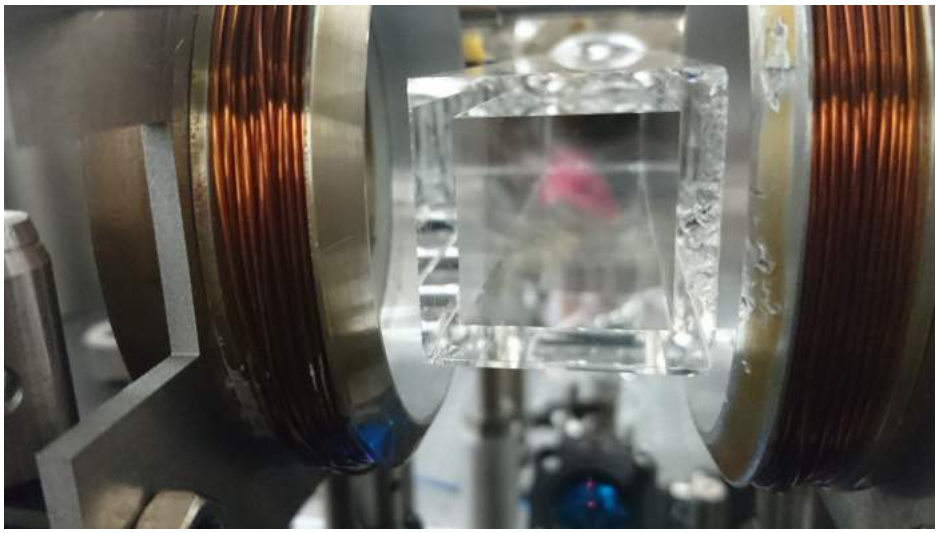

Fig. 3.11 An image showing a close up view of the cuvette. The 3D MOT coils are visible either side and a large cloud of cooled ^{87}Rb atoms is clearly visible in the centre as a fluorescing cloud. The non-uniform shape is a result of imperfect alignment of the MOT beams to the centre of the magnetic field and is not critical to the operation of the experiment.

create sequences that controls the entire experiment to a high degree of temporal accuracy and precision. An example of the Cicero user interface is shown in Figure 3.12.

All aspects of the experiment can be independently controlled from Cicero, allowing for quick changes and rapid optimisations of different configurations of traps to be performed with ease. Cicero uses 2 analogue and 1 digital National Instrument distribution boards to control individual components of the experiment. The timings of the sequence are controlled by an FPGA clock with a frequency of up to 150 MHz, allowing for a time resolution in the order of 0.01 ms. The major advantage of using the Cicero program lies in its variable time resolution. A typical sequence length of 10 s with a time resolution of 0.01 ms would yield a total of 10^6 time steps that require generating every time the sequence is executed. As large parts of the sequence involve no change of variables, such as the MOT loading or evaporation steps, these can be given much larger time resolutions to vastly reduce the number of time steps that require generation.

The first step in the sequence is titled “load MOT” and is used to build a sufficient reservoir of trapped atoms in the MOT whilst keeping the duration of the sequence short. During this step the magnetic field and light from the cooling, repumper and dipole trap laser are switched on, forming a MOT using techniques described in Chapter 3.6. After this step, the frequency of the cooling light is further detuned away from resonance by 200 MHz in a linear ramp in a

Fig. 3.12 Typical screenshot of a Cicero sequence. Analogue outputs appear in the middle of the image, each separate output is independently controlled with a range of voltages of ± 10 V. Digital outputs are below and controlled with an on/ off toggle switch providing +5 or 0 V respectively. The horizontal axis represents increasing time in the sequence.

time of 40 ms. The additional detuning brings the resonance of the cooling light close to the F' = 2 line and is known as a "dark" MOT. Detuning reduces the re-absorption of scattered light, thus reducing the radiation pressure and subsequently increasing the density of the MOT by up to a factor of 10 [106]. Simultaneously, the repumper intensity is reduced to a point where the majority of atoms are populating the F = 1 state. Fewer resulting interactions results in a temporarily colder MOT temperature. The magnetic field gradient of the 3D MOT coils is also reduced as it was found to increase the number of atoms loaded into the dipole trap.

Removing the RF signal supplied to the AOM to zero attenuates the laser light coupled to the fibres by 2 orders of magnitude. However, the remaining light can be sufficiently large enough to disrupt and excite trapped atoms, resulting in atom loss. Minimising this is achieved using mechanical shutters designed from simple physical relay switches that physically block the light with an average time-to-close of 10 ms and a delay of 15 ms. A useful feature of Cicero allows the delay between sending a signal to the shutter and the shutter beginning to move to be mitigated by applying the signal earlier than requested. This ensures that the shutters close as soon as possible when required. Mechanical vibrations

caused by the moving shutters are minimised by using a layer of foam between the shutter and the optical table. Additionally, the optics used to generate the cooling, repumper and imaging light for the LVIS and 3D MOT are situated on a separate table from the main science chamber, ensuring that any vibrations caused by the shutters are not transmitted to trapped atoms.

The subsequent step switches off the cooling and repumper light, allowing atoms to be transitioned into the dipole trap. Additionally, the frequency of the cooling light is returned to its normal position, allowing it to be relocked ready for the next sequence. All other light to the atoms is switched off at this point using mechanical shutters, and the atoms in the dipole trap are held for roughly one second in order to ensure that all atoms not trapped by the dipole beams have dissipated and a stable trap has formed.

A Bose-Einstein Condensate is then formed exclusively optically using evaporative cooling. The intensity of the dipole beam is reduced exponentially over a time period of 5 seconds from 12 W to 30 mW. This reduces the trapping potential experienced by the atoms. Any hotter atoms will escape the trap and are lost whilst colder atoms will continue to be trapped. By reducing the potential exponentially the process is adiabatic and atoms are not excited.

Imaging consists of several short steps. Initially, the dipole beam is switched off and the cloud of trapped atoms is given time to expand in a step titled “time of flight”. During this time there is no force acting on the atoms except for gravity, hence they fall and expand. Secondly, imaging light resonant with the F’ = 3 transition passes through the cell such that it is incident on the CCD and then a trigger is sent to the camera which takes an image of the trap with an exposure time of 50 µs. After a pause of 3 ms, the same process is repeated without atoms present to generate a background image. Both of these images are sent to a separate computer where a python script automatically subtracts the two images and applies a fit to generate accurate information about the trap.

3.8 Imaging

Two methods of imaging are available to use in the experiment. Fluorescence imaging is a useful technique that detects resonant photons deflected from a probe beam. Fluorescence imaging produces large signals and requires no additional optics. However, the long illumination time in the order of several ms results in poor spatial resolution and so

fluorescence imaging should only be used in cases with very low signal, such as trapping single atoms [107] or ions [108].

The second method is absorption imaging, and is much better suited for imaging a BEC. Absorption imaging provides a high signal-to-noise ratio and information regarding number of atoms, temperature and density. A laser beam resonant with the $5S_{1/2}$ F=2 $\Rightarrow$ $5P_{3/2}$ F'=3 is used as a probe to image the atoms. Resonant atoms will absorb the incident photons and will be observed as a shadow by the CCD camera. The quantity of light absorbed by the atomic cloud relays information on the optical density. For cold atoms above the critical temperature T_c the optical density is described by a Gaussian function as

$$OD_{Gauss}(x,y) = OD_{peak}\exp\left[-\frac{1}{2}\left(\frac{x-x_c}{\sigma_x}\right)^2 - \frac{1}{2}\left(\frac{y-y_c}{\sigma_y}\right)^2\right], \tag{3.2}$$

where σ_x and σ_y are the half-width at half-maximum of the atomic density distribution, OD_{peak} is the maximum value of the intensity and x_c, y_c are the spatial coordinates of the maximum intensity. A full derivation can be found in [109]. By fitting the Gaussian to the image, the number of atoms in the thermal cloud N_{th} is calculated as

$$N_{th} = (2\pi)^{3/2}\frac{OD_{peak}}{\sigma_0}{\sigma_x}^2(t)\sigma_y(t)\,. \tag{3.3}$$

The initial atom cloud temperature is calculated from the spatial distribution of the atomic density in the falling cloud [110] as

$$T = \frac{2{\tau_r}^2}{1+3{\tau_r}^2}T_r + \frac{1+{\tau_z}^2}{1+3\tau_z^2}T_z\,, \tag{3.4}$$

where

$$T_i = \frac{m}{2k_B}\left[\frac{\omega_i^2{\sigma_i}^2(t)}{1+{\tau_i}^2}\right] \tag{3.5}$$

and $\tau_i = \omega_i t$ for $i = x, y$.

The corresponding drop in laser intensity can be calculated using the Beer-Lambert law, given as:

$$I = I_0 e^{-A}, \tag{3.6}$$

where A is the optical density of the atomic cloud and I_0 is the initial intensity of the probe light.

Similarly the number and optical density of atoms in a Bose-Einstein Condensate is calculated using the Thomas-Fermi distribution, derived in Chapter 2.6. Here the optical density is given as

$$OD_{TF}(x,y) = OD_{TF\,peak} \max\left\{0, \left[1 - \left(\frac{r-r_c}{R_r}\right)^2 - \left(\frac{z-z_c}{R_z}\right)^2\right]^{3/2}\right\}. \tag{3.7}$$

R_z and R_r are the radius in the radial and axial directions respectively. $OD_{TF\,peak}$ is the maximum amplitude of the condensate optical density. The initial temperature of the BEC is calculated in Equation 3.4. The number of atoms in the BEC is the summation of the number in the pure BEC N_{BEC} and the number in the thermal fraction, N_{th}. N_{BEC} is given as

$$N_{BEC} = \frac{8}{15}\pi \frac{OD_{TF\,peak}}{\sigma_0} {R_r}^2(t) R_z(t). \tag{3.8}$$

A schematic of the imaging setup optics is shown in Figure 3.13 where a pair of lenses magnifies the image by a factor $f_2/f_1 = 2.67$ to provide better imaging of the BEC. The entire lens system is housed in a lens tube, ensuring a good alignment of the imaging light to the lenses. Light exiting the fibre is collimated to a diameter of 28 mm with a power of 100 µW, significantly below the saturation intensity of the probe transition and avoids saturating the camera.

In this experiment the imaging exposure time is 50 µs, and is roughly 2 orders of magnitude quicker than the response time of the shutters used to block the probe light. For this reason an additional switch is used to attenuate the signal sent to the AOM which minimises the signal to less than 15 µW in less than 2 µs, ensuring a sharp, repeatable pulse of probe light with a stable intensity.

The detection pulse is sensitive to the F = 2 $\Rightarrow$ F' = 3 transition. During the time of flight, atoms will naturally decay into the F' = 2 state and thus be invisible to the detection pulse. To ensure all atoms are detected, immediately prior to the probe pulse a 100 µs pulse of

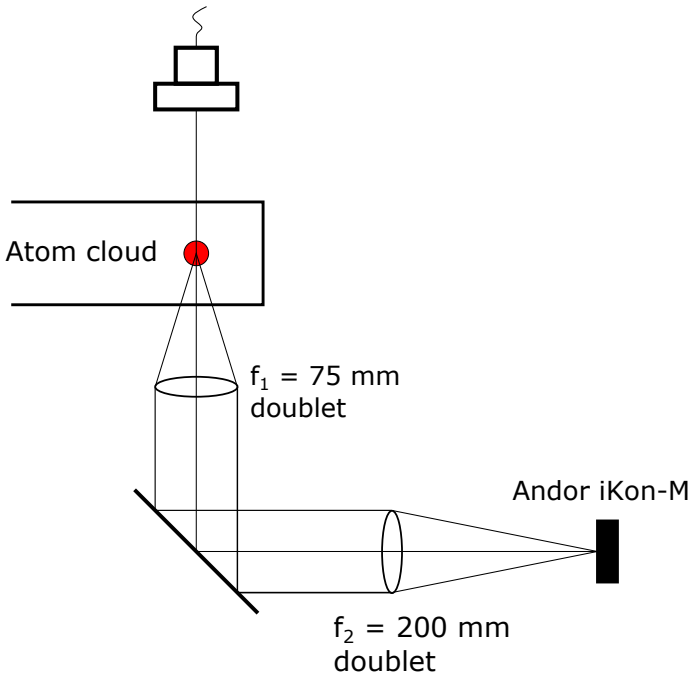

Fig. 3.13 Not to scale. A schematic of the setup used to image cold atoms in a dipole trap and a BEC.

repumper light, locked to the F = 1 $\Rightarrow$ F' = 2 is used to ensure that all atoms are pumped into the F = 2 state. However, this technique can not be used for imaging a BEC, as the additional pulse of repumping light will excite ground state atoms in the BEC and cause losses.

The camera used for imaging is an Andor iKon-M, chosen for its high quantum efficiency and fast readout speeds. The CCD is actively cooled to $-30\,^{\circ}$C and is specifically designed for ultra-cold atom imaging. Another feature of the camera is the fast file transfer, which allows for extremely quick imaging of the atoms and subsequent background. This works by only allowing a fraction of the CCD to be illuminated, with the rest physically blocked. In this experiment half of the CCD is blocked and half is illuminated, allowing two images to be taken in rapid succession. After the first image is taken, the pixel values are vertically shifted to the covered half of the CCD where the image is stored temporarily. The second image is taken and the hybrid image is read out as normal, an example of the two raw images taken is shown in Figure 3.14. As the imaging is destructive, when a second image is taken the atoms are dispersed. The minimum time between images is 3 ms and limited by the time taken for atoms to be blown away by the initial imaging pulse. The two images are subtracted from each other, significantly suppressing the background and yielding a greater signal-to-noise ratio for the atoms. However, the optical system will be subject to change between the two

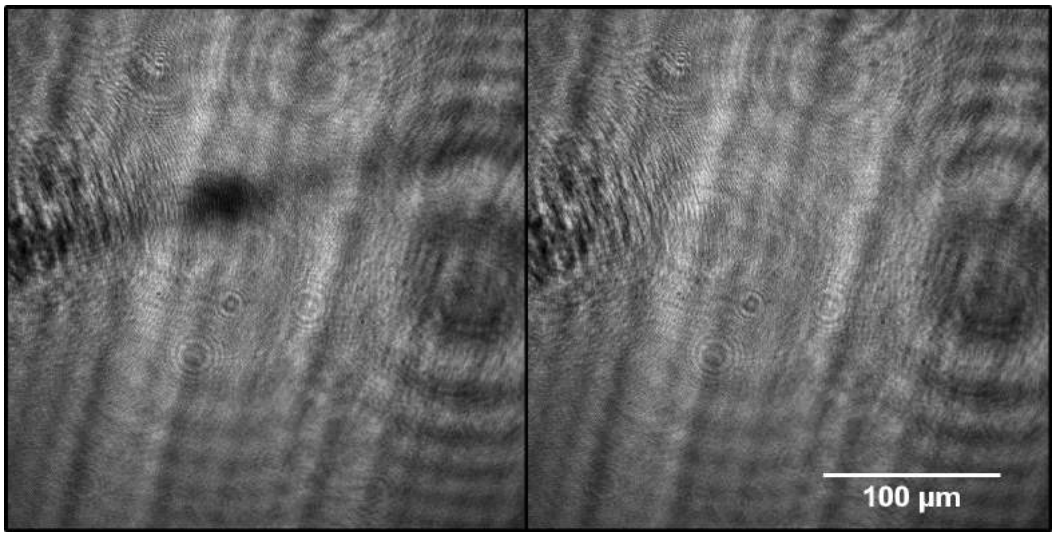

Fig. 3.14 An example raw image of the dipole trap with an accompanying background image taken 3 ms after the first. The dark spot near the centre of the first image is the shadow cast by atoms in the dipole trap on the CCD camera. Several diffraction patterns are present and arise from varying sources. The uncoated glass walls of the science chamber provide parallel diffraction lines, whilst the circular patterns are most likely caused by dust or other impurities on the imaging lenses.

images. Most notably, the intensity of the probe beam is not actively controlled and vibrations in the lab also affect coupling into the fibre. This results in a regular diffraction pattern of parallel lines across the entire image. Shorter time between images allows for significantly reduced noise in the final image, necessitating the need for the fast file transfer.

In addition to the first two images, there is an option for a third image to be taken without imaging light and is also subtracted from the first image to remove any stray light incident on the CCD not originating from the imaging beam. Further noise reduction to remove the parallel lines can be achieved using a Fast Fourier Transform (FFT) to transform the image into sine and cosine components, revealing common frequency components. This is useful in analysing noise as parallel diffraction lines are transformed into a single spot in the FFT. A mask can be applied to suppress unwanted frequencies before an inverse FFT process returns the original image with reduced noise. An example is shown in Figure 3.15. Whilst effective, this process is time consuming, difficult to automate and only useful in extremely noisy images.

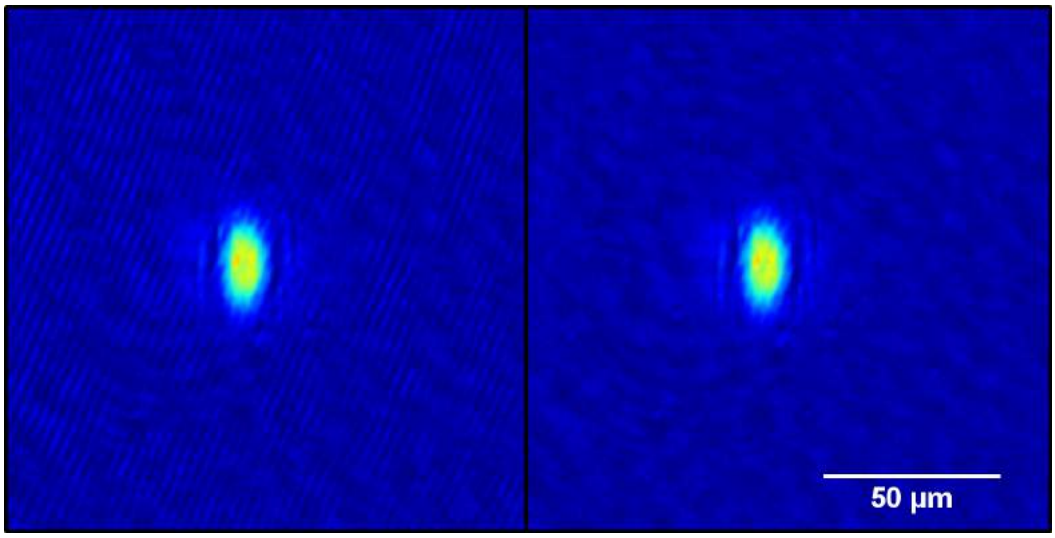

Fig. 3.15 Regular noise in the background of the first image displayed as parallel lines roughly 30° from vertical can be removed using a fast Fourier transform. After a mask is applied to unwanted frequencies, an inverse FFT is performed and the final image is shown on the right.

3.9 Lifetime Measurements in a dipole trap

Atoms held in a trap will naturally decay over time through several mechanisms. All must be addressed to ensure no appreciable loss in atom number over the length of a single experimental cycle.

Firstly residual atoms at room temperature in the science chamber will collide with the cold sample. As the trap depth of the dipole trap is less than 1 mK, any collision will result in the atom being lost cleanly from the trap without any further collisions. There is a possibility for a glancing collision transferring energy to the trapped atom and remaining trapped but this can be considered to be negligible due to the relatively shallow trap depth [111]. The rate of these losses is directly proportional to the quality of the vacuum.

Another mechanism for atom loss is through variation in the trapping potential, either by a point or intensity instability. The exact effect of this is hard to measure, but steps are taken to minimise their effects. For example high quality mirrors and accompanying mirror mounts are used to dampen vibrations that lead to increases in point instability. Additionally, all mechanical shutters are isolated from the main experimental table as an extra precaution against vibrations. To address the intensity instability, a PID feedback loop was implemented allowing the intensity variation of the laser to be damped via control of an AOM.

Finally, the spontaneous scattering rate of trapped photons can cause fluctuations in the radiation force of the trap owing to its random nature. As the light is far detuned from resonance the scattering rate is low and means that the energy of the emitted photon is proportional to the frequency of the laser as opposed to any optical transitions. The increase in energy to the system is represented by the recoil energy, given as $E_r = k_B T_r/2$, per scattered photon [80]. Frequency fluctuations of the dipole trap beams leads to fluctuations of the potential depth of the trap and leads to heating of the atoms.

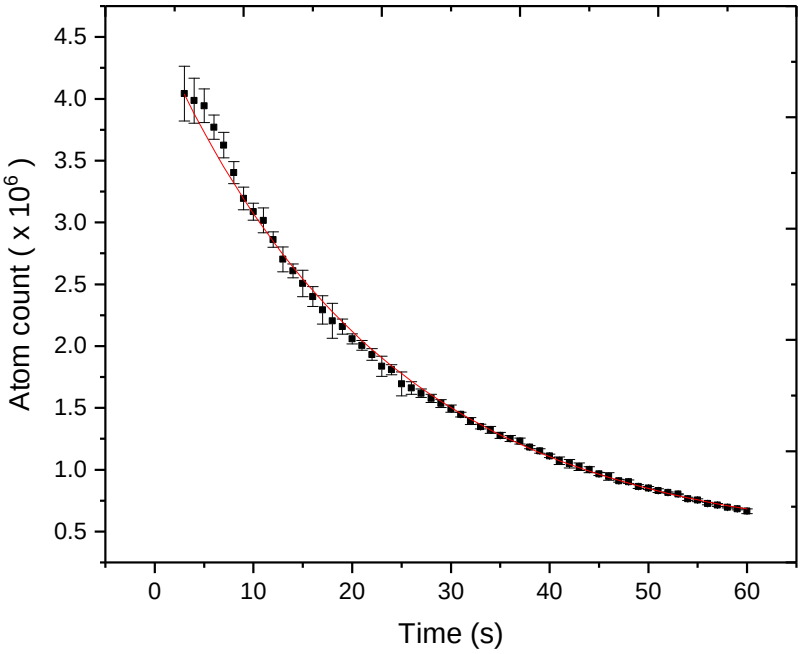

Fig. 3.16 Lifetime measurement of atoms in the dipole trap. The red line indicates an exponential fit yielding a half-life decay rate of 22.9 ± 0.4 s.

Measuring the lifetime of atoms in the dipole trap is achieved by forming a MOT with two dipole beams intersected through it as described in Chapter 3.11. After a period of loading, power to the MOT is removed leaving the dipole force as the only trapping potential to the atoms. Over time atoms will exit the trap via one of the mechanisms noted above. Figure 3.16 shows the resultant exponential decay in atom number.

Table 3.1 Ziegler-Nichols PID Tuning

Control Type	K_p	T_i	T_d
P	$0.5K_u$	-	-
P I	$0.45K_u$	$T_u/1.2$	-
P D	$0.8K_u$	-	$T_u/8$
P I D	$0.6K_u$	$T_u/2$	$T_u/8$

3.10 Intensity Stabilisation of the Dipole Beam

Shallow potentials are required to form an optimal BEC, with atoms only just held against gravity. Any instability in the trapping potential at these shallow depths will result in atom loss. As the trapping potential is solely created from a single laser, the intensity must be strictly controlled to ensure minimal excitations. A Proportional, Integral and Derivative (PID) control system is a wide-ranging technique [112] used to smooth natural variations in intensity from the laser. A small fraction of light is taken from the dipole beam using an uncoated glass plate and is fed into a photodiode. The signal is then passed through a PID control circuit with variable settings for proportional, integral and derivative values given as K_p, T_i and T_d respectively. Optimal values are obtained using the Ziegler-Nichols method [113]. This heuristic method uses step by step instructions to dampen natural fluctuations. To begin, all three values are set to 0. The proportional gain setting "P" is increased until it reaches the ultimate gain K_u. At this point output of the control loop undergoes regular oscillations and the PID settings are set by K_u and the oscillation period T_u as shown in Table 3.1.

3.11 Optical Dipole Trap

The dipole trap is formed using a far off resonance red detuned beam with a wavelength of 1064 nm. It is focused to a waist of 60 µm from an initial beam diameter of 1.3 mm using a 250 mm achromatic doublet lens. The beam is recirculated with an orthogonal polarisation to form a cross trap with an angle α =22°. Using crossed polarisations prevents any standing wave formations in the crossing region. Reusing the beam allows for a higher intensity trap resulting in a greater trapping potential. It also increases the trap frequency along the weakest axis and provides stronger confinement, making the trapping potential more uniform for a

crossing angle approaching normal. Initial power in the dipole trap is 18 W with losses from the uncoated cell walls reducing the return beam to 16 W. The trap is aligned to overlap with the MOT, with exact positioning inconsequential as the MOT size is significantly larger than the dipole trap.

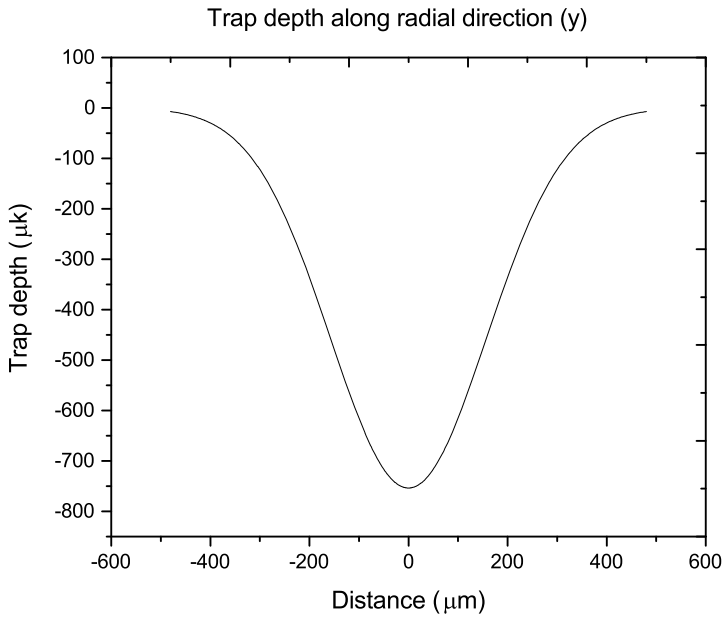

Fig. 3.17 Trap depth along the radial axis generated by a crossed dipole trap.

The potential produced by the dipole trap is elongated due to the shallow crossing angle but produces a trap depth of 750 μK. A numerical calculation of the trap depth along the direction of propagation of the incoming dipole trap beam is shown in Figure 3.17. The high intensity trap results in a negligible gravity contribution. By measuring the position of trapped atoms oscillating in the dipole potential, the axial frequency of the trap can be determined. Likewise, an adiabatic magnetic field gradient made to atoms stationary at the centre of the potential will cause a transverse oscillation and is measured. The corresponding axial and transverse frequencies are measured as 3.11 ± 0.07 Hz and 186 ± 14 Hz respectively.

After the MOT has grown to a sufficient size, several steps are taken to maximise atom transfer to the dipole trap. Firstly, power to the 3D MOT anti-Helmholtz coils is ramped down linearly over 30 ms meaning atoms are now only trapped by six MOT beams in a state known as an optical molasses. Simultaneously, additional detuning is performed on the MOT light to provide additional cooling before transfer to the dipole trap in a process described in more detail in Chapter 3.7.

The dipole trap beam is active whilst the MOT is loading allowing maximum transfer to the dipole trap. Loading the dipole trap is an exponential process with a rapid decay in additional trapped atoms because it is directly proportional to the MOT loading rate as they are loaded simultaneously. Figure 3.18 shows the number of atoms in the dipole trap as a function of loading time of the MOT up to a maximum 5 seconds. Loading for 4 seconds, or 5τ, yields a consistently high number of atoms with a high confidence interval.

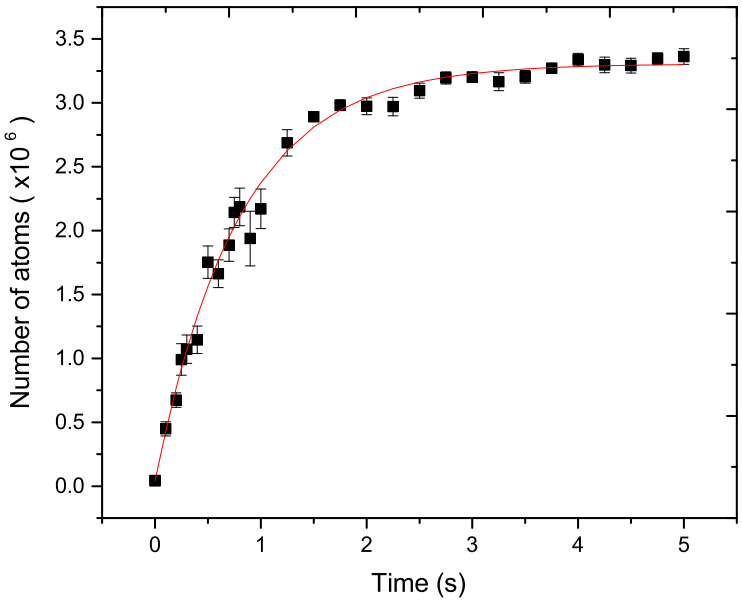

Fig. 3.18 Loading rate of the MOT, measured by the number of atoms confined in the dipole trap. Direct measurements of the MOT size are difficult as it rapidly grows larger than the imaging area. The red line represents an exponential curve where the time constant τ is given as 0.80 ± 0.02 s

Light from the MOT is switched off to allow atoms trapped in the arms to travel closer to the centre of the trap in a process that lasts for up to 1 second resulting in up to 5×10^6 trapped atoms with an average temperature of 5 µK. The corresponding phase space density is 3.31×10^{-5}. An example image of a dipole trap is shown in Figure 3.19 with accompanying Gaussian fits in both axes.

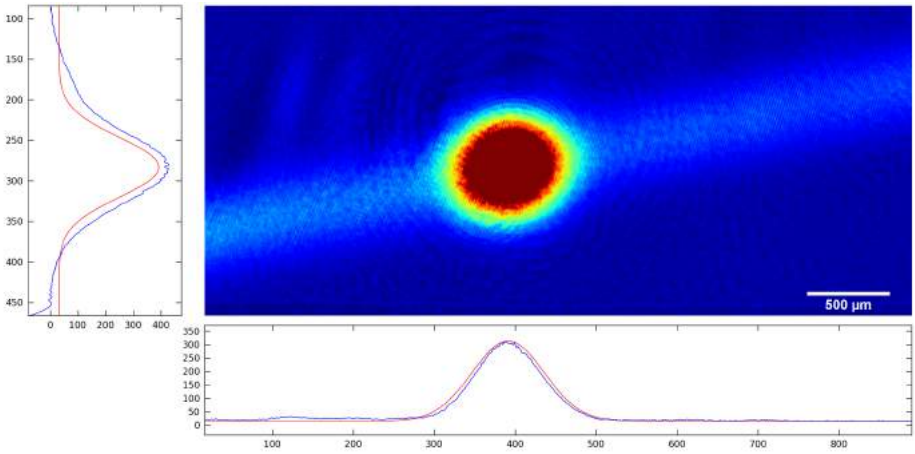

Fig. 3.19 An image of a dipole trap taken after 3 ms time of flight. More energetic atoms can be seen in the arms of the trap, with a majority trapped at the intersection between the two dipole beams.

3.12 All-Optical Production of a Bose-Einstein Condensate

Producing a BEC in an all-optical way remains experimentally challenging and requires a large source of pre-cooled atoms. The work detailed below represents the first BEC attained at NPL, and is a significant milestone within the experiment itself.

Additional cooling to atoms already trapped in a dipole potential can be provided using exclusively optical methods [114] through slowly reducing the potential depth over a period of 5 s to systematically remove atoms in the higher energy states of the trap. This is achieved through an exponential reduction in the intensity of the dipole trap. Power in the dipole trap is adjusted via an AOM controlled by an intensity stabilising PID circuit. The system modifies intensity in discrete steps corresponding to a power change of several mW. In the context of an exponential decrease in power, it allows atoms in the new trap with a reduced potential to thermalise. Atoms return to the standard density of states distribution in Equation 2.31, but with a lower average energy. Reducing the trap potential also has the side effect of reducing the trap frequency ω by the relation $\omega \propto U^{0.5}$ where U represents the potential depth. Additionally, the evaporation rate is directly affected by the elastic collision rate and decreases as ω decreases [115]. An example image taken from the experiment is shown in Figure 3.20.

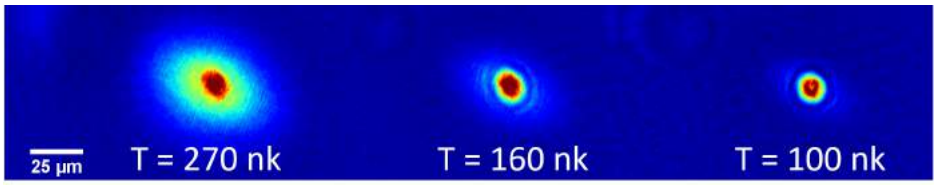

Fig. 3.20 Composite experimental image in false colour showing effect of continually decreasing the dipole potential, eventually leaving a pure BEC.

The dipole beam minimum waist of 60 μm is useful when creating a dipole trap as a large trapping area is required to confine a sufficient number of atoms. However, this leads to a relatively shallow potential when the intensity is reduced for evaporative cooling.

Limits on the evaporation rate can be approximated by comparing two scenarios. Firstly where trap depth is reduced too quickly, meaning atoms have insufficient time to thermalise making the process less efficient. Alternatively if trap depth is reduced too slowly, loss of particles through inelastic collisions becomes significant, also making the evaporation process inefficient. Therefore, an optimal evaporation time must exist and can be calculated using the principle of detailed balance [116]. This considers atoms with density n_0 in a box potential with a large trap depth, denoted by η. Detailed balance states that elastic collisions leads to atoms with an energy larger than $\eta k_B T$ with a rate given by number of atoms with energy in excess of this as a fraction of their collision time. Velocity of atoms with an energy of $\eta k_B T$ is $\sqrt{2\eta kT/m} = \bar{v}\sqrt{3\eta/2}$, where $\bar{v}$ is the average thermal velocity of the atoms. For a sufficiently large η, the fraction of atoms in the Maxwell-Boltzmann distribution with $\varepsilon > \eta$ is given by

$$f(\varepsilon > \eta) = e^{-\eta}\sqrt{\frac{3\eta}{2}}. \tag{3.9}$$

The elastic collision rate is $k_{el} = n\sigma v$ where σ is the elastic collision cross section. The rate of evaporated atoms can then be expressed as

$$\frac{dN}{dT} = -Nf(\varepsilon > \eta)k_{el} = -n\sigma\bar{v}\eta e^{-\eta}N \equiv -\Gamma_{ev}N. \tag{3.10}$$

As the average elastic scattering rate depends on the relative velocity but not the average velocity of atoms, the average elastic collision rate becomes $\bar{k}_{el} = 4n\sigma\bar{v}/\sqrt{3\pi}$. Therefore, the ratio of evaporation and elastic collision time is

$$\frac{\tau_{ev}}{\tau_{el}} = \frac{\sqrt{2e^{\eta}}}{\eta}, \tag{3.11}$$

giving a ratio with an exponential dependence with η. Once sufficient evaporation has taken place a few ultra-cold atoms with high density remain.

Measurements on the temperature will gain an insight into properties of the atoms but does not provide definitive proof that the atoms have condensed into a BEC as opposed to a cold thermal cloud. Heisenberg's uncertainty principle states

$$\Delta x \Delta p \geq \hbar/2, \tag{3.12}$$

where x is the position and p is the momentum of the particles. As the cloud of atoms cools adiabatically the position of individual atoms becomes increasingly uncertain, to the point where the wavefunction of the atoms begin to overlap. In keeping with the uncertainty principle, as atoms cool their kinetic energy and hence momentum decreases leading to an increase in position uncertainty. Furthermore, the confining potential experienced by the atoms is not uniform, with the higher trapping potential occurring along the axial direction of the trap resulting in greater position uncertainty. As a result when atoms are released and allowed to expand naturally, they will expand quicker in the axial direction than the radial and thus provides a good indication that atoms have condensed into a BEC. This effect is dominant for a small BEC with $N < 10^3$ atoms. For a larger BEC the interaction energy is stored anisotropically as a result of an unequal trapping potential along the radial and axial directions and also creates a size inversion [117]. A sequence of images showing the BEC expanding with increasing time of flight is shown in Figure 3.21.

Figure 3.22 shows a BEC 30 ms after release from the dipole beams. Tighter confinement along the axial direction causes the BEC to expand quicker along the radial direction, causing greater uncertainty in the momentum distribution. A Thomas-Fermi approximation is used to determine the size and temperature of the cloud, explained in detail in Chapter 2.6.

As the BEC is formed optically, atoms can be favourably loaded into any of the three magnetic sublevels $m_F = 0, \pm 1$, using applied magnetic field gradients during the evaporation. Figure 3.23 is a diagram explaining how the separate m_F states in the BEC are separated by applying a magnetic field gradient during the time of flight. The population of each sublevel can easily be examined using Stern-Gerlach spin separation. After abruptly removing the

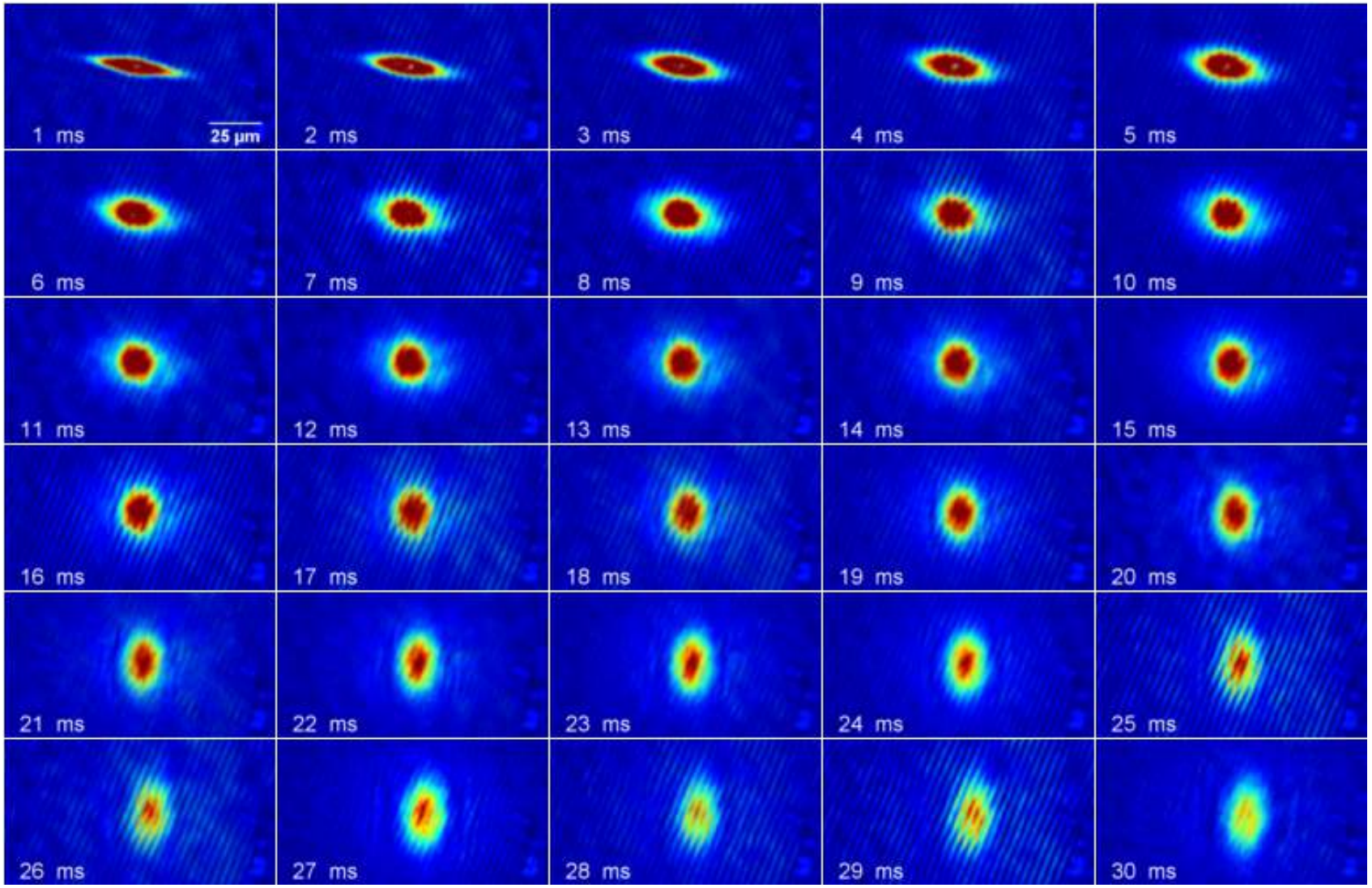

Fig. 3.21 A sequence of images to show the evolution of a BEC as it expands during time of flight. The BEC is initially trapped close to the vertical axis. Once the trapping potential is removed the cloud expands anisotropically as a result of Heisenberg's uncertainty principle, see Equation 3.12.

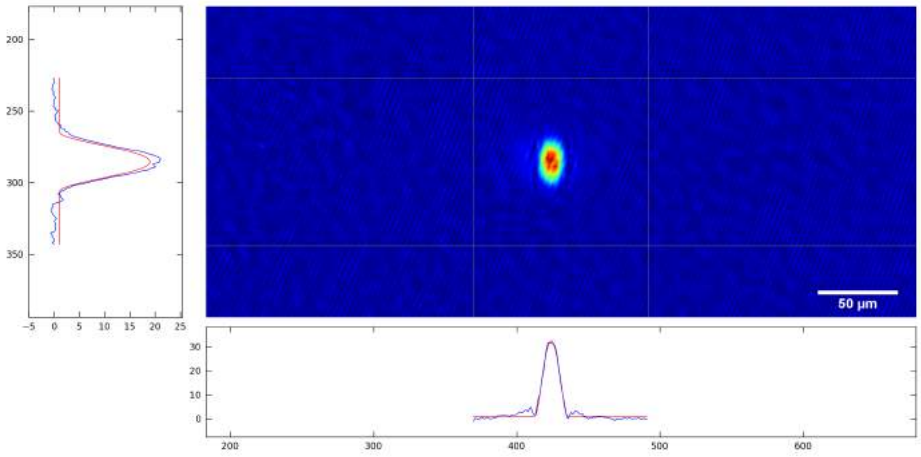

Fig. 3.22 Absorption image of a BEC containing 5×10^4 atoms taken after 30 ms time of flight. The trapping dipole beams are oriented along the horizontal axis and therefore create a stronger trapping potential. As a result atoms expand faster along the vertical axis once the trapping potential is removed.

optical dipole trapping potential, the BEC is permitted to expand for up to 5 ms time of flight. The cloud expands radially before a magnetic field gradient is applied to separate the m_F states spatially. More time of flight is permitted to allow a greater separation between states. The separation is dependent on the strength and duration of the magnetic gradient and the length of the time of flight. Figure 3.24 shows three separate images. Figure 3.24a is taken during a normal evaporation cycle, with a magnetic gradient applied during time of flight. The majority of atoms are loaded into the $m_F = +1$ state with a smaller number in the $m_F = 0$ and very few in $m_F = -1$. Atoms in $m_F \pm 1$ can be identified by the direction they travel in the influence of a magnetic field from a single coil. The coil creates a region of high magnetic field, attracting atoms in $m_F = -1$ and repelling atoms in $m_F = +1$.

If a magnetic field gradient is applied during the evaporation, atoms in the $m_F = \pm 1$ states are evaporated faster and the $m_F = 0$ state is exclusively populated, shown in Figure 3.24b. A graphical representation is shown in Figure 3.25, where the fraction of atoms in each m_F state is displayed as a function of length of evaporation time. Figure 3.25a displays the population of m_F states when no additional bias field is applied. The majority of atoms are naturally loaded into $m_F = +1$ as a result of small existing magnetic field gradients. Figure 3.25b has an additional bias field applied by increasing the current in one of the compensation coils used to cancel the Earth's magnetic field. The bias is applied from the start of the evaporation and atoms in $m_F = +1$ are immediately suppressed with a roughly equal population of atoms in $m_F = 0, -1$. Early in the evaporation sequence the trapping potential from the optical

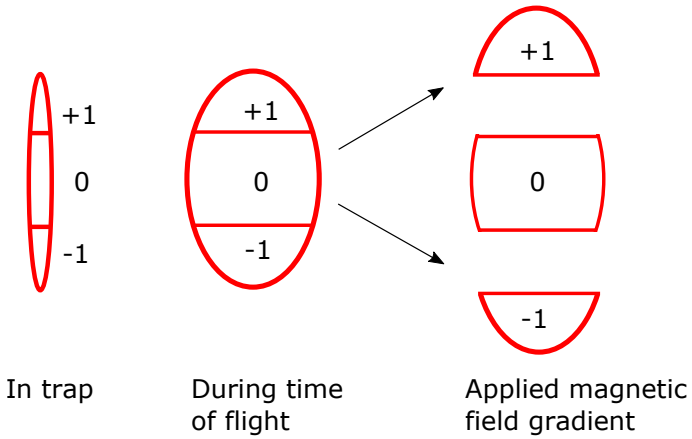

Fig. 3.23 Diagram to show how the different m_F states in the BEC can be individually probed. Initially after release the BEC expands radially before a magnetic field gradient is applied to split the cloud into component m_F states. Finally, a probe beam is used to image the atoms as shown in Figure 3.24.

dipole beams is sufficient to keep atoms in all m_F states confined. However, at around 4.5 s the potential is sufficiently weakened for the applied bias field to selectively remove atoms in the magnetically sensitive states.

After this point virtually 100% of atoms exist in the magnetically insensitive $m_F = 0$ state, meaning full control over the m_F states of atoms in the BEC is achievable. However, this process leads to a significantly reduced BEC atom number as the majority of atoms in magnetically sensitive states are removed, leading to large losses. Typically, a BEC loaded into $m_F = 0$ will contain half the number of atoms as a spinor BEC with $> 90\%$ of atoms in a single magnetically sensitive state. However, the BEC is required to be in a magnetically sensitive state for experimental work described in more detail later. To this end efforts were made to load the majority of atoms into $m_F = +1$ by adjusting the bias coils used to cancel the Earth's magnetic field. Figure 3.24c shows $> 90\%$ of atoms loaded into the $m_F = +1$ state after optimisation.

3.13 Estimating the Temperature of the BEC

The temperature of a BEC can be difficult to ascertain, due to the large momentum uncertainty of the atoms and the thermal fraction of atoms surrounding the BEC. The most common approach to estimating the temperature of an atomic cloud is a time of flight (TOF)

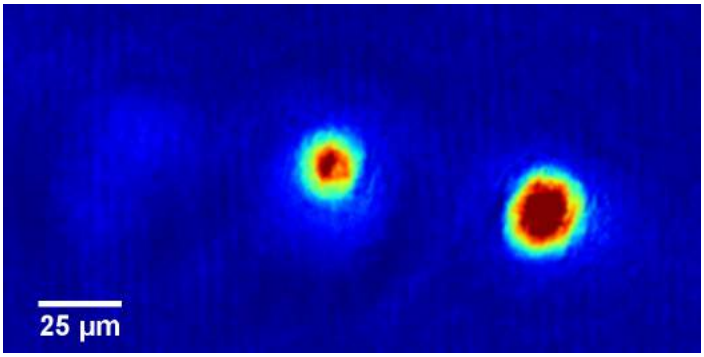

(a) The BEC is loaded as normal.

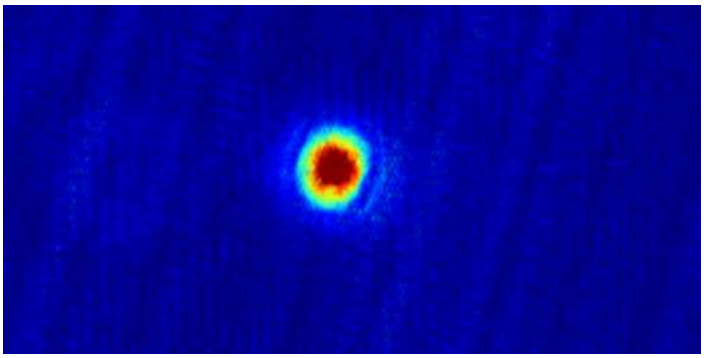

(b) A strong magnetic field gradient is applied during evaporation.

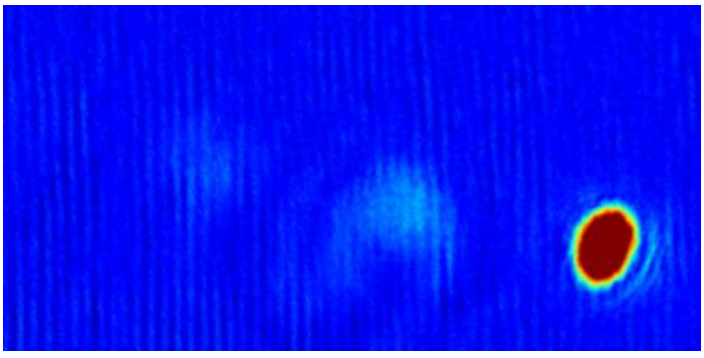

(c) Optimised loading into $m_F = +1$.

Fig. 3.24 After creating a BEC a magnetic field gradient is applied during the time of flight to split the BEC spatially into its three m_F components. From left to right the magnetic sublevels are $m_F = -1, 0, +1$. The distribution of atoms in Figure 3.24a represents the population in each m_F state when the BEC is loaded as normal. In Figure 3.24b a magnetic field gradient is applied during the evaporation to remove magnetically sensitive atoms. Figure 3.24c shows atoms favourably loaded into the $m_F = +1$ through adjustment of the bias coils.

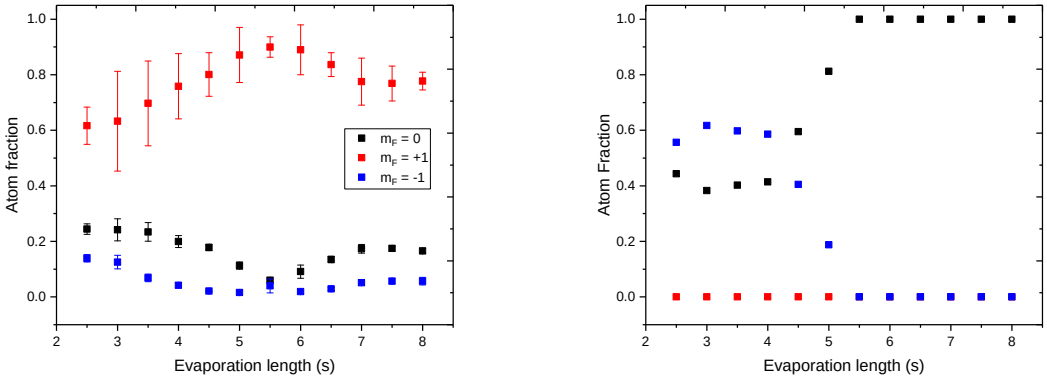

(a) (b)

Fig. 3.25 The fraction of atoms in each m_F state as a function of evaporation length displays how applying a bias field can drastically alter the population of each state. Data is taken from a minimum of 2 seconds of evaporation as the total atom number is too large above this point, and the three magnetic sublevels are unable to be resolved.

(a) Population of m_F states with no additional applied bias field. The majority of atoms are loaded into $m_F = +1$.
(b) An additional bias field is applied during the evaporation causing a majority of atoms to exist in the magnetically insensitive $m_F = 0$ state.

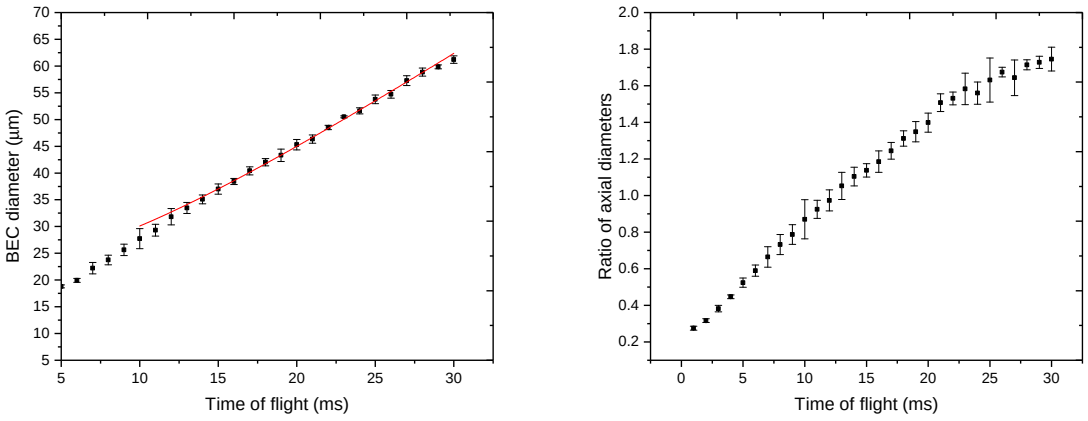

(a) Temperature measurement.

(b) Inversion of BEC axial diameter.

Fig. 3.26 Figure 3.26a shows a temperature measurement of the thermal fraction of a cloud containing a BEC, plotting cloud diameter as a function of time of flight. Using Equation 3.15 a polynomial fit to the data is made, and the corresponding temperature is calculated as 39.0 ± 0.3 nK, well below the critical temperature T_c required for atoms to condense into a BEC. Figure 3.26b displays the ratio of the two axial diameters of the BEC and shows an obvious inversion created due to Heisenberg's uncertainty principle described further in Chapter 3.12.

measurement [118]. An accurate temperature measurement is achieved by measuring the spatial distribution of the atomic cloud whilst it is falling under gravity and with no other forces acting upon it. The velocity distribution of the atomic cloud can be described with a Maxwell-Boltzmann distribution as

$$f(v_x) = \left(\frac{m}{2\pi k_B T_x}\right)^{0.5} \exp\left(\frac{-mv_x^2}{2k_B T_x}\right), \tag{3.13}$$

where m is the mass of a single Rubidium atom and T_x is the temperature of the atomic cloud. Assuming the cloud is of uniform temperature its position can be described with the Gaussian distribution:

$$P(x_i) = \frac{1}{\sqrt{2\pi\sigma_x}} \exp\left(\frac{-x_i}{2\sigma_x^2}\right). \tag{3.14}$$

The cloud expands as it falls and the rate of expansion is proportional to the temperature of the atoms as

$$\sigma_x(t) = \sqrt{\sigma_x^2 + \frac{k_B T_x}{m} t^2}, \tag{3.15}$$

as described in [119]. Figure 3.26a shows an example of a temperature measurement of atoms condensed into a BEC by plotting the $1/e$ diameter of the BEC as it expands during time of flight. The temperature is derived from the gradient of the fitted curve using Equation 3.15. Figure 3.26b shows a graphical representation of the axial inversion of the BEC when permitted to expand under time of flight, shown as a sequence of separate images in Figure 3.21.

3.14 Conclusions

This chapter details the significant upgrades to the experiment that were critical for the production of a BEC. Both lasers responsible for providing the repumper and cooling light were replaced with higher intensity equivalents. The increase in power enabled the total illuminated area of the MOT to be larger, which in turn trapped more atoms. Dedicated outcouplers for the MOT beams with simple lens tube designs also provided an increase in stability, and a more Gaussian wavefront. A new sequencing system allowed mechanical shutters to be pre-triggered, mitigating their rise and fall time and ensuring no light enters the cuvette when not required to a better temporal accuracy. Finally, a new camera system dramatically improved the quality of images acquired. A fast file transfer mode enabled much shorter times between the image and a subsequent background of 3 ms, reducing the interference fringes in the images caused by fluctuations in the probe beam intensity.

A single recirculating dipole beam with a power of 12 W creates a crossed dipole trap capable of trapping up to 5×10^6 atoms with an average temperature of 5 µK. The introduction of optical evaporative cooling selectively removes more energetic atoms from the trap, reducing the average energy. After evaporating for 5 s, the remaining atoms condense into a BEC, where the temperature of the surrounding thermal cloud is measured to be 39 ± 3 nK.

Chapter 4

Waveguides and Beamsplitter Implementation

Once a stable BEC source has been created, steps are taken to transfer the atoms into an optical waveguide where they will propagate and coherently split. The waveguide is derived from the same laser used to generate the dipole beams and is tightly focused at its waist. It holds the atomic sample in an optical potential with no reliance on magnetic fields. Two identical overlapping waveguides creates a periodic potential, the amplitude of which is dependent on the relative polarisation between the waveguides. The resulting band structure explained in Chapter 4.6 creates regions of high reflectance and atoms are deflected into the second waveguide depending on their initial velocity.

4.1 Generation of Optical Waveguides

To form a trapping potential, the wavelength of light for the waveguides must be red detuned relative to the atoms and be tightly focused. In this sense they are similar to the dipole beams used to form the dipole trap, but with significantly lower intensities. Because of this, the dipole and waveguide beams are derived from the same laser. Using the same laser mitigates interference arising from frequency fluctuations, helping to reduce excitations.

The laser used to form the waveguides is fibre coupled, and therefore emits a good approximation of a Gaussian beam, minimising the need for shaping optics. A schematic of the optical layout is shown in Figure 4.1. Two waveguides, referred to as WG1 and WG2, are generated

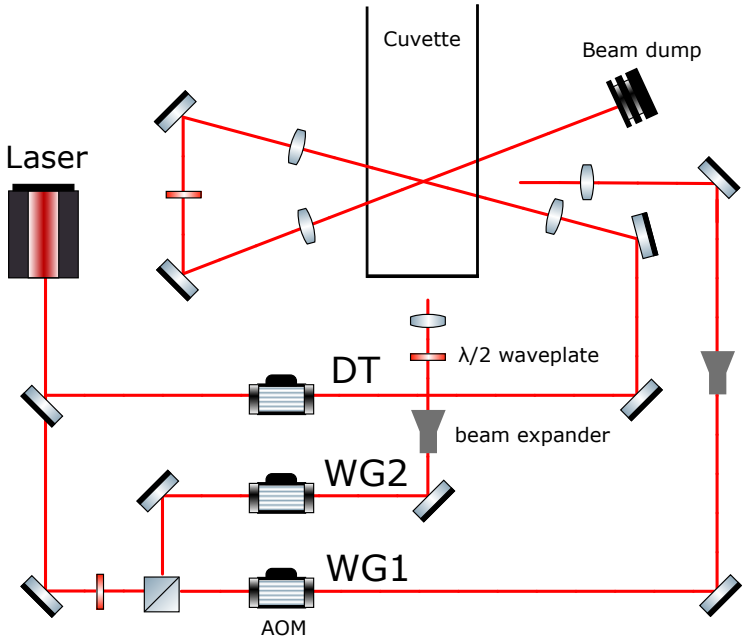

Fig. 4.1 Paths of the dipole trapping beam and the two waveguides. A single dipole beam is recirculated and crosses inside the science chamber. WG1 and WG2 intersect close to the dipole trap intersection. The photodiodes are used for independent power stabilisation.

using a fraction of light from the dipole beam before it passes through an AOM. The two waveguide beams then pass through two separate AOMs to allow independent control of their power. This has an additional advantage of shifting the frequency of the waveguides to the dipole beam by an additional 80 MHz, avoiding any cross interference. After the AOM, a small fraction of light is removed and sent to a photodiode for use in stabilising the intensity as described in Chapter 3.10. A $\lambda/2$ waveplate is used to create linearly polarised light before passing through a beam expander, increasing the diameter by a factor of 3, to 12 mm. A larger waist results in a smaller minimum beam waist when focused using the relation

$$2w_0 = \left(\frac{4\lambda}{\pi}\right)\left(\frac{f}{D}\right), \tag{4.1}$$

and is valid for $f \gg z_R$, where z_R is the Rayleigh length. w_0 is the minimum beam waist, f is the focal length of the lens and D is the diameter of the collimated beam.

The waveguide potential is affected by the minimum beam waist, intersection angle and intensity of the waveguides. Figure 4.2 shows the potential depth for a waveguide with a 23 µm waist and 15 mW of power intersecting a second identical waveguide with an angle

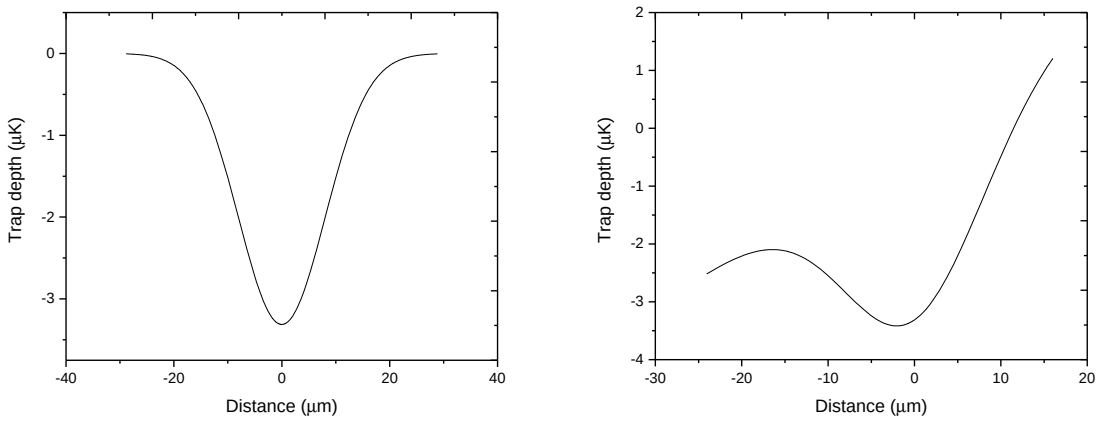

(a) (b)

Fig. 4.2 Potential depth of the waveguides along two axis for a 15 mW horizontal beam with a 23 μm waist. Figure 4.2a represents the potential along the direction of the waveguide. Figure 4.2b is the potential along the axis of gravity.

$\theta = 90°$. The trap depth is 5 μK along the axial direction of the waveguide. Due to the low power of the waveguides atoms are only weakly held against gravity with a trap depth of 2 μK. Fluctuations in intensity can be large enough to push atoms out without additional power stabilisation. Additionally, the waveguides must be horizontal to minimise the component of gravity. This is especially important once the BEC is released and permitted to travel along the length of the waveguide. If the waveguide is angled away from the horizontal gravity will impart an additional force on the atoms, causing them to be accelerated out of the waveguide. As it is difficult to guarantee the horizontality of the optical bench to the level of precision required, a kinematic mount provides additional alignment in the vertical axis. The best method of aligning the waveguide to be horizontal is to allow a BEC to propagate in the waveguide. It will naturally oscillate around the focus of the waveguide for a horizontal beam. Any vertical offset will cause the BEC to oscillate off centre. By adjusting the kinematic mount and monitoring the BEC oscillation a good approximation of a horizontal beam can be made.

4.2 Improved BEC Loading using Waveguides

WG1 will overlap with the crossed dipole trap, enabling the waveguide to serve a dual-purpose and help to load more atoms at a faster rate into a BEC state. A common technique used to

load more atoms into a BEC from a dipole trap is with the use of a dimple beam [120, 121]. This is an additional beam usually derived from the same laser to prevent excitations which also intersects at the dipole beam focus. Due to the low power in the dimple, its additional trapping potential is negligible when the dipole trap is formed. As the power is slowly lowered for evaporative cooling, the trapping potential from the waveguide becomes significant. The smaller beam waist of the dimple helps to spatially confine atoms as they undergo evaporative cooling, keeping density high. In this experiment, WG1 intersects the dipole beam 500 µm to 800 µm from the focus of WG1. The distance between the intersection and the focus of WG1 is typically less than one Rayleigh length. Increasing the distance beyond this point reduces the trapping potential felt by the atoms, to the point where they will fall out of the trap due to gravity. The Rayleigh length is calculated as

$$Z_R = \frac{\pi {\omega_0}^2}{\lambda}, \tag{4.2}$$

giving an effective maximum separation between the dipole beams and the focus of WG1 of 1.5 mm.

4.3 Transfer from the BEC

Once a BEC is formed in the dimple assisted trap, the dipole trap beams are abruptly switched off using the AOM shown in Figure 4.1. A diagram describing the relative positions of the dipole and waveguide beams is shown in Figure 4.3. The orientation is simplified to increase clarity. With the dipole beam off, WG1 becomes the sole trapping potential. Once released, the atoms can no longer be described as a BEC, but are instead an ultra-cold atomic wave packet, and are highly coherent. An adiabatic transfer to the waveguides will cause multiple transverse modes of the waveguide to be occupied. As the atoms are no longer in the centre of a potential, they will begin to accelerate towards the focus of WG1, a region of lower potential. After passing the minimum beam waist the atoms begin to climb the potential and start to oscillate. The oscillation is measured and used to calculate the axial frequency of the trap.

Measurements are taken of the BEC position as a function of time as it oscillates in WG1 and are shown in Figure 4.4. As absorption imaging is destructive a new BEC is required for each data point, necessitating a need to minimise the length of a full experiment cycle. Otherwise

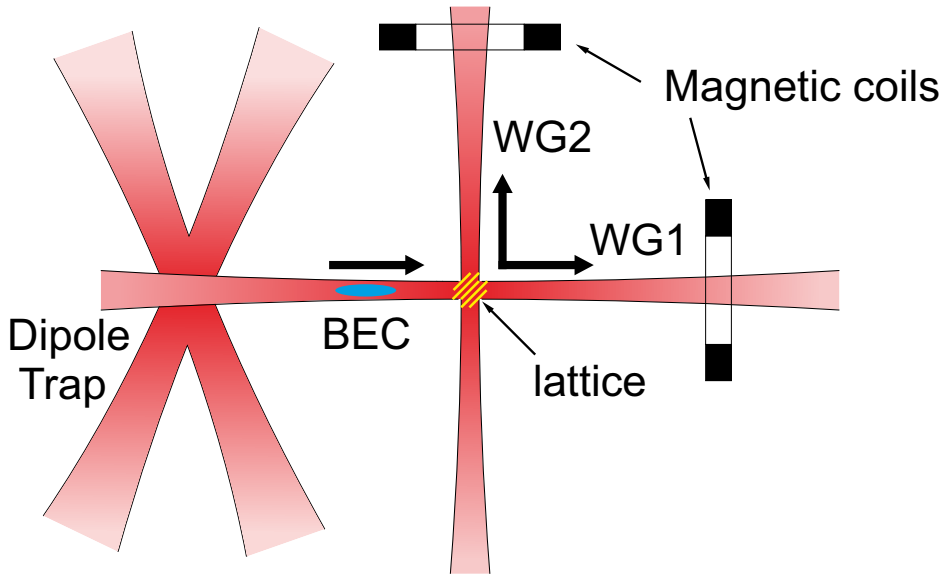

Fig. 4.3 Diagram to show how atoms are transferred from the optical dipole trap to WG1.

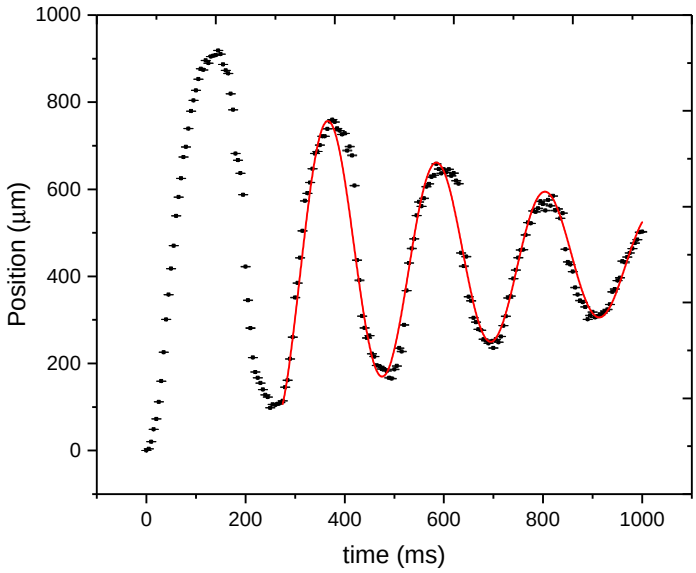

Fig. 4.4 The BEC is released from the dipole potential and begins to oscillate in WG1. A series of images are taken with propagation time increasing sequentially by 5 ms up to 1 s. A damped sinusoidal curve is fitted to the data yielding an axial frequency of 4.35 ± 0.02 Hz. The first oscillation is not included in the fit as the BEC and the large cloud of surrounding thermal atoms exhibit different behaviours and must thermalise before a good fit can be made.

it results in long total sequence times which leads to relaxation of optics, misalignment and fluctuations in beam power from varying coupling efficiencies into fibres. The sinusoidal motion of the atoms in WG1 is very clear, as is the exponential damping of the oscillation amplitude. This indicates that a small thermal fraction of atoms still exists around the BEC. The thermal atoms populate higher transverse modes within the waveguide, meaning a fraction of kinetic energy from the motion of the atoms is converted to a transverse momentum. As a result, the thermal fraction of atoms lags behind the BEC when allowed to oscillate in the waveguide. This leads to a rapid thermalisation of the BEC and causes the visible damping. The frequency change towards the end of the measurement is also caused by the thermal atom lag, as the centre of the thermal cloud in the waveguide becomes more uncertain. Fitting a sine curve to the data yields a frequency of 4.35 ± 0.02 Hz. Information on the minimum beam waist can be inferred from measurements of the axial trap frequency. Starting with the definition of the Rayleigh length from Equation 4.2, the waist along the beam axis defined as the y-axis of WG1 is given as

$$w_s = w_1 \sqrt{1 + \left(\frac{y}{z_R}\right)}. \tag{4.3}$$

If the crossing angle between waveguides is α, w_s can be rotated by $\alpha/2$ to give

$$w_{s,rot} = w_1 \sqrt{1 + \left(\frac{x \sin\left(\frac{-\alpha}{2}\right) + y \cos\left(\frac{-\alpha}{2}\right)}{z_R}\right)^2}. \tag{4.4}$$

The intensity of WG1 is therefore

$$I_1 = \frac{2P_1}{\pi {w_s}^2} \exp\left(-\frac{\left(2x \cos\left(\frac{-\alpha}{2}\right) - y \sin\left(\frac{-\alpha}{2}\right)\right)^2 + z^2}{{w_s}^2}\right). \tag{4.5}$$

The potential from WG1 including gravity is

$$U_1 = \frac{-\pi c^2 \Gamma I_1}{2 {w_0}^3} \left(\frac{2}{\Delta_1} + \frac{1}{\Delta_2}\right) + mgz, \tag{4.6}$$

where Δ_1 and Δ_2 are constants proportional to the wavelength separation between the red-detuned 1064 nm trapping laser and the resonant 780 nm light transitions, g is the acceleration

due to gravity and m is the mass of a ^{87}Rb atom. The potential from WG2 is derived in the same manner and their summation provides the total trapping potential.

Similarly, the radial frequency of the trap can be calculated by applying a short perturbation to the potential and measuring how atoms in the trap respond. A perturbation is applied by rapidly increasing power in WG1 for several μs before returning to normal power. The position of atoms is recorded over time and the resulting sinusoidal motion is shown in Figure 4.5. The radial frequency is therefore calculated as 186.6 ± 1.4 Hz.

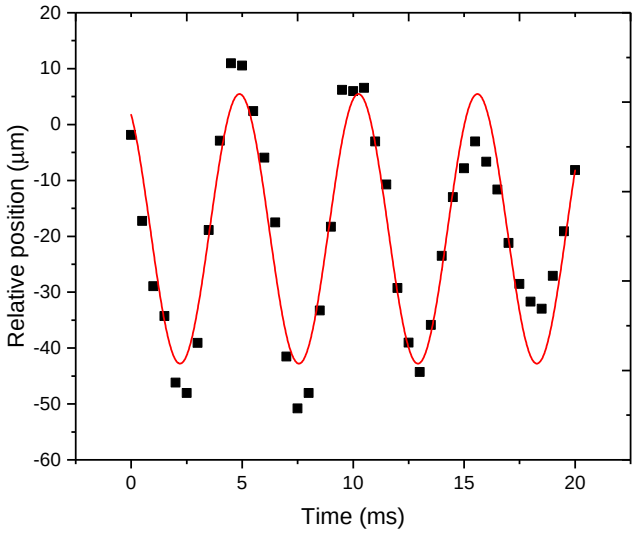

Fig. 4.5 A perturbation in the form of a short pulse of increased trap potential forces trapped atoms to oscillate along the radial axis. The y-axis is defined relative to the initial position of the trapped atoms.

4.4 Velocity Spread of Atoms in the Waveguide

Atoms released from the dipole beam are initially tightly confined along the length of WG1. Due to the uneven potential gradient, atoms closer to the focus of WG1 will accelerate faster than those more distant.

The atoms are in an attractive potential and expand along the waveguide whilst being attracted towards the region of higher trapping potential at the focus. For this reason as an atomic cloud propagates in WG1, it will visibly increase in size relative to the velocity distribution.

This results in a reduced density. Figure 4.6 clearly shows that there is only a small increase in cloud diameter by accelerating atoms more quickly. However, it is important to take into account the travel time of atoms between their release from the optical dipole trap and subsequent passing through the minimum beam waist of WG1. Due to the oscillatory nature of atoms in the waveguide, when no magnetic field is applied the time taken for atoms to reach the centre is roughly constant. There is no reliance on the separation between WG1 and the dipole trap. However, when an additional acceleration force is applied in the form of a magnetic field gradient, the travel time is significantly reduced. Whilst the cloud expansion is roughly equal in both cases, atoms accelerated using magnetic field gradients reach the centre faster. This results in a higher density of atoms with a velocity spread of $0.9\,\mathrm{mm\,s^{-1}}$, significantly below the recoil velocity.

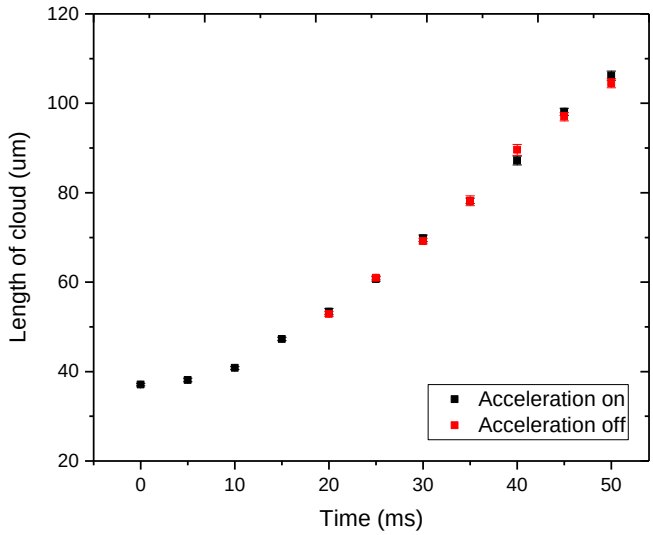

Fig. 4.6 A graph to show the minimal effect of applying a magnetic field gradient on the diameter of the atomic cloud. No measurements are taken at low times when the magnetic field coils are on as the atoms are still affected by a residual magnetic field gradient during imaging, reducing reliability of the true position of the atoms. This shows that applying a magnetic field gradient will not increase the velocity distribution of atoms in the waveguides.

The velocity distribution is calculated by measuring the diameter of the atom cloud along the axial direction of the waveguide as a function of time after it is released from the dipole trap. The FWHM of a Gaussian fit is used to calculate the diameter of the cloud. Figure 4.7 shows the linear relationship between cloud diameter and time. The fitted curve is only valid up to 55 ms at which point the cloud is split by the lattice, making the fit unreliable.

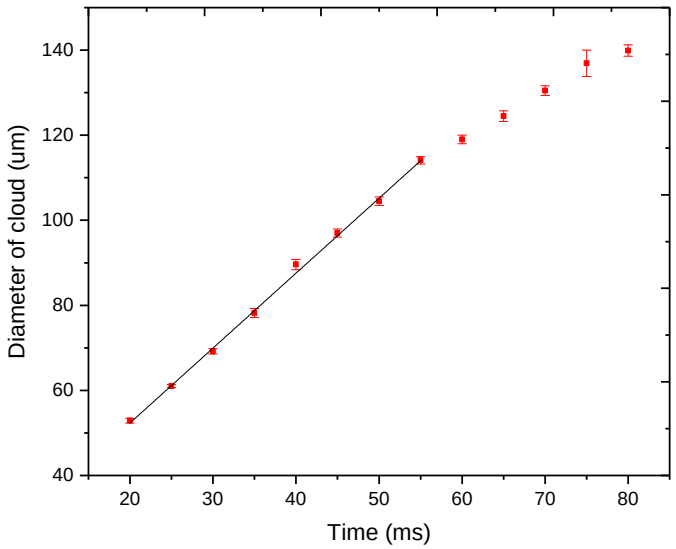

Fig. 4.7 The velocity distribution of a BEC released into WG1 can be calculated by measuring the cloud diameter as a function of time. Here atoms are accelerated over 30 ms using an applied magnetic field. The velocity distribution increases by $1.76 \pm 0.02\,\mathrm{mm\,s^{-1}}$.

Faster acceleration reduces the time atoms spend in the waveguides and therefore reduces the velocity distribution, improving the behaviour of the splitter. For this reason, the maximum permitted magnetic field gradient is used to accelerate atoms to the desired velocity in the minimum time possible. Due to rise and fall times of current through the magnetic coils, the minimum on-time is 5 ms and atoms can be accelerated up to $40\,\mathrm{mm\,s^{-1}}$ in this period. This is more than sufficient to achieve equal splitting in both waveguides.

4.5 Diffraction of Matter from a Standing Wave

When the atoms reach the intersection with the second waveguide, they experience a periodic lattice and are split between the two waveguides in an effect similar to Bragg diffraction. Bragg scattering was first observed as constructive interference arising from diffraction of x-rays from a zincblende cubical crystal by W. L. Bragg [122] in 1912. It led to a Nobel prize in 1915 and it was later shown that atoms can be deflected by light resonant with an atomic transition [123]. Following from this work, Bragg scattering of atoms using a standing light wave was first experimentally realised in 1988 [124] and opened the possibility of creating an atom interferometer using Bragg scattering. An incident atom cloud can be defined as a

de Broglie wave with wavelength $\lambda_{dB} = h/p$, and diffracts from an intensity grating with a defined lattice spacing within the standing wave. Atoms experience a momentum transfer from this interaction via absorption and stimulated emission in discrete units of $2\hbar k$. In Kapitza-Dirac scattering many momentum states are populated [125] represented as $\pm n\hbar k$ where n is an integer. However, Bragg scattering considers an ideal configuration where only a single momentum state is populated.

4.6 Periodic Potentials

Continuing to use the one dimensional model used in Chapter 2.1 for simplicity, the dynamics of a gas of non-interacting particles in a periodic potential is analysed. The 2 dimensional motion of atoms can be simplified to a 1D problem by introducing a system of coordinates along the direction of the first waveguide. The periodicity condition for a potential $U(x)$ will take the form

$$U(x) = U(x+d)\,, \tag{4.7}$$

where d is the lattice spacing and is analogous to ions in a perfect crystal aligned in a periodic array [126]. The time independent Schrödinger equation for the wavefunction $\psi(x)$ of a particle moving in the periodic potential is given as

$$\hat{H}\psi(x) = \left[-\frac{h^2}{2m}\frac{\delta^2}{\delta x^2} + U(x)\right]\psi(x) = E\psi(x)\,, \tag{4.8}$$

where m is the mass of the particle. The solutions of the Schrödinger equation are derived from the well known Bloch theorem [127] given as

$$\psi_{n,q}(x) = e^{iqx}u_{n,q}(x)\,, \tag{4.9}$$

where $u_{n,q}(x) = u_{n,q}(x+d)$. The band index n, and the quasimomentum q are quantum numbers known as Bloch states. The solution is composed of a plane wave, e^{iqx}, multiplied by a function with the same periodicity as the lattice, $u_{n,q}(x)$. There is a discrete invariance of the Hamiltonian when under a translation $x \Rightarrow x + nd$. As a result the quasimomentum q

is defined as modulo $2\pi/d = 2k_L$, and is the period of the reciprocal lattice. The periodicity of the lattice in real space also creates a periodic structure in momentum space, known as Brillouin zones. Any given quasimomentum q will have many different solutions with an energy spectrum $E_n(q)$. The band index n is named from the segmentation of the energy spectrum arising from the periodicity of the lattice into allowed and forbidden regions. These are known as energy bands and represent regions of high reflection for the non-interacting particles. The energy spectrum of a standard potential $U(x)$ is calculated from the limits of high and low potentials, starting from the extreme cases of tightly bound and free particles respectively. A pure sinusoidal potential represents the simplest form of a periodic lattice, given as

$$U(x) = \frac{U_0}{2}\left(1 - \cos 2kx\right), \tag{4.10}$$

and has a lattice spacing $d = \pi/k$. This can be substituted into Equation 4.8 to give

$$\left[-\frac{h^2}{2m}\frac{\delta^2}{\delta x^2} + \frac{U_0}{2}\left(1 - \cos 2kx\right)\right]\psi_{n,q}(x) = E_n(q)\,\psi_{n,q}(x). \tag{4.11}$$

This form of the Schrödinger equation is known as a Mathieu equation [128]. The solutions cannot be calculated analytically but are tabulated and good approximations to the positions of the band gaps can be made numerically. The Mathieu equations are used to calculate the band gap structure in the lattice and are a useful tool to engineer optimal splitting conditions by varying the amplitude of the periodic potential. Figure 4.8 shows an example of a band gap structure with $\varepsilon = 0.4$. The red dotted line indicates the bands witnessed by an atom travelling at $3v_R$. Two small bands are crossed, indicating reflection at their respective distances from the waveguide intersection centre.

4.7 Spatial Band Gaps Produced by Two Crossed Optical Waveguides

Optical waveguides are commonly used in interferometry experiments to transport pre-cooled atom samples for use in interferometry [129]. In this experiment they are composed of two tightly focused, red detuned lasers beams derived from the same laser used to generate the

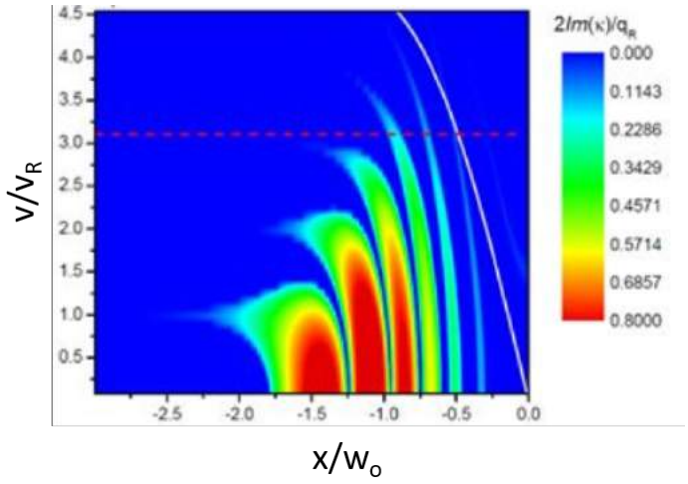

Fig. 4.8 A graph to show the size and position of band gaps, created from the interference of two waveguides. The position and amplitude of the bandgaps is dependent on the relative polarisation between the waveguides [72].

dipole beams. The waveguides are linearly polarised, and intersect at their respective focuses under an angle close to 90°.

Diffraction of matter-waves from one optically confined waveguide to another, labelled as WG1 and WG2 respectively, can be achieved using a standing wave lattice created from interference between the waveguides. Depending on the relative polarisation between the two, WG1 and WG2 can interfere when overlapped. The interference forms an optical lattice with a controllable height adjusted by the relative polarisation of the two waveguides. This creates an optical lattice with defined band gap structures able to reflect a fraction of incident atoms from one waveguide to another. The simple design allows any angle between the two waveguides to be considered as the optical lattice will always form in alignment with the waveguides. As the waveguides are focused with a non-uniform beam diameter, the lattice will also be inhomogeneous, with a Gaussian envelope and the greatest lattice amplitude existing at the focus of both waveguides. In the simplified 1D model, the Gaussian nature of the potential means atoms inside the crossing region experience an additional acceleration.

The potential arising from the two intersecting waveguides at an angle θ can be expressed as

$$U(x,y) = -\frac{1}{2\varepsilon_0 c}\alpha\,|E_0|^2\, I(x,y)\,, \tag{4.12}$$

where α is the atomic polarisability and E_0 is the amplitude of the light field. Assuming the lattice spacing is significantly smaller than the minimum waist of the waveguides, the normalised intensity $I(x,y)$ is

$$I(x,y) = 2e^{-\frac{1}{{w_0}^2}\left[(y\cos\theta - x\sin\theta)^2 + y^2\right]} \Bigg\{ \cosh\left[\frac{1}{{w_0}^2}\left[(y\cos\theta - x\sin\theta)^2 - y^2\right]\right] + \varepsilon\cos\left[k_R(x(\cos\theta - 1) + y\sin\theta)\right] \Bigg\}, \tag{4.13}$$

where $k_R = \frac{2\pi}{\lambda}$ is the light wave number and w_0 is the minimum beam waist. The x-axis is aligned with direction of propagation of WG1. To further simplify the notation, the coordinates are rotated by $\theta/2$ to work in the reference frame of the lattice. The potential here is given as

$$U(x',y') = -U_0(x',y')\left[A(x',y') + \varepsilon\cos(q_R(\theta)y')\right], \tag{4.14}$$

where $0 \leq \varepsilon \leq 1$ is the interference amplitude between the waveguides and is dependent on the relative polarisation between the two and defines the lattice amplitude. The effective wavevector $q_R(\theta) = 2\sin(\frac{\theta}{2})k_R = \frac{2\pi}{d}$ where d is the lattice spacing. Here $U(x',y')$ is the sum of two potentials; a trapping potential $U(x',y') = -U_0(x',y')\left[A(x',y')\right]$ and a periodic lattice with a gaussian envelope $U_{lattice} = \varepsilon U_0(x',y')$ and can be written as

$$U_0(x',y') = -2U_t e^{-\frac{1}{{w_0}^2}\left[(1-\cos\theta)x'^2 + (1+\cos\theta)y'^2\right]}. \tag{4.15}$$

U_t is the trap depth created by a single waveguide. As $w_0 \gg 2\pi/k_R$ and assuming $U_0(x',y')$ is slowly varying compared to $\cos(q_R(\theta)y')$, the band gap structure produced by the lattice can be described using methods found in [130]. Equation 4.15 gives the potential of the quasi-periodic lattice. The stationary Schröedinger equation is described as a Mathieu equation meaning the position of the band gaps can be determined numerically by calculating the imaginary component of the Mathieu characteristic exponents κ. Solutions of the Mathieu equation are in the form $e^{i\kappa x}f(x)$. If κ is an imaginary value, it indicates the wavefunction is evanescent. Particles with energy lying inside a band gap will experience suppression and be reflected. Due to inhomogeneities in lattice amplitude the band gap structure creates

reflective barriers known as spatial gaps. The exact number of band gaps is determined by the depth of the trap.

The lattice design lends itself for use in a Michelson or Mach-Zehnder interferometer where a deflection of atoms into separate waveguides can be furthered to create an all-optical atomic circuit with a relatively large enclosed area for use in high sensitivity measurements.

4.8 Beamsplitter Design

A novel approach to splitting a cloud of atoms is used with the aim of continually and coherently splitting an atomic beam. The beamsplitter is composed of two separate optical waveguides derived from the same laser and with identical characteristics such as frequency, power and intensity. They overlap with an angle θ close to 90° and both waveguides intersect at their minimum waist. Both waveguides have the same optical properties including wavelength, minimum beam waist and power.

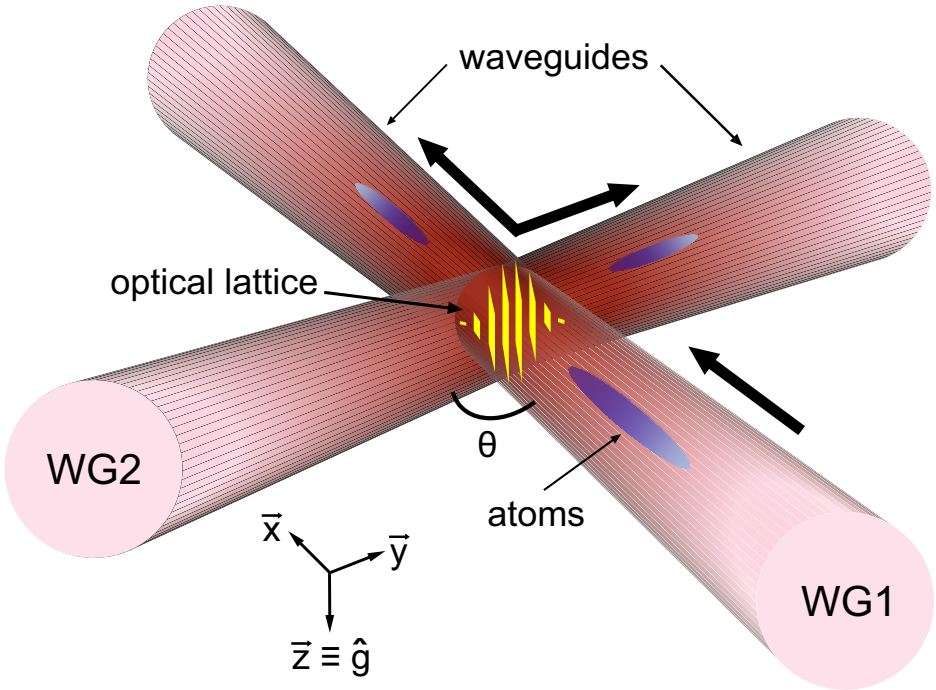

Fig. 4.9 Diagram to show layout of the two optical waveguides. A periodic optical lattice forms at their intersection with a Gaussian envelope.

Figure 4.9 demonstrates how the waveguides are aligned. Both waveguides are adjusted to be horizontal to a good degree of accuracy through measuring their axial frequency described in

Chapter 4.3. If the waveguide is not horizontal, atoms will not oscillate around the focus. Significant deviations from horizontal result in a large enough gravitational potential for atoms to exit the waveguide. The angle of the waveguide relative to horizontal is adjusted using the 5-axis kinematic mount shown in Figure 5.20. A high thread count screw is used to adjust the angle of the beam and can be approximated to be horizontal by measuring the beam height at near and far distances. The waveguide must be horizontal and overlap with the dipole beams. The height of the beam can be crudely adjusted by adding spacers in increments of 0.5 mm. Finer adjustments are provided by a vertical translation stage which moves the fibre coupler and collimating lens relative to the final focusing lens. A more accurate test of how horizontal the waveguides are can be made by measuring the radial frequency, an example is shown in Figure 4.4. Through careful measurement of the centre of an oscillation, defined as the point where atoms have maximum velocity, both waveguides can be made horizontal to a good degree of accuracy over a relatively large distance.

The current experimental setup images the atoms along a single vertical axis, meaning there is no sensitivity to the height of the beams relative to each other. Due to the waveguides small beam waists, it is difficult to overlap them with the dipole beams. A systematic approach is taken to aligning the beams. Firstly, significantly higher power is sent through the waveguide outcouplers to create a deeper potential that is capable of trapping atoms without the dipole beams. The waveguide is aligned along the x-axis and y-axis by viewing the position of trapped atoms from the imaging system. If the two beams are not aligned, the two beams act as single arm dipole potentials, and create two separate elongated traps. Then the waveguide is adjusted until it intersects with the dipole potential. Using the imaging system it is simple to observe when this happens, as the two elongated traps will combine to form a crossed trap, more reminiscent of the dipole trap image shown in Figure 3.19. The second waveguide is then aligned in a similar manner. After several iterations of both techniques, the waveguides can be overlapped with each other, and to the dipole trap whilst being horizontal.

An example of the shape of the potential at different interference intensities is shown in Figure 4.10, derived from Equation 4.13 and plotted along a single axis.

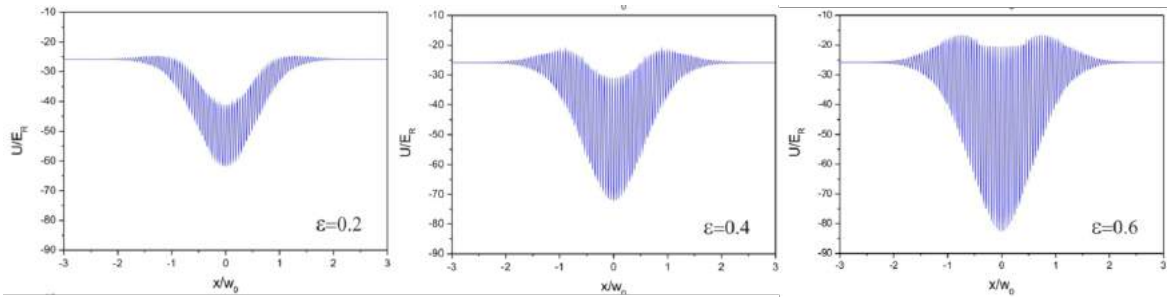

Fig. 4.10 A calculation to show how the shape and depth of the potential changes when varying the interference between the two overlapping beams.

4.9 Passage Through the Beamsplitter

The photon recoil velocity, v_R, is defined as the change in velocity of an ^{87}Rb atom when absorbing or emitting a resonant photon [76]. However, in an optical lattice [131], the recoil velocity of atoms reflecting from a Bragg grating is calculated as

$$v_R = \frac{\hbar k}{m}, \tag{4.16}$$

where $k = \pi/d$ is the wavevector and d is given as

$$d = \frac{\lambda}{2\sin(\theta/2)}. \tag{4.17}$$

The direction of the lattice always propagates with an angle $\theta/2$ between two waveguides crossing with an angle θ. Only the velocity component of incident atoms perpendicular to the lattice can be considered. For this reason, the sine term cancels and the recoil velocity is not dependent on the angle θ between the two waveguides. The recoil velocity is therefore calculated as $v_R = 4.3$ mm/s and the velocity distribution of atoms in the waveguide from Chapter 4.4 is $0.2\,v_R$.

Without use of magnetic fields to further accelerate atoms, the maximum velocity attainable in a waveguide with trapping potential $U = 25\,E_R$ and waist $w_0 = 25\,\mu$m is roughly $20\,\mathrm{mm\,s^{-1}}$ or $4.7\,v_R$, where $v_R = 4.3\,\mathrm{mm\,s^{-1}}$ is the recoil velocity. This corresponds to a separation distance of 1 mm, comparable to the Rayleigh length of WG1.

Information about the lattice can be found by adjusting the lattice strength and atom velocity and observing the position of atoms as they exit the lattice. Atoms propagating in the waveguide and split by the lattice can exit from several points in the lattice. Using the coordinate system in Figure 4.9 the majority of atoms exit the lattice in the positive x and y axes. However, a small percentage will remain trapped by the waveguide potential or fall out of the trap altogether and be lost. Due to the inhomogeneous nature of the lattice, losses will be dependent on lattice strength and initial atom velocity. A graph comparing the number of reflected and transmitted atoms as a function of lattice strength ε is shown in Figure 4.11. Data is taken by allowing atoms in a BEC to propagate towards the crossing region with WG2 over a time period of 30 ms. Once enough time has passed to allow all atoms to propagate through the crossing region the intensity in the waveguides is reduced to zero and atoms are allowed to fall and expand for 2 ms during time of flight. Atoms are then imaged using techniques mentioned in Chapter 3.8. Analysis software calculates the number of atoms reflected, transmitted or trapped in the crossing region.

A total of four measurements with velocities ranging from $0.8\,v_R$ to $4.7\,v_R$ are shown. From Figure 4.11a, it becomes apparent that for low velocities $v_R < 1$ very few atoms are reflected by the lattice regardless of lattice strength. This is expected behaviour as the atoms have insufficient energy to enter the lattice and are instead trapped before entering. Increasing the lattice height further will only trap more atoms outside the crossing region. For atoms with velocity $v_R < v \leq 3\,v_R$ atoms are able to enter the lattice and small fractions are reflected as lattice height increases. However, continually increasing the lattice height will start to trap atoms outside the crossing region and the number of reflected atoms decreases. Finally, the lattice is capable of reflecting up to 85% of atoms with velocity $v > 3\,v_R$ into WG2. At the highest tested velocities of $4.7\ v_R$ the maximum lattice height is incapable of trapping all atoms outside the waveguide.

Similarly, Figure 4.11b shows the fraction of atoms transmitted in WG1. As mentioned previously, a majority low velocity atoms $v < v_R$ are trapped outside even with no lattice present. However, for atom velocities $v > v_R$ virtually all atoms are transmitted through the crossing region when no lattice is present. Additionally, all velocities tested reduce to a negligible transmitted fraction given a high enough lattice amplitude, with higher velocities requiring higher lattice heights as expected. The transmitted fraction of atoms is therefore completely controllable with a majority of initial atom velocities.

Data from the number of trapped atoms shown in Figure 4.11c illustrates how increasing the lattice strength affects the fraction of atoms unable to enter the crossing region and are

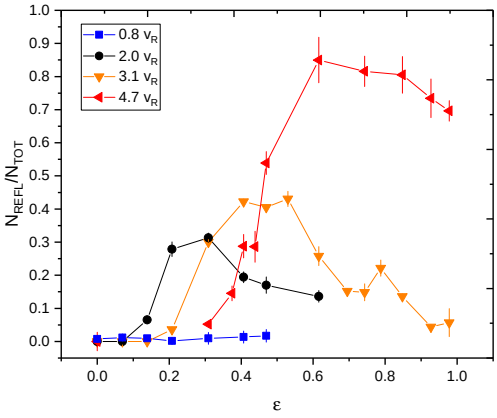

(a) Reflected fraction.

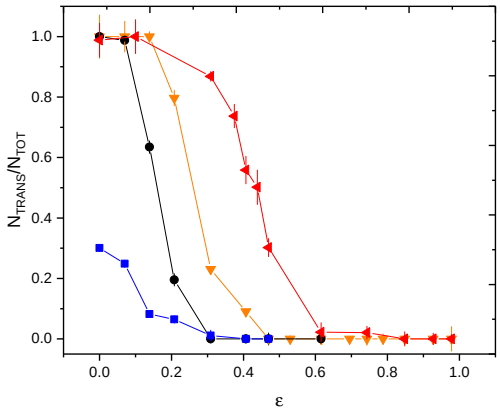

(b) Transmitted fraction.

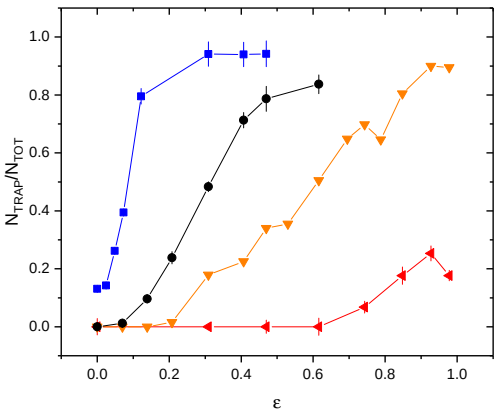

(c) Trapped fraction.

Fig. 4.11 Fraction of atoms that are reflected into WG2 (a), transmitted in WG1 (b) or trapped at the entrance to the crossing region (c). All measurements were taken without additional magnetic field acceleration. The lines act as a guide [72].

therefore treated as losses. Only the highest velocity atoms are able to enter the crossing region with losses below 20% at maximum lattice height. For atoms with low velocities the losses become predominant, with $> 90\%$ of atoms trapped before entering. Low numbers in the trap result in difficulty imaging and a low signal-to-noise ratio.

4.10 Additional Acceleration using Magnetic Fields

Allowing atoms to naturally accelerate in WG1 provides very little control over their final maximum velocity as they pass through the focus of WG1. The only experimental control linked to this velocity is the initial distance δ between the BEC and WG1 focus. Increasing δ allows more time for atoms to accelerate, at the cost of a weaker initial trap depth. Furthermore, atoms will be limited by a maximum velocity as increasing δ will eventually lead to atoms falling out of WG1. Atoms are constantly accelerating in the potential, meaning their velocity as they pass through the focus of WG1 will be non-uniform. This also becomes an issue for the repeatability of the experiment. If a different atom velocity is required, the waveguide must be physically realigned to move the BEC to or from the focus. Aside from being a time consuming process it becomes impossible to revisit old parameters reliably.

One simple method to overcome these limitations is to use a magnetic field aligned along the axial direction of WG1 to accelerate atoms. In the experiment the coils used in the 3D MOT to produce an anti-Helmholtz field are offset from WG1 by an angle of 10°. During a normal experimental cycle they are switched off once a full size MOT is formed, meaning they can be reused to accelerate atoms in WG1 after formation of the BEC. The small offset results in minimal excitations, whilst accelerating atoms to much greater velocities. Additionally, if the acceleration is great enough any potential created by the waveguide becomes negligible, resulting in almost zero acceleration once magnetic coils are switched off. Much larger velocities are obtainable, with a maximum of $23\,v_R$ or $99\,\mathrm{mm\,s^{-1}}$, significantly larger than the original maximum of $4.7\,v_R$. However, for velocities $v > 15\,v_R$ a maximum amplitude lattice is unable to reflect any atoms due to the increased kinetic energy of the atoms. An additional advantage of using magnetic acceleration is a calibration can easily be made between magnetic field strength and final atom velocity allowing many velocities to be tested accurately. Additionally, as no realignment of optics is required δ can be smaller, reducing effects from atoms falling out of the lattice due to the decreased potential depth far from the

waveguide focus. An example calibration is shown in Figure 4.12, displaying the velocity of atoms in the waveguide after acceleration as a function of the current supplied to the coils. The linear relationship can be used to calibrate and allow rapid testing of different velocities.

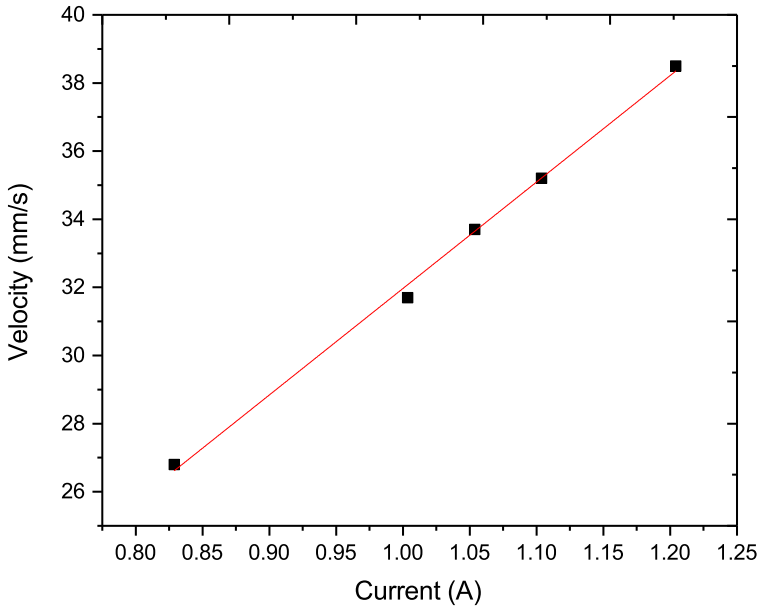

Fig. 4.12 A graph showing a calibration between 3D MOT coil current and velocity of atoms after acceleration. The separation between BEC and WG1's focus is kept constant, as is the total acceleration time. The red line represents a calibration used to quickly estimate the atom cloud velocity and is represented by a straight line equation allowing quick testing of the high velocity regime.

Figure 4.13 depicts measurements taken using additional magnetic acceleration to reach higher velocities. All tested velocities were taken with the same separation between the initial position of the BEC and the focus of WG1. A varying magnetic field dictated the velocity of atoms in the waveguide. A magnetic field gradient is applied from the point that atoms are released in WG1 for a constant duration of 30 ms. Care was taken to switch off the magnetic coils before atoms entered the lattice to ensure no additional forces are imparted on the atoms. Eddy currents remaining within the coils immediately after switching off are also considered, leading to the coils switching off significantly before atoms enter the lattice. Different velocities are therefore achieved by altering the current sent to the magnetic coils. High velocity data shows a broad continuation from trends observed in

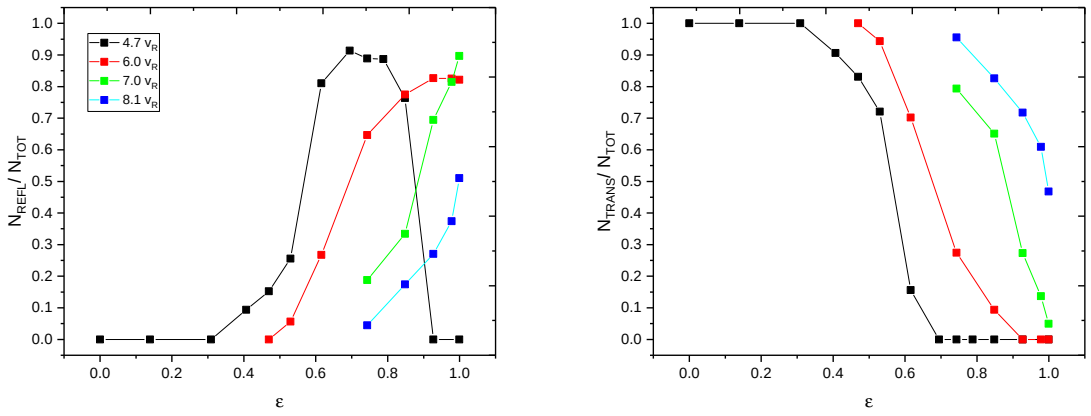

(a) Reflected fraction.

(b) Transmitted fraction.

Fig. 4.13 High velocity dynamics of atoms entering the lattice of varying strength. Figure 4.13a shows the fraction of atoms reflected into WG2, Figure 4.13b shows the transmitted fraction of atoms. In the high velocity regime $v > 4.0\,v_R$ no atoms remain trapped in the lattice.

Figure 4.11. At $4.7\,v_R$ increasing lattice strength eventually prevents atoms from entering the crossing region, thus reducing the fraction of atoms reflected into WG2. However, for higher velocities $5\,v_R < v < 7\,v_R$ the maximum lattice height is insufficient to trap any atoms in the crossing region. At very high velocities, $v > 8\,v_R$, atoms have sufficient energy to be transmitted through the crossing region at the maximum lattice amplitude. The trend continues and sufficiently high velocities are capable of traversing the crossing region with a negligible reflected fraction. However, the higher velocity regime is still preferable due to a significantly lower fraction of atoms trapped in the lattice. This increases atom numbers and therefore signal-to-noise ratio in the waveguides after splitting. In addition, the increased density of atoms reduces the wavepacket size after splitting.

Despite the higher velocities achievable using magnetic coils, high velocity distribution of atoms in the waveguide prevents the splitter from working as intended. Figure 4.14 shows the splitting effect when atoms are accelerated slowly to $26\,\mathrm{mm\,s^{-1}}$. The slow acceleration increases the velocity distribution of the atoms, meaning higher velocity atoms reach the splitter first and are more likely to be transmitted using data from Figure 4.13b. Slower atoms are similarly more likely to be reflected and this is observed in Figure 4.14 as the reflected fraction of atoms are closer to the lattice, indicating they are reflected later. As a direct result the lattice is acting as a velocity selector with the two separated clouds travelling at different average velocities, making it more difficult to recombine the two clouds later.

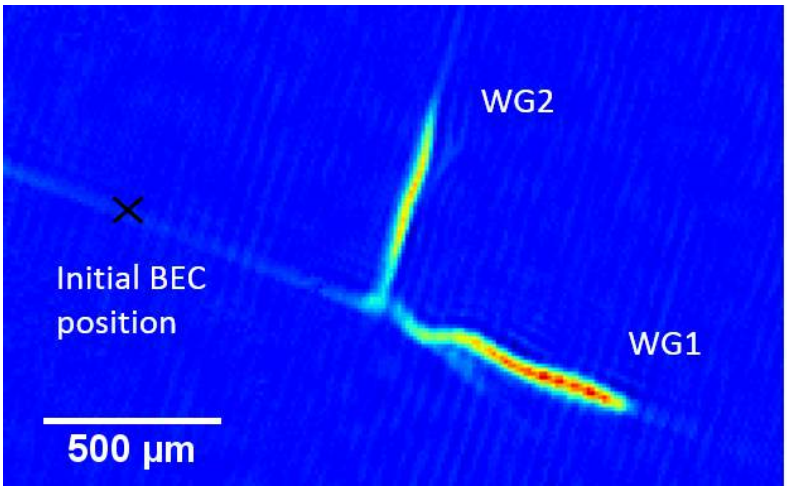

Fig. 4.14 Atoms in a BEC are accelerated to $26\,\mathrm{mm\,s^{-1}}$ in 30 ms using magnetic coils. The relatively slow acceleration time increases the velocity distribution of atoms in the waveguide. As a result faster atoms are selectively transmitted whereas slower atoms are more likely to be reflected. This image is taken with 0.3 ms expansion time.

4.11 Atom Dynamics in the Lattice

Further information regarding atom behaviour in the lattice can be obtained through a sudden reduction in lattice intensity whilst the atomic cloud is passing through. In a regime where atoms are equally split between waveguides, switching off WG1 and WG2 simultaneously will cause atoms to fall and expand under gravity. If the waveguides are switched off whilst atoms are present in the lattice, information regarding the atomic momentum distribution inside the lattice will become clear. The momentum spread is mostly determined by the interaction energy between the atoms. Figure 4.15 shows atoms entering the lattice with an initial velocity $v_i = 9.0 \pm 0.2 v_R$ and lattice strength $\varepsilon = 0.9$, corresponding to roughly 40% reflection into WG2. Light from WG1 and WG2 is abruptly switched off using an AOM and atoms fall and expand due to gravity. Interesting atom behaviour is revealed in the lattice if it is removed.

If the confining potential creating the lattice is suddenly removed, several clearly resolved quasimomentum peaks become visible. Increasing the time of flight will separate the peaks further to the point where they are independently resolved and observable in images.

The peaks are clearly resolved and show how atoms experience a discrete transfer of momentum from each lattice site. It also demonstrates the multi-photon processes that atoms experience in the lattice before exiting roughly orthogonal to their initial direction. The

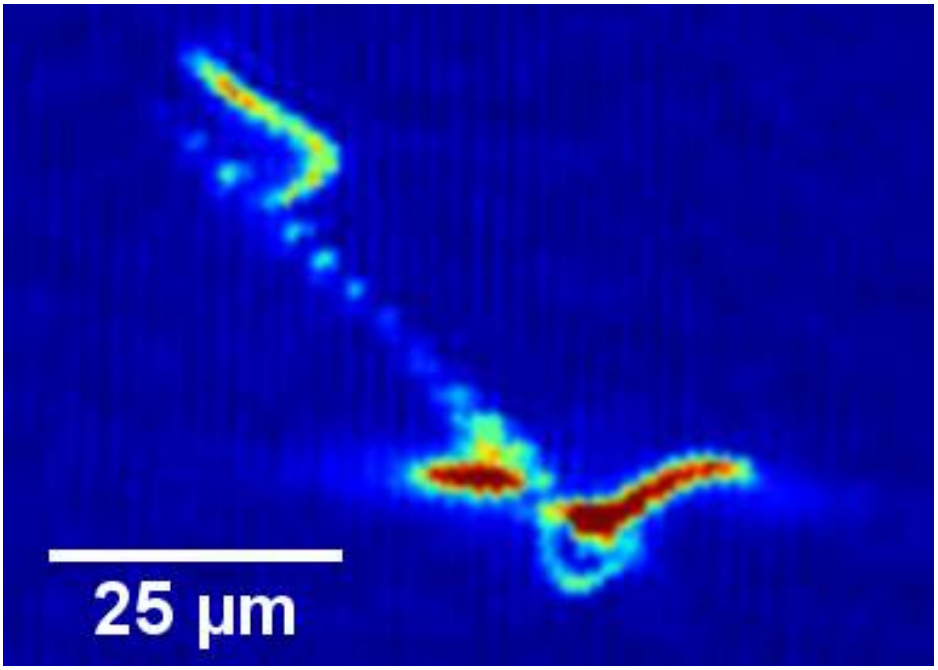

Fig. 4.15 Atoms entering the lattice from WG1 along the horizontal direction are reflected into WG2 along the vertical axis. WG1 and WG2 are switched off as atoms are present in the crossing region and atoms are allowed to expand for 5 ms. Atoms that have already exited the lattice can be seen as two separate clouds, whilst atoms still in the crossing region form several discrete points described as quasi-momentum peaks.

interaction time of atoms incident on the optical lattice is typically large, $t\frac{E_R}{\hbar} > 1$, and the reflection of atoms occurs where the lattice is strong, $U_{lat} \gg E_R$. The initial velocity of the cloud prevents any atoms being trapped in the lattice centre. This leads to the label quasimomentum peak using the notation in [132] as they are only visible when the confining potential is rapidly removed whilst atoms are in the lattice. An atom in the light field will experience a sinusoidal potential as a function of position given by

$$V(x) = V_{max}\cos^2(kx)\,, \tag{4.18}$$

where the wave vector $k = 2\pi/\lambda$ and the peak-to-peak height $V_{max} = \hbar{\Omega_{rabi}}^2/\Delta$. Atom detuning $\Delta = \omega_{light} - \omega_{atom}$ and the on-resonance Rabi frequency $\Omega_{rabi} = dE/\hbar$ is proportional to the atomic dipole moment d and the electric field E. V_{max} is proportional to the light intensity I. The period of the lattice is calculated as

$$\frac{\lambda}{2\sin(\theta/2)}\,. \tag{4.19}$$

The potential height V_{max} and atom-light interaction time τ_{int} can be normalised through comparison with the recoil frequency $\omega_{rec} = \hbar k^2/(2m)$ using

$$q = \frac{V_{max}}{4\hbar\omega_{rec}}\,, \tag{4.20}$$

and

$$\tau_{int} = \omega_{rec} t_{int}\,. \tag{4.21}$$

By considering atoms diffracting in a periodic standing light field, three diffraction regimes are found to exist dependent on the potential height of the lattice and the interaction time of atoms in the light field. Figure 4.16 shows the different regimes as a function of interaction time and potential height.

Firstly the Raman-Nath regime is valid for short interaction times fulfilling

$$\tau_{int} < \frac{1}{2\sqrt{2q}}\,. \tag{4.22}$$

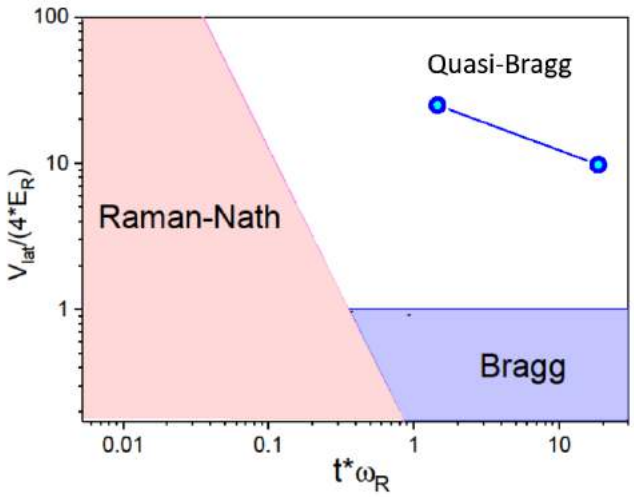

Fig. 4.16 Three diffraction regimes exist for atoms incident on a standing light wave, Raman-Nath, Bragg and quasi-Bragg. In this experiment the beam splitter exists between the Bragg and quasi-Bragg regimes for velocities tested $3\,v_R \leq v \leq 9\,v_R$. The smooth Gaussian envelope of the lattice leads to the diffraction pattern produced by a single spatial gap and is similar to that of a Bragg regime. For this reason the regime is quasi-Bragg.

Interaction time is short compared to the oscillation period of the lattice. The Bragg regime is characterised by small potentials satisfying $q < 1$ and longer interaction times. Atoms can only be deflected if the incident angle fulfils the Bragg condition [133].

The final regime is characterised by long interaction times and high potentials and is named quasi-Bragg as atoms tend to channel along the minima of the standing waves. Atoms in this experiment are in the quasi-Bragg regime as the smooth Gaussian envelope of the lattice creates a diffraction pattern very similar to that of a Bragg regime [134, 135].

Initially a few quasi-momentum peaks are populated around the observed exits for the atoms. The discrete peaks can be described in a coordinate system whereby the first quasi-momentum peak visible in the transmitted fraction can be described as $q_1 = (q,0)$, where q is defined in Equation 4.20 as the momentum of the atoms before being reflected by the lattice. Similarly, the first reflected quasi-momentum peak will occupy $q_2 = (0,q)$. Adjacent peaks are separated by

$$\Delta q = \pm q_R(\theta)\cos\left(\frac{\pi-\theta}{2}\right), q_R(\theta)\sin\left(\frac{\pi-\theta}{2}\right). \tag{4.23}$$

As time increases further, more quasi-momentum peaks become occupied until all spaces are filled. The initial velocity of the atoms affects the number of quasi-momentum states that atoms exit. For velocity $v < 8\,v_R$ atoms exit the splitter in two or more states. However, for $v > 8\,v_R$ a single momentum state is occupied despite complex dynamics in the crossing region. As a consequence, it shows that splitting is caused by diffraction from the lattice in a coherent process, akin to Bragg diffraction.

4.12 Conclusions

The introduction of crossed optical waveguides has provided a novel means of transporting and splitting atoms condensed into a BEC. The optical waveguides are derived from the same laser used to create the dipole beams but are shifted in frequency using an AOM to prevent any cross interference. One of the waveguides is used as a dimple beam to aid in evaporating atoms in the dipole trap, helping to achieve a BEC with up to 10^5 atoms. Once released from the dipole trap into WG1, atoms begin to oscillate around the minimum trap potential. This yields information regarding the angle of the waveguide relative to gravity and the purity of the sample by a measured damping of the oscillation amplitude.

The reflected fraction of atoms is highly dependent on the lattice amplitude and the initial velocity of the atoms. The velocity was increased varied by changing the distance between the BEC and the focus of WG1. This allowed more time for the cloud to accelerate, reaching higher velocities as a result. However, the maximum velocity achieved of $4.7\,v_R$ was difficult to maintain due to the large separation between WG1 and the BEC close to a Rayleigh length. The application of a magnetic field gradient can rapidly accelerate atoms to velocities up to $100\,v_R$, well in excess of requirements. Tests at higher velocities show that fewer atoms are lost from the lattice.

Chapter 5

Michelson Interferometer

A cold, coherent cloud of ^{87}Rb atoms can be accelerated in optical waveguides and split in a controlled manner using an interference pattern arising from two overlapping laser beams. The amplitude of the lattice dictates the percentage of atoms reflected or transmitted into different waveguides with high precision and repeatability. However, it is unclear once atoms have exited the splitter if they are still coherent. To test coherence, the two separated clouds are recombined and the resulting interference pattern is analysed. The simplest method is to invert the velocity of atoms by reflecting them back along the same waveguide and recombine using the initial splitter in a Michelson interferometer configuration.

5.1 Inverting the Motion of Atoms in the Waveguides

Chapter 4.10 details how the coils used to create the 3D MOT can also be used to accelerate atoms in the waveguide. The anti-Helmholtz configuration of the coils creates zero magnetic field at the centre of the MOT. However, the waveguides are slightly offset from the centre, allowing a small applied magnetic field gradient to accelerate the atom cloud. Inverting the motion of atoms in WG1 is more difficult than simply swapping the polarity of the coils, as the magnetic field gradient still propagates in the same direction. However, a single coil from the anti-Helmholtz pair used by itself creates a region of high magnetic potential, which repels atoms. The circuit diagram used to swap between the anti-Helmholtz and single coil configurations is shown in Figure 5.1.

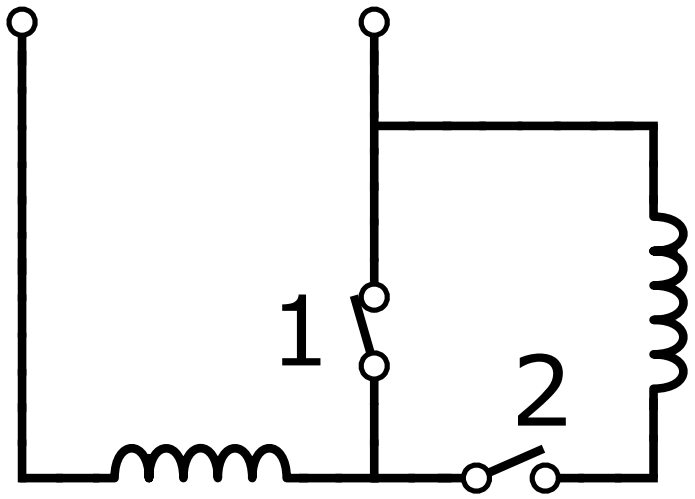

Fig. 5.1 Two switches, labelled 1 and 2, are inserted between the two magnetic coils used to form the 3D MOT and are controlled using Cicero. In this diagram a single magnetic coil is used by setting switch 1 to closed and switch 2 to open.

The switches used are solid state relays, chosen for their fast switching characteristics. Typically, the single coil is only required for up to 20 ms and must be completely off, including sufficient attenuation of eddy currents, by the time atoms enter the lattice to ensure all atoms enter with equal velocity. An additional complication arises as the magnetic field gradient generated by a single coil is weaker than using two. This can be compensated by increasing the current supplied to the single coil and required an additional power supply to be installed in parallel to generate a maximum current of 10 A. Higher currents were not considered due to excessive heating of the coil potentially melting the wound wire. Additionally, decelerating the atoms requires a greater velocity change as they are already in motion in the opposite direction. The maximum current deliverable is a limiting factor and places constraints on the minimum time atoms are separated. Faster recombination is possible when working with lower initial velocities but optimal splitting is only observed at higher velocities, see Chapter 4.10. The single coil is only useful in decelerating atoms that are transmitted in the lattice and remain in WG1. Atoms reflected into WG2 are travelling perpendicular to the direction of the magnetic field gradient. However, the potential depth of the waveguide is greater and so atoms remain in the waveguide with only minimal excitations. An additional coil is required to create a gradient along the axial direction of WG2 to decelerate atoms. The coil is placed around the glass cell as shown in Figure 5.2 and is placed as close as possible to the atoms but is limited by the position of the 3D MOT beam pairs and the 3D MOT coil housing. As the coil is situated further from the atoms than the

3D MOT coils, it will require a greater current to generate a similar magnetic field gradient at the position of the atoms. The magnetic field gradient can be approximated as

$$\frac{\mathrm{d}B}{\mathrm{d}r} = \frac{\mu_0 IA}{2\pi r^3}, \tag{5.1}$$

where IA is the magnetic moment of the coil and r is the distance from the coil to the atoms. The $1/r^3$ dependence drastically reduces the magnetic field as distance increases. To help compensate, a larger coil is used with a greater number of turns and thicker wire to enable higher currents.

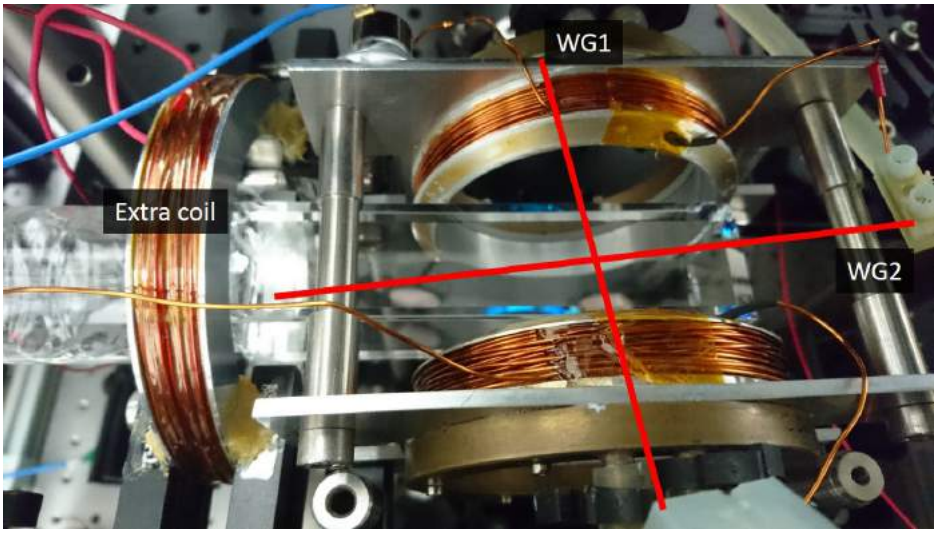

Fig. 5.2 An image to show the position of the additional coil used to decelerate atoms in WG2 relative to the parallel pair of coils used for the 3D MOT. The housing used to secure these coils limits how near the extra coil can be placed.

The 3D MOT coil pair is used to accelerate atoms towards the lattice. Faster acceleration results in a smaller velocity distribution, meaning the coils are off long before atoms enter the lattice. Therefore, a small window exists where no magnetic field gradient is applied. This small downtime allows any eddy currents in the coils to dissipate and also allows time for the switches to activate and effectively remove the second coil. The magnetic field gradient is reapplied immediately after all atoms have exited the lattice to minimise the time taken to invert the velocity of the cloud. The additional coil is switched on simultaneously and careful balancing of currents sent to both coils is required to return atoms in both waveguides concurrently.

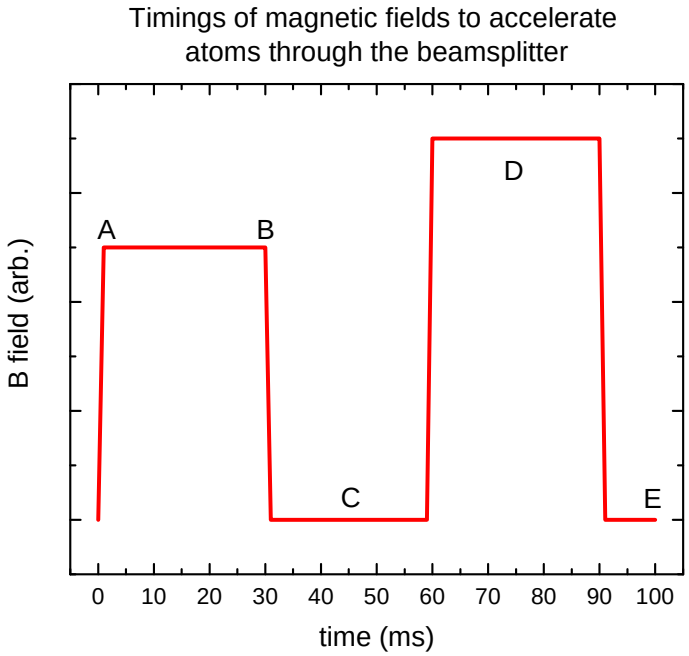

Fig. 5.3 A graph to show the timings of the magnetic field gradient pulses used to accelerate atoms towards the beamsplitter.

Figure 5.3 shows the timings of the applied magnetic field pulses used to accelerate and decelerate the atoms through the beamsplitter. After the formation of the BEC, a magnetic field gradient is applied to accelerate it towards the crossing region, shown as A in the figure. The atoms are accelerated for a maximum of 30 ms, where the magnetic field is switched off at point B. The magnetic field remains off at C for an additional 30 ms to allow atoms to split into the separate waveguides with a constant velocity. Whilst the B field is off, the switches in Figure 5.1 are used to invert the direction of the magnetic field gradient. Once all atoms have exited the crossing region, the magnetic fields are reapplied in the opposite direction to the motion of atoms at D, causing them to decelerate back towards the splitter. A stronger magnetic field is required due to the increased distance between the decelerating coil and the atoms. Again the magnetic field is switched off when atoms enter the crossing region at E. Beyond this point more time is given to allow the atoms to propagate through the splitter before imaging.

As WG1 is not well aligned to the axis of the magnetic field from the coil, but is instead offset by roughly 10°, it will also impart a force along the radial axis of the waveguide. Several iterations of different magnetic field strengths in each coil were tested to find optimal conditions that resulted from atoms in both arms returning at the same time and with equal

velocity matching the initial velocity atoms entered the lattice. Figure 5.4 shows a montage of images appreciating in time left to right, top to bottom in steps of 5 ms of a BEC accelerated to $32\,\mathrm{mm\,s^{-1}}$ towards the lattice and splitting into two equal clouds. Accelerating atoms takes 5 ms and the magnetic field is otherwise switched off. Atoms have all passed through the lattice after $t = 40$ ms, at which point the deceleration coils are activated. As previously mentioned decelerating is slower, taking 30 ms total for the atom clouds to completely invert their velocity.

A gradual reduction in atom number is evident throughout the time atoms exist in the lattice. A large cause of losses derives from the finite accuracy of alignment of the coils with respect to the waveguide which leads to the excitation of transverse modes. Despite the longer time required to decelerate the atoms, the distance travelled by atoms in the two arms is roughly equal at 500 μm. This is close to the Rayleigh length of the waveguides and provides further insight into why atom losses occur. The beam waist at a distance of a Rayleigh length from the focus increases by a factor of $\sqrt{2}$ and the potential depth decreases by almost half. Atoms are only slightly held in the waveguide against gravity and noise in the beam position and intensity results in large losses. These effects can be mitigated by using a stronger magnetic field on-axis to the waveguides to reduce the distance atoms travel in the waveguide. This approach is infeasible due to constraints on the magnetic coils, but an alternative method is to increase the confining potential in the waveguides by increasing the intensity, either by reducing the beam waist or increasing the power in the waveguides.

It should be noted that interference between the two recombining atom clouds will not be visible. This is because for atoms travelling with a velocity of $28.8\,\mathrm{mm\,s^{-1}}$, the corresponding de Broglie wavelength of the matter wave is $\lambda_{dB} = 160$ nm. As a result, the fringes of the Michelson interferometer have a spacing of $\lambda_{dB}/2 = 80$ nm. Correspondingly, half a fringe is 40 nm and any observation of interference will therefore only be visible when varying the length of one Michelson interferometer arm relative to the other by 10 nm or better. For arms of length roughly 0.5 mm, this corresponds to a level of control in the magnetic mirror amplitude of 10^{-5} or better, which is unrealistic using current methods.

5.2 Atom Behaviour after the Lattice

The dynamics of atoms in the lattice is described in Chapter 4.11, where atoms are shown to exit in one or more momentum states depending on their initial velocity. Atoms exiting the

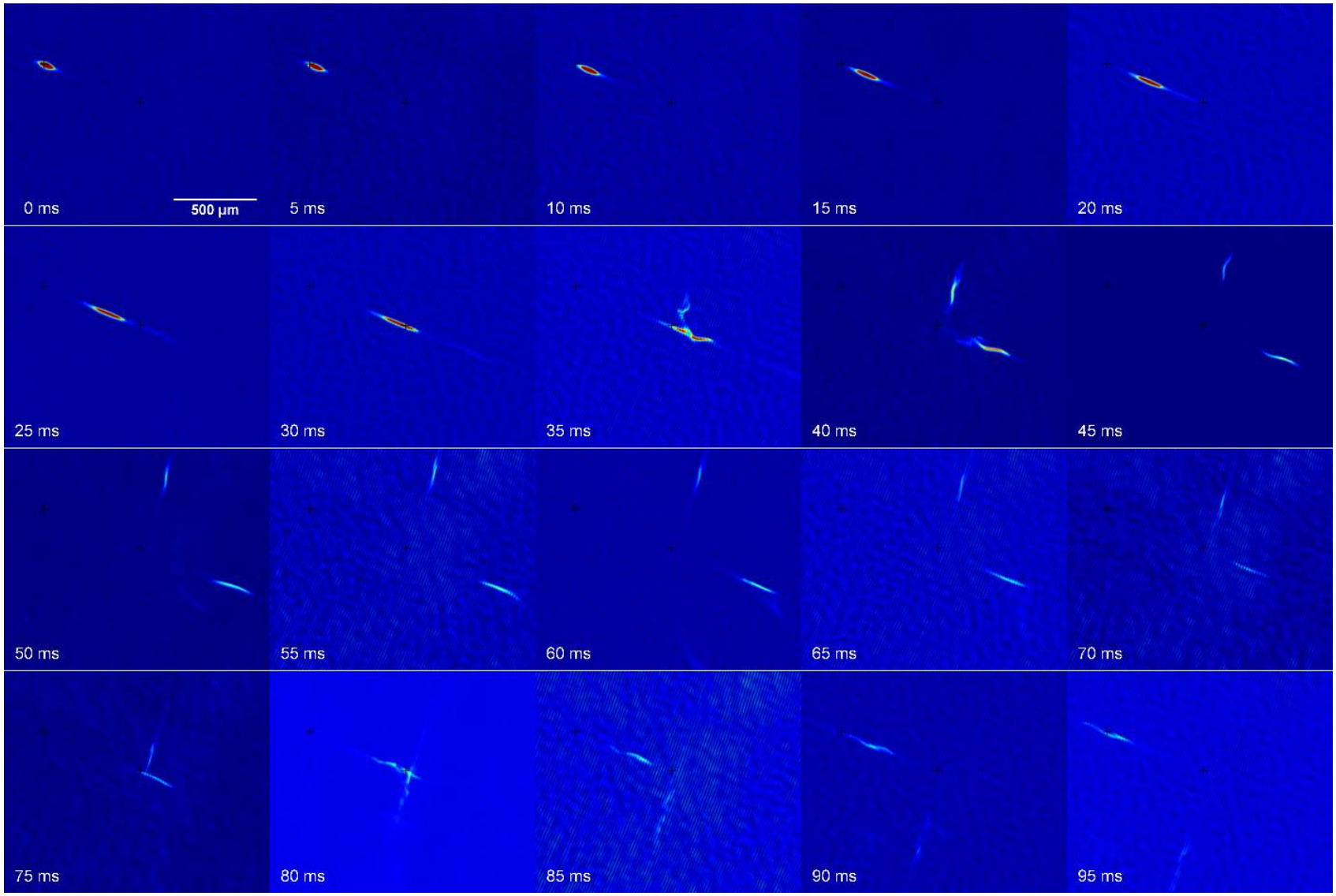

Fig. 5.4 A series of images to show atom position in a Michelson interferometer. Here atoms are 620 µm from the lattice, displayed as two black crosses, and are accelerated to $32.0 \pm 1.6\,\mathrm{mm\,s^{-1}}$ in 30 ms. The lattice amplitude is $\varepsilon = 0.98$. After all atoms have traversed the lattice, two separate magnetic coils are used to reverse the velocity of the atoms. Atoms in WG1 re-enter the lattice with a velocity of $31.9 \pm 2.1\,\mathrm{mm\,s^{-1}}$ and atoms in WG2 similarly re-enter with velocity $34.0 \pm 1.9\,\mathrm{mm\,s^{-1}}$.

lattice exhibit small amplitude oscillations along the transverse direction of the waveguide, shown in Figure 5.5. The amplitude of the oscillation is dependent on the initial velocity of the atoms and is caused by atoms not reflecting from the centre of the lattice. The lattice is formed by two Gaussian laser beams, and so is shaped as a Gaussian envelope with a small periodic potential existing outside the $1/e$ diameter of the beams. As a result, atoms are influenced by the lattice before they reach the centre of the crossing region. For a sufficiently large amplitude lattice, the majority of atoms will be reflected before reaching the centre of the crossing region.

The interaction time between the atoms and the optical lattice is typically long, meaning a large interaction time given as

$$t\frac{E_R}{\hbar} > 1\,.$$

There is also a strong confining potential given as

$$U_{lat} \gg E_R\,,$$

meaning the splitter does not act as a Bragg splitter, but instead occupies the quasi-Bragg regime shown in Figure 4.16 and described in Chapter 4.11. Atoms are therefore unlikely to exit the lattice from the centre, and are instead aligned closer to the edge of WG2. Due to the Gaussian shape of the waveguide, the region of the greatest potential occurs at the centre of the waveguide. As a result, an attractive force moves atoms towards the centre and creates a small oscillatory effect. The effect is dampened after several oscillations due to the weakening potential depth of the waveguide from the increasing beam waist away from the focus.

After the deceleration coils are switched off, atoms in WG1 and WG2 re-enter the lattice with a constant velocity matching the initial velocity. The two atomic clouds enter the lattice simultaneously and interfere, with atoms exiting in both waveguides. Figure 5.6 shows a typical image of the atoms after recombination. The resulting clouds have areas of high and low density atoms unlike the initial splitting in Figure 5.5 where the two clouds have roughly equal density despite the oscillatory effects arising from excitations. The variation in density shows a sign of interference between the two clouds where one waveguide is selectively favoured over the other before reversing.

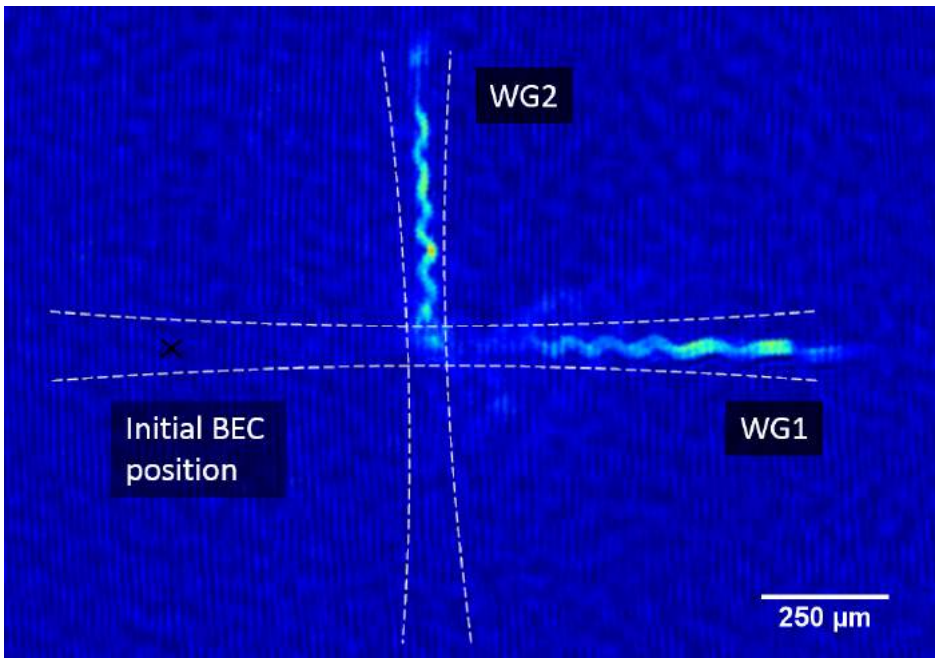

Fig. 5.5 Atoms exiting the lattice acquire a small amplitude oscillation due to atoms not reflecting from the centre of the lattice. In this image WG1 is oriented in the horizontal plane and WG2 in the vertical. A rough outline of each waveguide is depicted as a dashed white line.

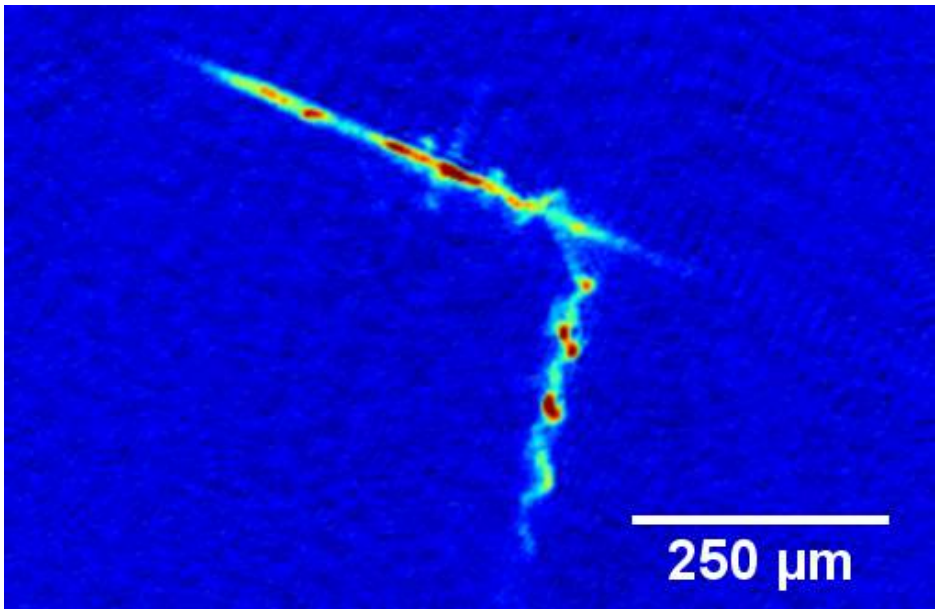

Fig. 5.6 A typical image of atoms in the Michelson interferometer after the initial atomic cloud has split and recombined. A large time of flight is used to accentuate the variations in atom cloud density, leading to visible quasi-momentum states shown in more detail in Figure 4.15.

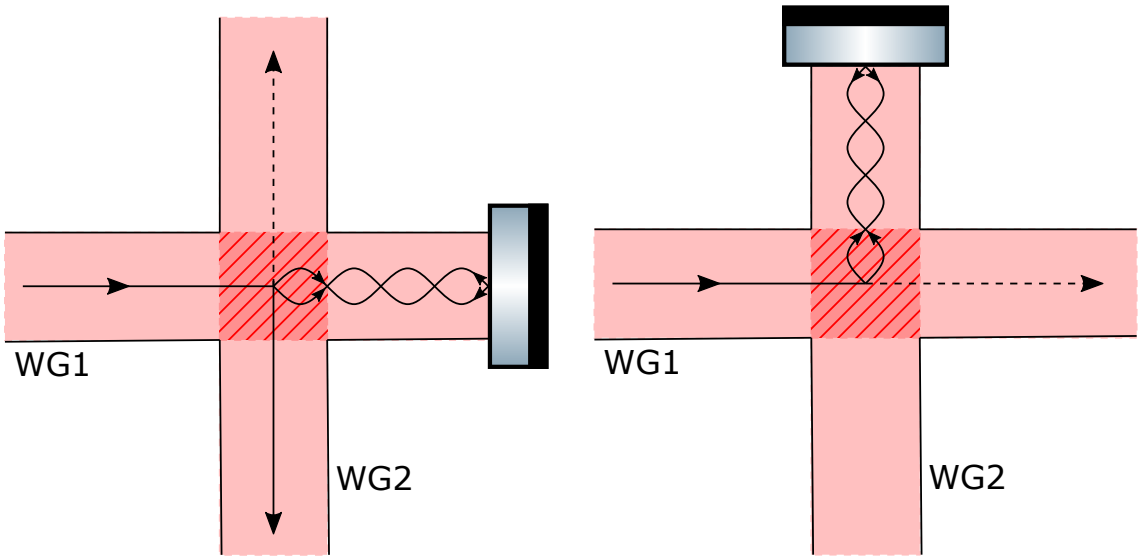

(a) Returning in WG1 only.

(b) Returning in WG2 only.

Fig. 5.7 Two diagrams to show different configurations of a single arm Michelson interferometer used to compare the output signal to a double arm interferometer. Figure 5.7a shows the position of atoms in a double transmission configuration. Similarly, Figure 5.7b shows a double reflection.

5.3 Michelson Interferometer Analysis Method

Understanding the dynamics of the atoms after recombination is essential to understanding the underlying process behind the lattice splitter. Full and separate control over the two waveguides intensities allows for a systematic approach to analysing any interference patterns produced by the recombination of two atomic clouds. To simplify the initial conditions, a single-arm Michelson interferometer is used where atoms are split as normal. One of the waveguides is momentarily switched off to deliberately remove all atoms in that waveguide. The waveguide is returned to full power before remaining atoms re-enter the lattice from a single waveguide, forming a single arm Michelson atom interferometer.

The two configurations obtainable using this methodology are shown in Figure 5.7 where atoms can return from a single waveguide in either WG1 or WG2. Figure 5.7a shows atoms splitting as normal, the intensity in WG2 is reduced to zero before returning. Atoms only remain in WG1 and split in the lattice as normal when recombining. Figure 5.7b shows the opposite, where atoms in WG1 are selectively removed. This method does not excite atoms

in the remaining waveguide and provides a useful comparison to atoms returning in both waveguides simultaneously.

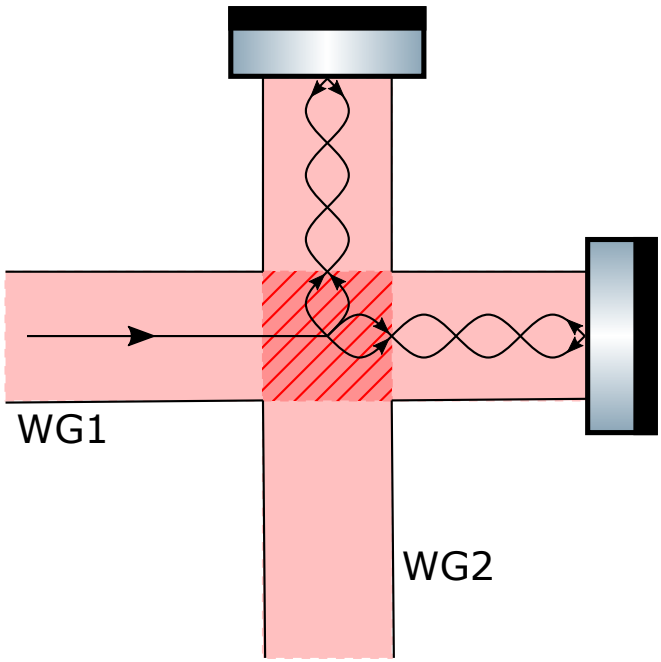

Fig. 5.8 A full Michelson interferometer. Atoms begin in a BEC in WG1 before splitting equally into WG1 and WG2. Applied magnetic fields in each arm reflect the atoms causing them to recombine.

By contrast, Figure 5.8 shows a diagram of a double arm Michelson atom interferometer where atoms are recombined from both waveguides simultaneously after splitting. Comparing splitting results from the double and single arm Michelson interferometer is useful to determine the level of interference generated between the two clouds of atoms.

Analysing the signal from the recombining atoms such as in Figure 5.6 can be achieved using a variety of methods. One such method analysed a single image taken a set time after the atoms have recombined. The atom cloud is then split along the axis of the waveguides into equal thin strips or bins 5 pixels in height and wide enough to encompass the oscillatory motion of the atoms. The number of atoms in each bin is calculated and plotted, giving an intensity profile as a function of distance to highlight the perceived peaks and troughs of intensity. This method was eventually not chosen due to difficulties in aligning the bins to the angle of the waveguides. The initial image is rotated to place one waveguide along the horizontal axis to fit the binning system better. However, the other waveguide will only be aligned along the vertical axis if they cross at 90°. As a result it becomes difficult to directly

compare atom number in one waveguide with the other using a single image. In addition, measuring a single image can accrue large noise fluctuations, whilst averaging over lots of images could remove finer details.

The preferred method used to analyse atoms after recombination is to create two equally sized regions of interest. They are equidistant from the lattice centre along the axis of the waveguides in the direction of travel. The distance between the lattice centre and the region of interest is deliberately chosen to be large enough to ignore any effect of the quasi-momentum peaks described in Chapter 4.11. These regions of interest are used to calculate the number of atoms in the small area. Figure 5.9 shows a sample image with the analysis method superimposed. A series of images are analysed with increasing time, essentially measuring the flux of atoms passing through a set point. The flux fluctuates as the returning atoms selectively favour one waveguide over the other. The chosen area of the region of interest affects the measurement greatly, with a large area blurring out variations in atom density whilst a small area is badly affected by fluctuations in background noise from picture to picture. Typically, images are taken sequentially, increasing the time atoms are in the waveguides by 0.2 ms scanning a total time frame of 20 ms for a total of 100 images. A full experiment cycle is completed every 18 s, resulting in a total time of 30 minutes to complete. The time frame is set by the duration atoms are within the region of interest. The time separation between images is limited by the total time to complete a full sequence. Several sequences are required to provide good averaging and statistics. However, experimental conditions change from day to day, largely through temperature fluctuations or relaxation in mirror mounts affecting coupling to fibres. Therefore, minimising the sequence time is important to improve the overall reliability of results.

Taking subsequent images over a relatively long period also demonstrates the repeatability of the experiment and the deterministic nature of the splitter. By using a full sequence of images, the exact path of atoms in the waveguides is traced. Atom behaviour in the lattice remains constant throughout the image acquisition, and provides a good indication that the spatial and intensity stability of the waveguides described in Chapter 4.1 and Chapter 3.10 respectively is working as intended. It also provides good stability for several hours.

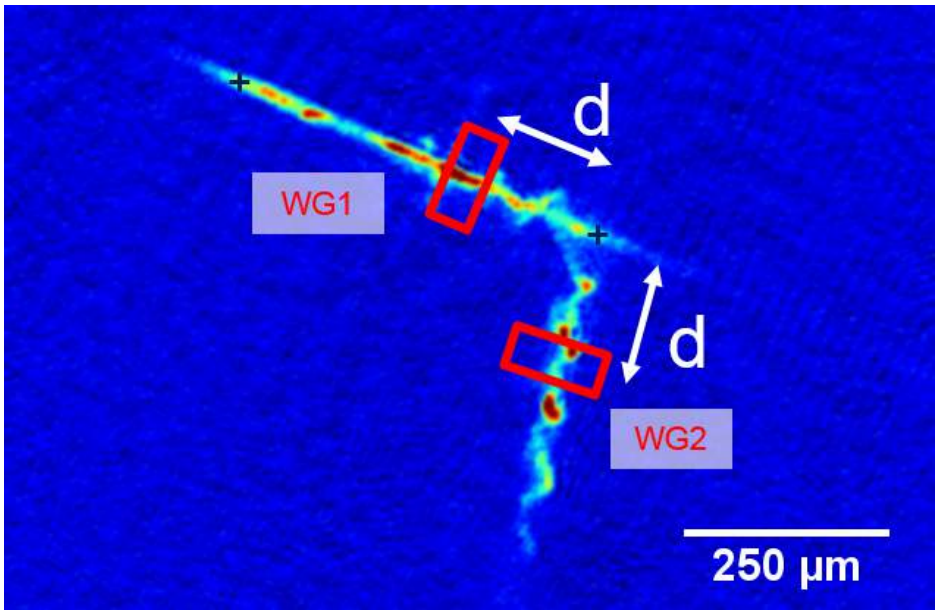

Fig. 5.9 Explanation of the method used to analyse atoms after recombination. The flux of atoms through the red boxes equidistant from the lattice in each waveguide is calculated as a function of time. The distance d is sufficiently large to ignore effects from the quasi-momentum peaks from Figure 4.15.

5.4 Results from Michelson Interferometer Study

A systematic approach to understanding the behaviour of atoms in the Michelson interferometer is vital to understand the optimal conditions required to produce clear signs of interference. As a result numerous combinations of initial atom velocities, lattice strengths and waveguide separation angles are attempted. The optimal conditions found in Figure 4.13 are used to set the atom velocity range between 25 mm s^{-1} and 35 mm s^{-1}. The initial atom cloud will be split equally into the two waveguides. All parameters are kept constant whilst the magnetic coils are applied to invert the velocity of the atoms before recombining. After a sequence of images is taken, the analysis method explained in Chapter 5.3 is used to measure the fraction of atoms returning in one waveguide relative to the other.

A typical example of the signal found when atoms return and split is shown in Figure 5.10 where the flux of atoms in WG1 is measured as a fraction of the flux in WG2. Atoms are initially accelerated to 26.5 mm s^{-1} and are split equally. Atoms in both arms are kept and recombined to form a full Michelson interferometer sequence. Defining $t = 0$ ms as when the atoms enter the lattice for the first time, $t = 30$ ms is the average time atoms are separated in two waveguides. The magnetic coils are activated for 25 ms and are switched off before atoms

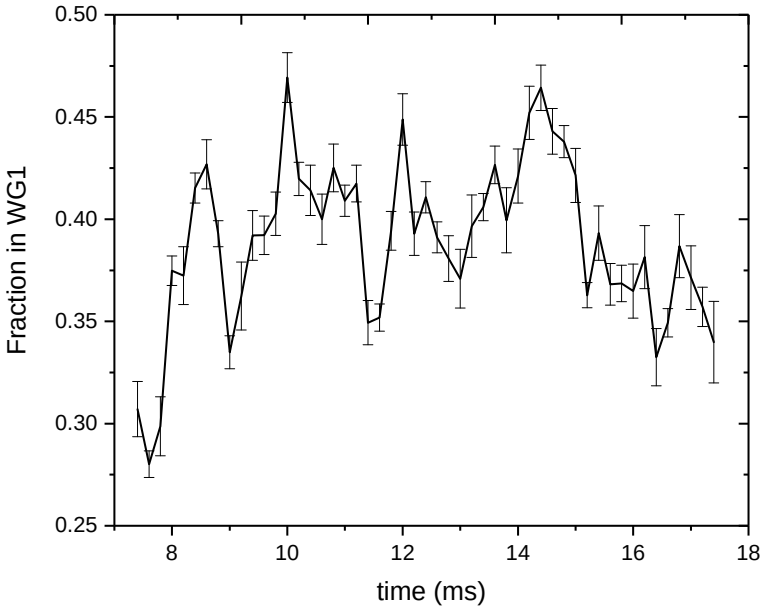

Fig. 5.10 A graph displaying the flux of atoms passing through WG1 after recombination as a fraction of the equivalent flux in WG2. Initial atom velocity is 26.5 mm s^{-1}, data is averaged over 5 consecutive runs and WG1 and WG2 had powers of 16.9 mW and 16.2 mW respectively. Atoms return from both WG1 and WG2 simultaneously to form a full Michelson interferometer sequence.

re-enter the lattice. An average of 5 datasets is taken with several iterations of atom velocity, spanning a time frame in excess of 7 hours. A small relaxation of optics is observed over such a large time, affecting the average and increasing the associated standard error. As a result future measurements were taken rapidly, with fewer averages to minimise experiment drift. A further point to note is the average fraction in WG1 is significantly below 50%, indicating the returning atom velocity has changed likely from variations in the waveguide intensity. Maintaining a constant returning atom velocity represents one of the biggest difficulties in this experiment and is addressed later. The oscillation amplitude is approximately 10% and is in part limited by noise in the images. Although a full sequence covers a 20 ms timespan, the two atom clouds are only fully overlapped for a fraction of this time, due to varying returning atom velocities and arm lengths. In Figure 5.10 the overlapping period is from 8 ms to 15 ms. Outside of theses times, the data becomes less useful as atoms are predominantly returning from a single waveguide.

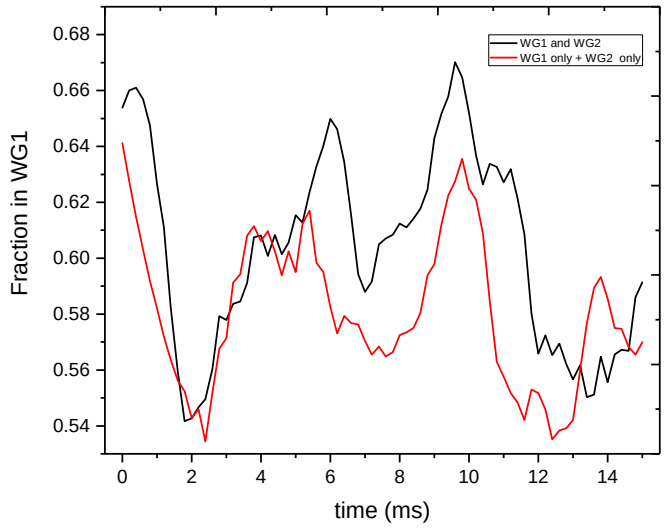

Fig. 5.11 A comparison between atoms returning in a single waveguide and atoms returning in both waveguides simultaneously, forming a single or double arm Michelson interferometer shown as a diagram in Figure 5.7 and Figure 5.8 respectively.

An additional useful comparison to make is from the summation of signals arising from two single arm interferometers, with atoms returning in either WG1 or WG2. Two separate sequences are performed with identical parameters such as initial atom velocity and lattice amplitude. However, after atoms are separated into two clouds, the intensity in one waveguide is reduced to zero. Atoms in that waveguide are deliberately lost and the waveguide is returned

to its original intensity before remaining atoms in the other waveguide return to the lattice. A double arm interferometer sequence is also taken as a comparison. Analysis of the flux is identical for all three sequences. The flux from the two single arm interferometer sequences is summed to simulate a double arm interferometer with no interactions between atoms in different quantum states.

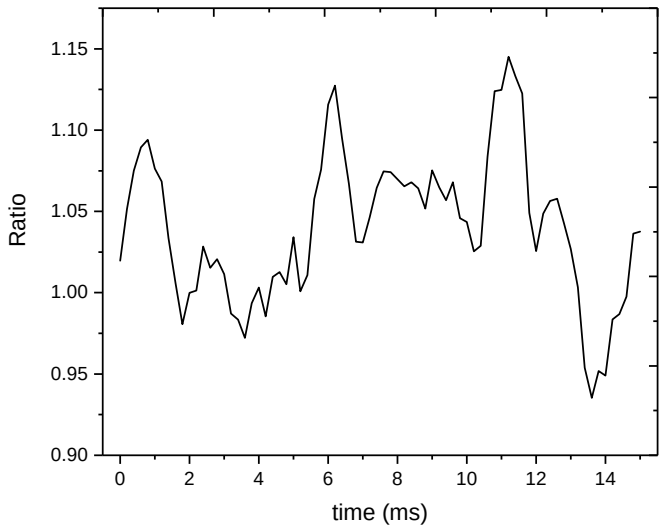

Fig. 5.12 A graph to show the ratio of a double arm and simulated double arm interferometer shown separately in Figure 5.11. Three clear peaks are visible indicating the slight offset between datasets.

The resulting comparison is shown in Figure 5.11 where three sequences were taken with an initial atom velocity of $35\,\mathrm{mm\,s^{-1}}$, power in WG1 and WG2 is 19.4 mW and 16.4 mW respectively. Slight differences in power in the waveguides can be necessary to ensure that atoms are held against gravity. At higher initial velocities atoms will travel further from the waveguide beam waist and therefore require a higher intensity to resist the effects of gravity. The oscillation amplitude is roughly equal to Figure 5.10, at 10% and the oscillation period is roughly 2.5 ms for both datasets. At first glance there is a large similarity between the data from single and double arm interferometer sequences, implying there is little interaction between the atoms in each waveguide as they recombine.

However, the two curves are not identical and the ratio of the two is shown in Figure 5.12. Three clear peaks are visible, corresponding to the maximum flux of atoms in WG1. The amplitude of the peaks is roughly 10%, also matching Figure 5.11. The large deviation

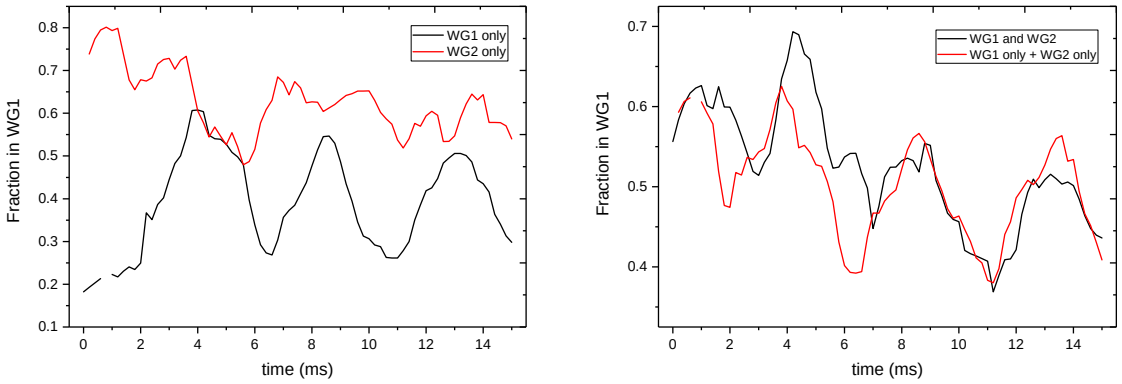

(a) Single arm interferometer.

(b) Double arm interferometer.

Fig. 5.13 A comparison of single and double arm Michelson interferometers at 30 mm s^{-1}. Figure 5.13a compares the flux of atoms in WG1 when atoms are returning in a single waveguide, WG1 or WG2. Figure 5.13b compares the combined signal of two single arm interferometers with a double arm interferometer. The combined signal from single arm interferometers simulates a double arm interferometer.

away from an equal ratio is strong evidence demonstrating the effect of two clouds of atoms recombining.

Figure 5.11 can be further deconstructed to plot the individual signal generated from two single arm interferometers, with atoms returning in either WG1 or WG2. This provides useful information when compared to the signal generated from a double arm interferometer sequence and is shown in Figure 5.13. In additional to plotting the separate signals in Figure 5.13a, the combined signal plotted against the double arm interferometer is shown in Figure 5.13b. Further upgrades such as the introduction of power stabilisation have helped to increase the peak amplitude to approximately 30% when atoms are returning in WG1 only. This is discussed further in Chapter 3.10. The sine wave generated by the atom flux is more consistent than previous attempts and a slight damping effect is observed with increasing time, reducing the amplitude to 25% over 12 ms. The estimated frequency of the oscillations is 210.0 ± 3.5 Hz. This value is close to the radial frequency of the waveguides calculated in Chapter 4.3 and could be a contributing factor towards the oscillatory motion of atoms after the lattice. Conversely the flux from atoms returning in WG2 shows no clear sign of oscillation despite a large population fraction measured in WG1. Figure 5.13b compares the sum of the two single arm interferometer sequences in Figure 5.13a with a double arm

interferometer sequence. The strong correlation between the two signals agrees with earlier data taken, shown in Figure 5.11.

5.5 Further Analysis of Interferometer Signal

Whilst the splitting and recombination of atoms are clearly affected by entering the lattice, the exact mechanism causing the fragmentation upon recombination is still not completely understood. Additional analysis systematically measuring different sources of noise in the Michelson interferometer sequence are tested. This will systematically address any individual sources of noise. Firstly, more information on the splitter was attained by performing the same analysis technique from Chapter 5.3 on the atom cloud. However, the cloud is split at different points in time in the Michelson interferometer sequence. This will increase understanding on where the oscillation signal originates from, and decide if it is just an artefact of the splitter.

Initially, the analysis is performed after the cloud splits once into two equal fragments. To compare, the analysis is also performed on atoms which are only split upon returning to the lattice. This is achieved by accelerating atoms as normal in WG1 with the intensity of WG2 set to 0 to prevent any reflection on the first pass. Atoms are then decelerated as normal and the intensity in WG2 is returned to its original value before atoms re-enter the waveguide crossing. Upon entering the lattice, atoms will split. Figure 5.14a and Figure 5.14b plots these scenarios, measuring the fraction of atoms in WG1 as a function of time. The measured flux area is constant in both sequences. The graph indicates the difference in atom splitting behaviour after a longer time is spent in the waveguide and a magnetic coil applies a slight off-axis force, providing excitations to the cloud. Atoms splitting on the first pass through the splitter as normal exhibit usual behaviour observed from previous data shown in Figure 4.14. Initially, a high percentage of atoms are transmitted by the lattice and remain in WG1. Due to the velocity distribution of atoms within the atom cloud, faster atoms enter the lattice first and are therefore more likely to be transmitted. As the cloud passes through the lattice the average velocity of individual atoms decreases, which is observed in Figure 5.14a by a decrease in WG1 population. The majority of the cloud passes through the lattice within 15 ms and data after this point becomes less reliable. The cloud traverses the lattice more rapidly on the first pass due to the velocity distribution which increases the length of the cloud over time.

Predictably atoms spend longer in the lattice but there is no observed decrease in WG1 population over the duration the atom cloud is passing through the splitter until the tail end. This provides unreliable results due to decreased atom population. A small < 10% amplitude oscillation is visible despite the fact that atoms only enter the lattice once. It is possible that a small inherent excitation is generated either from the waveguides, the lattice or the magnetic field gradient which creates oscillatory behaviour. However, the oscillation amplitude is significantly larger when two clouds are recombining as shown in Figure 5.14c. Here the oscillation amplitude is close to 30% with a frequency of 179.9 ± 3.4 Hz, similar to the value measured in Figure 5.13b. All parameters of the sequence are identical, ruling out any effect of increased noise from the magnetic field gradient. Therefore, the effect of applying a lattice to split and recombine the cloud of atoms can be determined as the difference between the signal in Figure 5.14b and Figure 5.14c plus the sum of any additional excitation accumulated during the second lattice interaction.

A second variable and source of noise is the two orthogonal magnetic field gradients applied during the deceleration of atoms in both waveguides. As mentioned previously the gradient axes are not aligned well to either waveguide due to geometric limitations of the science chamber and is partially responsible for creating visible oscillations in the atom cloud as it travels through the waveguide. To gauge the effect of any excitations directly caused by the magnetic coils, atoms are accelerated as normal before being decelerated in one of two ways. Firstly a single coil is used to decelerate the atoms. The additional coil primarily used to decelerate atoms in WG2 is unable to generate a large enough magnetic field gradient to decelerate the atoms sufficiently by itself. As a result, the single coil that forms the pair of anti-Helmholtz coils to form the MOT is used. For this reason atoms can only be decelerated in WG1 when using a single coil. Secondly, atoms are returned in WG2 using both coils in the normal arrangement as a control. The velocity of atoms in both sequences is equal as are all other experimental parameters.

Figure 5.15 shows a comparison between the two configurations. Atoms are initially accelerated to $28.8\,\mathrm{mm\,s^{-1}}$ or $6.7\,v_R$ before entering the lattice and splitting equally into the two waveguides using a lattice amplitude of $\varepsilon = 0.5$. In Figure 5.15a a single coil is used to return atoms in WG1, with no contribution from the additional coil. To ensure no atoms remain in WG2 it's intensity in WG2 to zero. This also helps to keep parameters equal when comparing results to a situation where atoms are returning in both waveguides. An average of 5 sequences were taken over a timespan of roughly 3 hours. Despite the large error resulting from variations in the initial size of the BEC over a relatively large period,

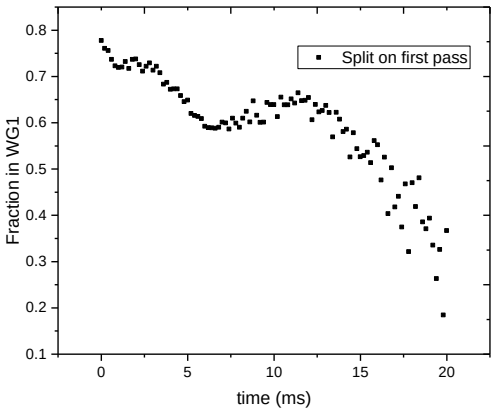

(a) Split on first pass.

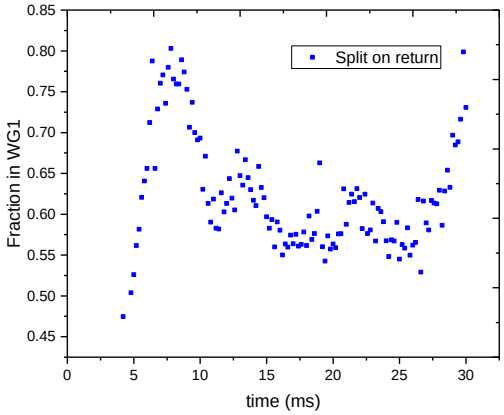

(b) Split on second pass.

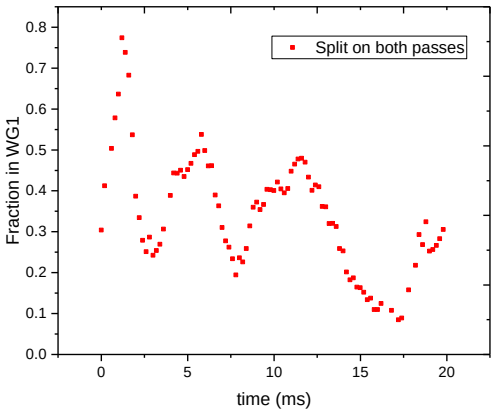

(c) Atoms split as normal.

Fig. 5.14 A comparison showing the effect of applying the lattice to atoms in the waveguide once or twice. Atoms in Figure 5.14a and Figure 5.14b are split once by the lattice, on either the first or second pass respectively. Atoms in Figure 5.14c are split on both passes through the lattice as normal.

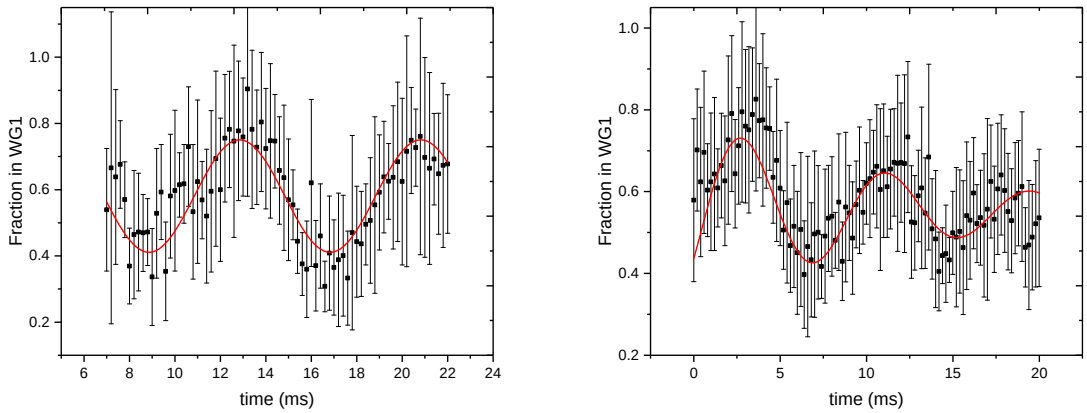

(a) One coil used.

(b) Two coils used.

Fig. 5.15 The flux of atoms in WG1 is measured when using a single magnetic coil to accelerate and decelerate the cloud. As a result atoms only return in WG1, the waveguide best aligned along the axis of the coil. The resulting fragmentation is shown in Figure 5.15a. The equivalent measurement with equal atom velocity is taken when using both coils as a comparison, again with atoms only returning from WG1 and is shown in Figure 5.15b.

a clear oscillatory signal is present with an amplitude of over 35%. A sine curve is fitted to the data, yielding a frequency of 125.3 ± 3.1 Hz. The frequency does not match earlier measurements compatible with the radial frequency of the waveguides. This is because the intensity of the waveguides were increased to prevent atoms falling out of the waveguide when returning atoms using a single coil. It indicates initially that the effect of excitations relating from improper alignment of the magnetic field gradients is significant.

This result is compared with a sequence which utilises the second additional coil as normal. The two coils are not aligned along the axis of the waveguides so a new calibration was required, as the coil designed to accelerate WG1 also has a small effect on the motion of atoms in WG2 and vice-versa. As a control, the velocity of atoms returning in WG1 was set to be constant by adjusting the balance in both coils. The results from using both coils is shown in Figure 5.15b where an average of 5 measurements is plotted. A large error signal is a result of a poor signal-to-noise ratio in the imaging which creates large variations in the number of atoms recorded when averaging. The overall uncertainty in the measurement is comparable between the two datasets and an oscillatory signal is present. However, clear signs of damping are evident. The frequency of the oscillation is 119.6 ± 2.6 Hz and so is compatible with the frequency calculated in Figure 5.15a. The half-life τ of the damped curve is 8.8 ± 2.1 ms. As the frequency of the two curves in Figure 5.15 are comparable, it

can be concluded that the frequency of the oscillation is not affected by the extra excitations arising from the additional coil. However, there is a clear effect on the amplitude of the oscillation where a maximum of 30% is recorded before reducing to roughly 12% as a result of excitations from the additional coil affecting the fractional population in each waveguide.

From these two trials it can be concluded that the acceleration technique infers a small excitation on the atoms in the waveguide, and is negatively affecting the sensitivity of the measurement. In addition, the fragmentation observed by the atom cloud is an effect of the lattice and is greater when atoms are recombining from two separate waveguides.

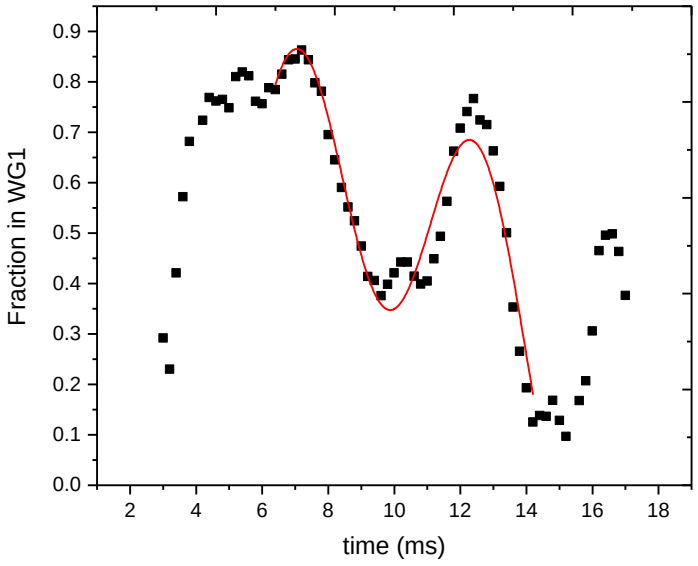

Fig. 5.16 A Michelson interferometer double arm sequence showing large amplitude oscillations. Evidence of a double sine curve is also present, indicating the addition of two separate sine curves, possibly generated by atoms returning from both waveguides simultaneously.

Subsequent upgrades to the experimental apparatus and sequencing greatly increased the sensitivity of the experiment, leading to further insight into the dynamics of atoms in the trap. Following many sequences with various iterations of variables, the optimal settings to generate maximum amplitude splitting were found. An average separation between the BEC and waveguide crossing of 700 µm is used. Coupled with waveguide power in WG1 and WG2 of 16.5 mW and 19.6 mW respectively, the atoms are strongly confined against gravity with an axial frequency of 1.35 Hz. Subsequent incremental upgrades to the BEC loading process now yield up to 10^5 atoms in a single m_F state, increasing the signal-to-noise

ratio significantly. The optimal splitting angle with respect to the geometry of the science chamber and crossing area is 95°. An average initial atom velocity of 29 mm s^{-1} is achieved using the maximum permissible current in the shortest possible time to prevent additional excitations. Atoms can be accelerated to a velocity in excess of 40 mm s^{-1} in 5 ms. Similarly, deceleration time after the initial split is minimised. However, the increased distance between the coils and atoms, as well as a greater total momentum transfer requirement, leads to a longer time to decelerate of 30 ms. Using the optimised conditions for splitting, an oscillation amplitude in excess of 40% is achieved and shown in Figure 5.16 where a double arm Michelson interferometer sequence is shown. The increase in sensitivity reveals a curve that closely resembles a sum of two separate sine curves which follows the form

$$f(x) = A\left[\sin(\omega_1 x) + \sin(\omega_2 x)\right], \tag{5.2}$$

where A, ω_1 and ω_2 are all constants. The fit is only applied to the data where maximum overlap with equal flux between the two recombining atom clouds occurs. A visible double sine pattern leads to a reasonable conclusion that the flux variation generated by two clouds recombining is simply a summation of the signal from each separate cloud. The frequency of the two sine curves from the fit is given as

$$f_1 = 30.2 \pm 2.3 Hz,$$
$$f_2 = 179.8 \pm 0.7 Hz.$$

The f_2 frequency agrees well with previous measurements shown in Figure 5.13b and Figure 5.14 and is close to the radial frequency of the waveguides as previously described in Figure 4.5. Conversely, the value of f_1 is the difference between the radial frequency of the two waveguides.

The minimum duration atoms occupy in the waveguide between initial splitting and recombination is limited by the magnetic field coils to 30 ms. However, the time atoms are in the waveguide after splitting can be varied and increased by applying two temporally separated magnetic field gradients. The first reduces the atom velocity close to 0 mm s^{-1} as the atoms reach the maximum separation from the lattice. After an adjustable delay, a second magnetic field gradient re-accelerates atoms to the initial atom velocity before recombination. The

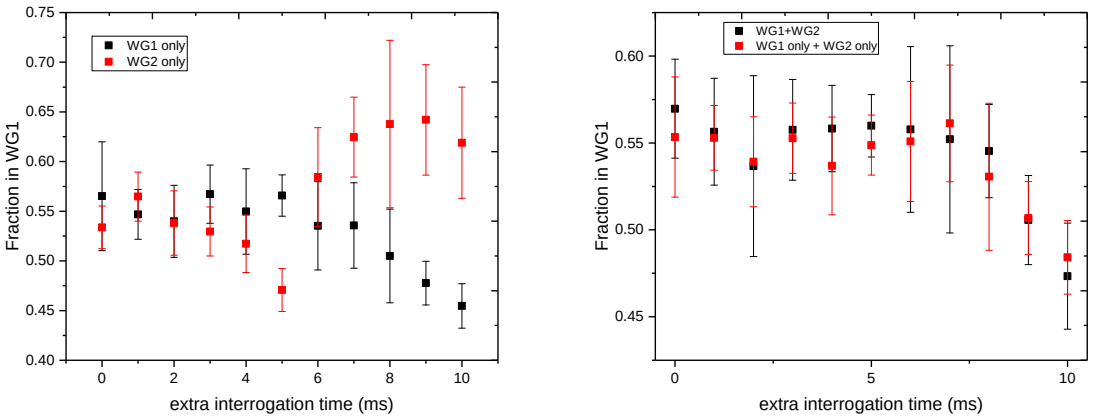

(a) WG1 and WG2 returning separately.

(b) WG1 and WG2 returning together.

Fig. 5.17 Effect of varying the time atoms are held in the waveguides after splitting. A total of 3 sequences were taken with atoms returning in WG1 only, WG2 only or WG1 and WG2 together. Data was repeated 5 times to gain an average.

effect on the fractional atom population is shown in Figure 5.17, where the extra interrogation time is varied from 0 ms to 10 ms. The initial atom velocity is 38.6 mm s^{-1}, chosen as the maximum achievable velocity that provides equal splitting into both waveguides with maximum lattice amplitude. Due to the higher velocities atoms travel further from the waveguide focus, requiring slightly increased intensity to keep atoms trapped against gravity. WG1 and WG2 are 21.0 mW and 16.2 mW respectively. Figure 5.17a shows the fraction of atoms in WG1 when atoms are returning from a single waveguide as a single arm Michelson interferometer. Figure 5.17b shows data from a double arm interferometer, using the combined data from the sum of atoms returning in separate waveguides compared against a sequence where atoms return in both waveguide concurrently. The large errors make any analysis difficult and are caused by atom losses when the clouds are held at large distances from the focus for longer periods of time. Despite the stationary atoms being well within the Rayleigh length of the beams, a small number are lost from the trap over time. Spatial and intensity fluctuations of the waveguides are the likely cause, and reduces the sensitivity of the experiment.

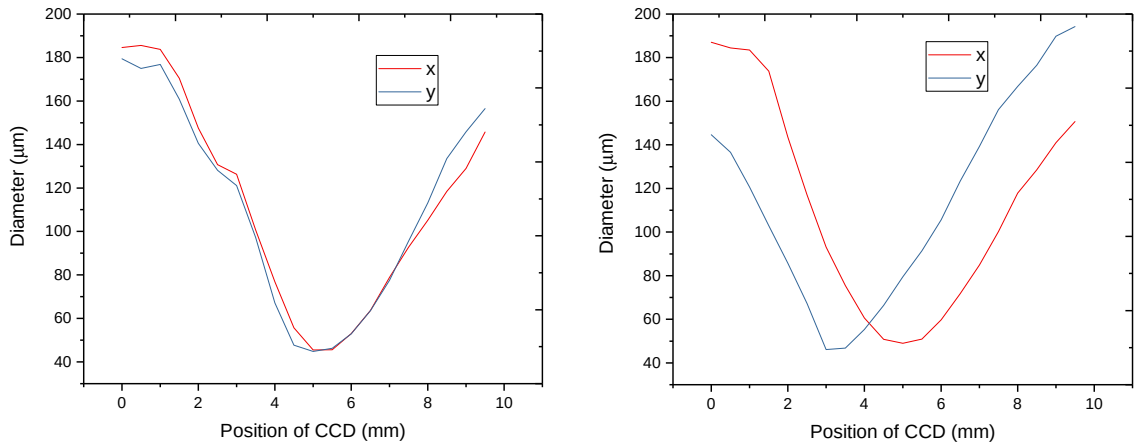

(a) 0 degree incidence angle.

(b) 45 degrees incidence angle.

Fig. 5.18 An uncoated glass plate is placed in-between a focused 1064 nm laser beam and a CCD camera at various incidence angles. The resulting aberrations created from the glass plate shifts the position of the minimum beam waist in both axes.

5.6 Study on Waveguide Minimum Beam Waist

The glass cuvette used to trap the atoms is uncoated and so creates reflections from all incident light. The reflected percentage is calculated to be as high as 5% of the incident light. This loss in power is accounted for when setting waveguide intensities. However, the profile of the waveguide beam was not tested due to difficulties in recapturing the beam after exiting the cuvette. WG2 enters close to normal on the end of the cuvette, meaning the beam exits at a shallow incidence angle in the glass to metal transition, visible in Figure 3.1, further distorting the beam and preventing any reasonable measurement.

A small test bench was used to simulate the effect of light incident on uncoated glass with the same parameters as a waveguide. The increased power in WG2 for some Michelson interferometer sequences is postulated to be caused by a deformation in the Gaussian wavefront as it is incident on the cuvette at an oblique angle. An uncoated glass plate with a similar thickness to the cuvette is placed between the test waveguide beam and a CCD camera used for imaging. Light enters the fibre but the waveguide outcoupler is deliberately misaligned to reduce the coupling efficiency to the point where the CCD is not saturated at the minimum beam waist. The CCD camera is placed on a translational stage and roughly aligned to the minimum beam waist. Images were taken at regular intervals along the axis of the beam and the $1/e^2$ diameter was calculated. The process is repeated with the glass sample rotated to

several angles to simulate light entering the cuvette at different incidence angles. Figure 5.18 demonstrates the extreme difference in the shape of the beam near the minimum waist after passing through a glass plate. In Figure 5.18a the incidence angle of light to the cell is 90°. The minimum beam waist is 22.5 µm, agreeing well with the expected value calculated using Equation 4.1 with a 200 mm focusing lens and an initial beam size of 6 mm. Figure 5.18b shows the same experimental parameters with the glass cell rotated by 45° to simulate a large incidence angle of 45°. The minimum beam waist is 24.5 µm and 23.0 µm along the x-axis and y-axis respectively, aligned to correspond to the horizontal and vertical direction. However, the minimum beam waist in both axes no longer occurs at the same focal length, meaning the beam is deformed and the minimum waist is significantly larger at any given point. The minimum beam waist is separated by 1.75 mm. When the beam is aligned to minimise the beam waist along the x-axis, the y-axis beam waist is almost 40 µm. One notable consequence of this is the reduced trapping potential generated by the waveguide as a result of an increased average beam waist. As a result the potential depth of the waveguide is reduced from 6 µK to 5.1 µK, a 15% reduction. Atoms travelling in the waveguide are therefore lost to gravity at shorter distances from the minimum beam waist, and explains why the power in WG2 is required to be higher than in WG1, as it enters at a more oblique angle.

As a direct consequence of these results, a major redesign of the optical delivery systems was implemented to allow the waveguides to enter the cuvette at an angle close to normal. One MOT beam pair originally occupied the normal angle of incidence to the cuvette and was required to be offset by 10° to make room for a waveguide outcoupler. Preliminary tests showed offsetting one MOT beam pair caused only minor decreases in MOT size up to 15° from normal and had little to no effect on the dipole trap or BEC population. In addition, the dipole trapping beam was reorientated to operate along a vertical axis with the same crossing angle and parameters in Chapter 3.11. Figure 5.19 shows a diagram of the new layout with the optical beams. The MOT beam pair is slightly offset to allow WG1 to enter the cuvette with a low angle of incidence, also aligning it closer to the axis of the magnetic coil. The initial dipole trap path is preserved but the return beam crosses along the vertical axis to save space on the optical table for future upgrades. WG2 is unable to enter the cuvette at a normal angle as light has to be able to exit the chamber to prevent large unwanted scattering of light and instead enters at a shallow angle of incidence of 10°.

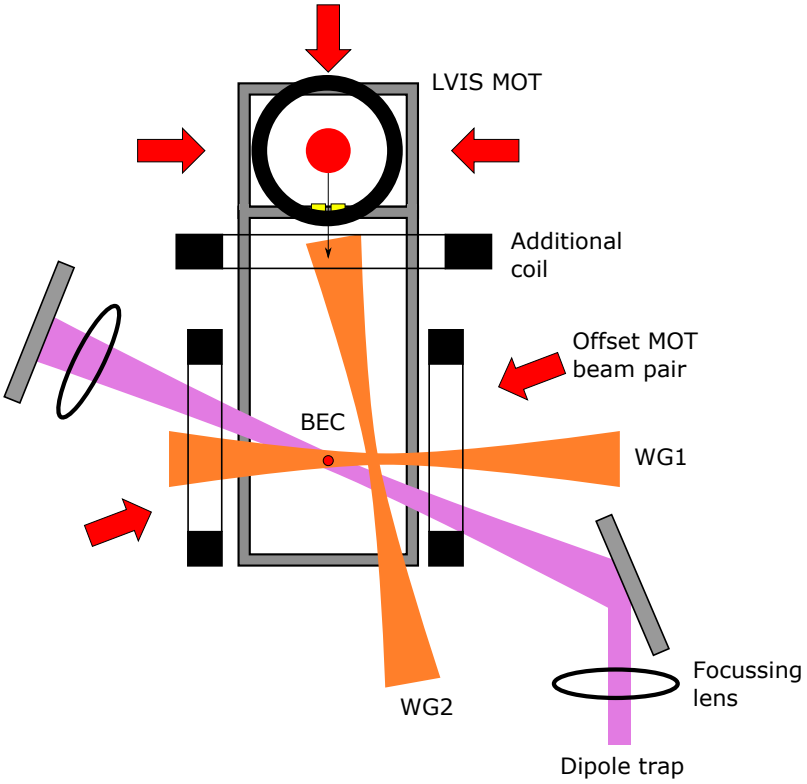

Fig. 5.19 Not to scale. A diagram showing the updated optical beam delivery system which prioritises the placement of the waveguide beams to minimise distortion from the uncoated glass cell by placing the WG1 outcoupler to be incident on the cuvette close to normal.

5.7 Planned Upgrades

The next generation of upgrades to the experiment will aim to reduce sources of noise imparted on atoms in the waveguides, as well as improving loading and BEC size. Following work in Chapter 5.5 it is apparent that improvements to the acceleration method of atoms in the waveguides are vital to reducing overall noise and repeatability of the experiment cycle. In particular, it would be beneficial to remove any reliance on magnetic fields as atoms could be loaded into the magnetically insensitive $m_F = 0$ state using the selective loading method in Figure 3.25b.

One simple upgrade to improve the quality of the waveguides is to create an outcoupler using a fibre and lens tubes to first create a good approximation of a Gaussian beam, before using well aligned optics to focus the beam to form a waveguide. An example of one of the new waveguide outcouplers is shown in Figure 5.20. Originally the waveguide beam was created using optics in free space. However, the beam path was regularly changed to vary the separation between the BEC and WG1, resulting in the beam not passing through the centre of the optics. This affects the beam quality and results in an imperfect focus. To mitigate these issues light is instead coupled into a fibre to ensure a Gaussian shaped beam. The waveguide beam is therefore created similarly to the 3D MOT beams shown in Figure 3.9, through use of a fibre outcoupler. Light from the fibre naturally expands before being collimated to a diameter of 6 mm. A polarising beamsplitter is used to clean the polarisation of the beam before a $\lambda/2$ waveplate is used to determine interference amplitude ε of the lattice. Finally, a 200 mm lens focuses the beam to a waist of 22.6 µm. The waveguide outcoupler represents a significant upgrade over the original design which were designed in free space. As a result, they suffered from significant aberrations as constant realignment to the BEC resulted in the beam drifting from the centre of the focusing lens over time. A similar problem was created when expanding the beam to create a smaller beam waist, small deviations in beam path amplified aberrations from the telescope lenses. Moving the system to a pre-aligned lens tube configurations drastically improved the Gaussian profile of the beam.

The new dipole trap configuration, shown in Figure 5.19, will feature a slightly reduced trapping potential due to the vertical orientation and will slightly compromise the evaporative cooling due to gravitational force on the trapping potential. One simple method to overcome this limitation is to use WG1 as an additional trapping potential, similar to its use as a dimple in Chapter 4.2. However, instead of providing a small trapping potential that is only relevant at the end of evaporation, it will provide comparable trapping to the dipole trap. The potential

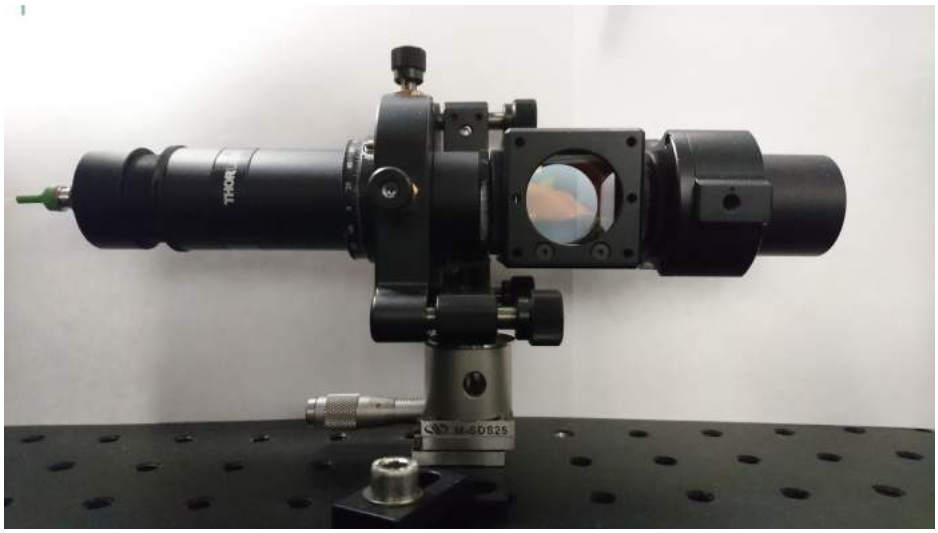

Fig. 5.20 An image of the newly designed outcoupler used to create a focused beam to act as a waveguide for atoms in the BEC.

of WG1 will be ramped down identically to the dipole trap, with the larger trapping area and greater trapping potential increasing the number of atoms condensed into a BEC.

One proposed method to replace the magnetic acceleration is to use a common technique in frequency fountains [136] to launch atoms optically using a counter-propagating beam. In a frequency fountain this is achieved by increasing the frequency of the upward facing MOT beams and simultaneously decreasing the frequency of the downward facing beams. This creates a moving standing wave, transporting atoms. The method is well understood and can launch atoms vertically to heights of several metres [137]. To accelerate atoms in the waveguide, a counter propagating beam to WG1 with similar beam waist and power can be shifted in frequency using an AOM to generate a moving standing wave which will impart a force on the atoms. This method provides many benefits over the current magnetic coil acceleration. Firstly the acceleration axis will be well aligned with the waveguide and is easily adjustable, and will minimise excitations generated from the off-axis magnetic field. Secondly, the acceleration can be performed faster. A typical fountain experiment is capable of accelerating atoms to $0.12\,\mathrm{m\,s^{-1}}$ in 9 ms [138], significantly faster than the current magnetic method and far in excess of what is required. The push beam will be controlled with a separate AOM and shutter to ensure no residual light from the push beam remains as atoms enter the lattice. This method is unable to be used to decelerate atoms in WG2 in a 90° configuration due to the geometry of the cuvette preventing a retro-reflection as mentioned in Chapter 5.6.

To fully eliminate reliance on magnetic acceleration, a new method to decelerate the atoms after splitting is required. An additional desirable benefit is to have full independent control over the length of the Michelson interferometer arms. This will allow more precise testing of the presence of any interference fringes by systematically varying the length of individual arms. A way to achieve both of these goals is to use focused laser beams, blue detuned to the rubidium transition to act as potential barriers to the atoms. Blue detuned light will create a positive guiding optical dipole potential and creates a repulsive force to the atoms. Two independent blue detuned beams will intersect with the two waveguides at a controllable distance from the lattice and will be aligned normal to the waveguides. The shape of the blue detuned beams could be a light sheet [139] or a focused Gaussian beam as there is no desire to trap the atoms. A light sheet is preferable to maintain an equal potential barrier over the width of the waveguides and to prevent small misalignments over time, but requires higher power.

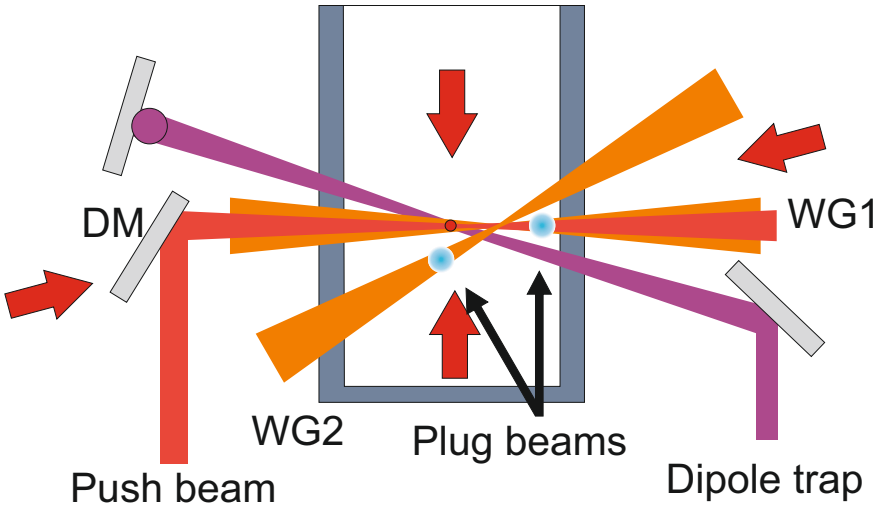

Fig. 5.21 Not to scale. Two upgrades to the experiment setup to remove reliance on magnetic field gradients to accelerate and decelerate the atoms. The push beam is used to accelerate atoms and the plug beams are blue detuned and act as a potential barrier, reflecting the atoms.

An additional improvement to the optical delivery system will utilise a dichroic mirror to reflect 1064 nm and transmit 780 nm light to allow a closer overlap of the MOT and WG1, potentially allowing them to both propagate along a normal incidence angle to the cuvette. Further reductions to unwanted aberrations and reflections from the uncoated glass of the cuvette will help to reduce unwanted light in the chamber. Despite a normal angle of incidence representing the minimum aberrations on the beam focus, it is necessary to slightly offset the waveguides from normal. The uncoated glass of the chamber will create a

5% reflection for any incident light and will in effect create a small retroreflected beam if aligned normal to the glass. This will create a small standing wave along the length of the waveguides and disrupt the motion of atoms within. To mitigate this effect, the waveguides are slightly offset from normal by roughly 5°.

A simple diagram of the proposed implementation of the push and blue beams is shown in Figure 5.21, as well as an indication of how a dichroic mirror would operate. A minimum of a 50 mm diameter mirror is required to allow the MOT beam to transmit through the angled mirror without interruption. An additional benefit to removing reliance on magnetic acceleration is that any angle θ can be considered between the two waveguides as they are no longer bound by the axis of the magnetic field coils. In the diagram a large angle splitter is shown with $90° < \theta < 180°$. In this scenario the lattice generated by overlap between the two waveguides is increased, leading to a larger interaction area with more reflections between atoms and lattice peaks.

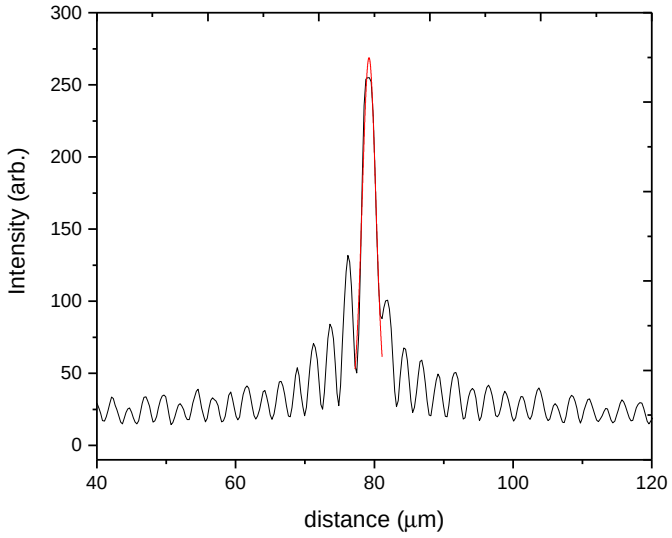

Fig. 5.22 An intensity profile of a Bessel beam generated using a conical axicon lens and imaged using an objective with 20x magnification onto a CCD camera. The central peak is fitted with a Gaussian and the $1/e^2$ diameter of the central peak is 3.9 µm.

Preliminary work has started on improving the trapping potential generated by the waveguides by reducing the minimum beam waist. The current beam waist is limited by the size of the optics as the waist is inversely proportional to the initial diameter of the beam from Equation 4.1. The linear inverse proportionality results in large initial beam diameters

to generate smaller minimum waists for a given focal length which becomes difficult to align and requires larger optics. One possibility to circumvent these issues is to use a non diffracting Bessel beam whereby the minimum beam waist can propagate over a relatively large distance, z_{max}, without diffracting. A Bessel beam is created using an axicon lens which features a rotationally symmetric conical surface on one side to focus incident light. Rays from the axicon converge and creates a cone of light [140]. The Bessel beam propagation distance can be calculated using

$$z_{max} \simeq \frac{w_0}{\alpha}, \tag{5.3}$$

where w_0 is the beam waist of the incident beam and α is the physical angle of the cone in the axicon.

Figure 5.22 displays the intensity profile along one axis of a simple Bessel beam setup using a 20° axicon to generate a Bessel beam before a 20x objective lens is used for imaging onto a CCD camera. The central peak represents the core of the Bessel beam and is fitted using a Gaussian function, yielding a FWHM diameter of $3.9 \pm 0.3\,\mu m$. For an initial collimated beam diameter of 8 mm, the expected length of non-diffracting propagation is therefore 200 µm, representing a significant fraction of the current length of the waveguides in the Michelson interferometer arms. Replacing both waveguides with Bessel beams will provide interesting atom dynamics, may provide optimal splitting with minimised excitations and lead to new understanding of atom behaviour in the waveguides. However, it is important to note that due to the non-diffracting nature of the Bessel beam, it is multi-mode. Whilst it has been shown that a single Bessel beam is well suited for transporting atoms in a waveguide [141], it is less obvious that it will interfere and form a lattice with an identical second beam.

One goal of the project is to use several waveguides to create a closed loop interferometer as a tool for inertial sensing. To achieve this, four waveguides will be arranged in a square formation, with each waveguide overlapping the other. The BEC will be loaded into one arm of one waveguide, where it will be accelerated and split equally in the first beamsplitter. The two atom clouds will travel along separate arms before being completely reflected by a second beamsplitter. Finally, the two separate atom clouds are recombined, spatially and temporally separated from the first beamsplitter. The layout is known as a Mach-Zehnder interferometer and will be sensitive to rotation. A diagram example is shown in Figure 5.23.

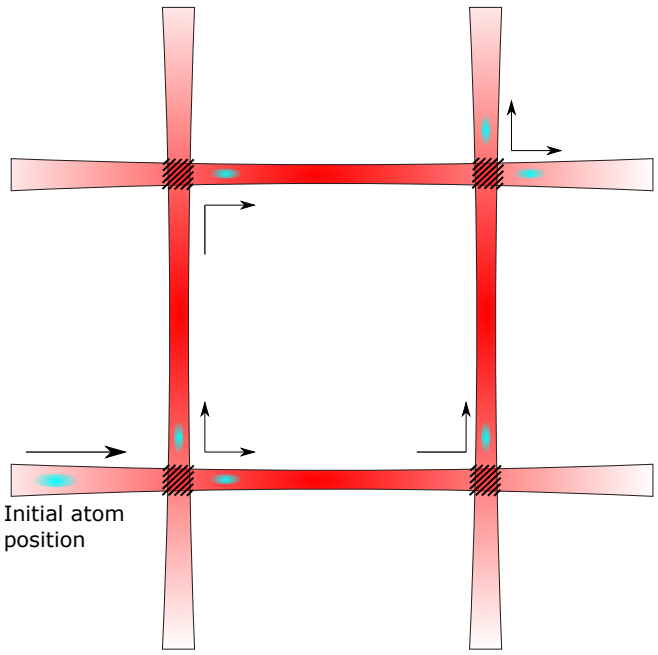

Fig. 5.23 A diagram to show the layout of waveguides required to create a Mach-Zehnder interferometer. The first interference region will split the atoms equally between the first two waveguides. The next beamsplitter will reflect the entire cloud, allowing both clouds to recombine at the final intersection.

5.8 Conclusions

A Michelson interferometer was chosen as the simplest method to test for signs of interference as only two waveguides are required. Reflection of the clouds after splitting in the lattice was achieved using magnetic field gradients from coils. One of the coils responsible for reflecting atoms in WG1 is also used as part of a pair to form the anti-Helmholtz field needed to generate a MOT. For this reason, the coils are not well aligned to the axes of the waveguides and excites the atoms in the radial direction.

Upon recombination, a clear sinusoidal oscillation of the atomic momentum between the two output ports is visible which is not present when the cloud is split initially. The returning atoms are analysed by measuring the flux of atoms exiting the splitter in one waveguide relative to the other. The results show a strong oscillatory signal. However, the frequency of the signal agrees well with the measured radial frequency of the waveguides. This indicates that the large excitations created by the off-axis coils are giving atoms a velocity component in the radial direction.

Planned upgrades to remove the reliance on magnetic fields to accelerate atoms in the waveguide will help to reduce these effects. The use of blue detuned beams to act as potential barriers has the additional benefit of permitting any angle between the two waveguides to be considered, as the axes of the coils are no longer important. In addition, the length of the interferometer arms can be significantly reduced to reduce the possibility of excitations. Furthermore, the length of each arm can be tuned to a far greater degree of accuracy. However, point instability of the beams is expected to be a constraining parameter and techniques to minimise the effect using motorised mirror mounts are actively being explored. The effect of introducing the blue detuned beams will open up new configurations that provide favourable splitting and recombination conditions.

Chapter 6

Summary

The aim of this work was to develop a novel method of coherently splitting and recombining a cloud of ultra-cold ^{87}Rb atoms in a BEC using optical waveguides. During the course of my PhD significant progress has been made, with major upgrades applied to virtually all areas of the experiment along with new techniques developed for trapping atoms. A major milestone within the experiment was the all optical production of a BEC, only made possible by the aforementioned upgrades. In particular, upgrades to the sequencing system allowed for greater control over the experiment via the introduction of a variable time resolution and new NI PXI cards all synced to the same high resolution clock.

The achievement of developing a BEC also relied on increasing the number of atoms trapped in the MOT, which was performed by creating MOT outcouplers. These are fibre coupled with minimal optics, aligned in a lens tube system to minimise deformations and preserve the Gaussian wavefront. It was also necessary to introduce new lasers such as the replacement cooling laser which provides close to 10 times the power of the original using a built in tapered amplifier. The replacement laser used to create the repumper light was also a significant upgrade over the original, which relied on a master and slave configuration requiring regular realignment and operated at a lower power. Increased power in both lasers allowed the new MOT outcouplers to feature larger diameter beams, increasing the total illuminated area and number of trapped atoms.

The introduction of crossed optical waveguides introduced a novel method of splitting a cloud of atoms using an optical lattice created from interference between two tightly focused dipole beams. Releasing a BEC in the waveguide up one Rayleigh length from the focus

results in the BEC being accelerated towards the focus owing to the shape of the potential. Upon reaching the centre, an intersecting identical waveguide creates a lattice of controllable amplitude which was adjusted to split the cloud equally into each waveguide. The velocity of the cloud is a critical factor in the probability that an atom will be reflected or transmitted. It is controlled by moving the position of the waveguide focus relative to the BEC, with a greater distance indicating a higher velocity. Introduction of magnetic acceleration through use of the 3D MOT coils helped to accelerate atoms to greater velocities. An additional advantage of using magnetic acceleration is that the waveguide focus can be stationary, with the atoms trapped well within one Rayleigh length from the focus. Unfortunately due to the imperfect alignment between the magnetic coil and the waveguide, a small excitation was created causing atoms to oscillate within the waveguide. A modification to the experiment to remove the reliance on magnetic acceleration has been proposed and is currently being implemented. A cloud of atoms condensed into a BEC can be split in a controlled manner into two separate optical waveguides. Interesting dynamics were observed as atoms traversed the intersection region and were continually reflected by the lattice in the form of quasi-momentum peaks. These represent the discrete energy steps atoms are gaining in order to be reflected into WG2 and are only populated when the confining potential is removed rapidly whilst atoms are present in the lattice.

Once the dynamics of atoms in the splitter were well understood, the first attempts at creating an interferometer were made. A Michelson configuration was chosen for its simplicity, requiring no additional optical waveguides or lattices. Atoms are instead split equally along two separate waveguides before their velocity is inverted, and they recombine at the original lattice. Magnetic field gradients were used to decelerate the atoms after all had passed through the splitter. A single coil from the 3D MOT is used to decelerate atoms that remain in WG1, whilst an additional coil was implemented to return atoms reflected into WG2. As observed when accelerating the initial BEC, small excitations are imparted on the atoms owing to the imperfect alignment of the magnetic field gradient. However, the initial results show promise, with a clear segmentation of the returning cloud as it periodically favours one waveguide over the other.

Planned upgrades to the current apparatus are focused on removing sources of noise, the most notable arising from the use of magnetic field gradients to accelerate atoms in the waveguides. Plans to implement a counter-propagating beam to accelerate atoms using a moving standing wave are being implemented. A new method to reflect atoms using blue detuned light to act as a repulsive barrier is also under consideration and will further remove reliance on

magnetic field gradients. Additional plans to introduce more waveguides to implement a closed-loop interferometer such as in a Mach-Zehnder configuration are also required to start using the experiment as an inertial sensor.

References

[1] A. A. Michelson and E. W. Morley. On the Relative Motion of the Earth and of the Luminiferous Ether. *Sidereal Messenger, vol. 6, pp.306-310*, 6:306–310, November 1887.

[2] B. P. Abbott, R. Abbott, T. D. Abbott, M. R. Abernathy, F. Acernese, K. Ackley, C. Adams, T. Adams, P. Addesso, R. X. Adhikari, and et al. Observation of Gravitational Waves from a Binary Black Hole Merger. *Physical Review Letters*, 116(6):061102, February 2016.

[3] P. G. Merli, G. F. Missiroli, and G. Pozzi. On the statistical aspect of electron interference phenomena. *American Journal of Physics*, 44:306–307, March 1976.

[4] R. Colella, A. W. Overhauser, and S. A. Werner. Observation of Gravitationally Induced Quantum Interference. *Physical Review Letters*, 34:1472–1474, June 1975.

[5] D. W. Keith, C. R. Ekstrom, Q. A. Turchette, and D. E. Pritchard. An interferometer for atoms. *Physical Review Letters*, 66:2693–2696, May 1991.

[6] A. D. Cronin, J. Schmiedmayer, and D. E. Pritchard. Optics and interferometry with atoms and molecules. *Reviews of Modern Physics*, 81:1051–1129, July 2009.

[7] S. Truppe, H. J. Williams, M. Hambach, L. Caldwell, N. J. Fitch, E. A. Hinds, B. E. Sauer, and M. R. Tarbutt. Molecules cooled below the doppler limit. *Nature Physics*, Aug 2017.

[8] S. Chu. Nobel Lecture: The manipulation of neutral particles. *Reviews of Modern Physics*, 70:685–706, July 1998.

[9] W. D. Phillips. Nobel Lecture: Laser cooling and trapping of neutral atoms. *Reviews of Modern Physics*, 70:721–741, July 1998.

[10] L. Essen and J. V. L. Parry. An Atomic Standard of Frequency and Time Interval: A Cæsium Resonator. *Natu*, 176:280–282, August 1955.

[11] N. F. Ramsey. A Molecular Beam Resonance Method with Separated Oscillating Fields. *Physical Review*, 78:695–699, June 1950.

[12] M. Kasevich and S. Chu. Measurement of the gravitational acceleration of an atom with a light-pulse atom interferometer. *Applied Physics B: Lasers and Optics*, 54:321–332, May 1992.

[13] F. Riehle, T. Kisters, A. Witte, J. Helmcke, and C. J. Borde. Optical Ramsey spectroscopy in a rotating frame - Sagnac effect in a matter-wave interferometer. *Physical Review Letters*, 67:177–180, July 1991.

[14] A. Lenef, T. D. Hammond, E. T. Smith, M. S. Chapman, R. A. Rubenstein, and D. E. Pritchard. Rotation Sensing with an Atom Interferometer. *Physical Review Letters*, 78:760–763, February 1997.

[15] T. L. Gustavson, P. Bouyer, and M. A. Kasevich. Precision Rotation Measurements with an Atom Interferometer Gyroscope. *Physical Review Letters*, 78:2046–2049, March 1997.

[16] P. Haslinger, N. Dörre, P. Geyer, J. Rodewald, S. Nimmrichter, and M. Arndt. A universal matter-wave interferometer with optical ionization gratings in the time domain. *Nature Physics*, 9:144–148, March 2013.

[17] W. Chaibi, R. Geiger, B. Canuel, A. Bertoldi, A. Landragin, and P. Bouyer. Low frequency gravitational wave detection with ground-based atom interferometer arrays. *PRD*, 93(2):021101, January 2016.

[18] Theodore H. Maiman et al. Stimulated optical radiation in ruby. *Nature*, 1960.

[19] Arthur Ashkin. Trapping of atoms by resonance radiation pressure. *Physical Review Letters*, 40(12):729, 1978.

[20] David J. Wineland, Robert E. Drullinger, and Fred L. Walls. Radiation-pressure cooling of bound resonant absorbers. *Physical Review Letters*, 40(25):1639, 1978.

[21] V. I. Balykin, V. S. Letokhov, and V. I. Mushin. Observation of the cooling of free sodium atoms in a resonance laser field with a scanning frequency. *JETP lett*, 29(10):560–564, 1979.

[22] William D. Phillips and Harold Metcalf. Laser deceleration of an atomic beam. *Physical Review Letters*, 48(9):596, 1982.

[23] Paul D. Lett, Richard N. Watts, Christoph I. Westbrook, William D. Phillips, Phillip Gould, and Harold J. Metcalf. Observation of atoms laser cooled below the doppler limit. *Physical review letters*, 61(2):169, 1988.

[24] S. Chu, L. Hollberg, J. E. Bjorkholm, A. Cable, and A. Ashkin. Three-dimensional viscous confinement and cooling of atoms by resonance radiation pressure. *Physical Review Letters*, 55:48–51, July 1985.

[25] D. E. Pritchard. Cooling Neutral Atoms in a Magnetic Trap for Precision Spectroscopy. *Physical Review Letters*, 51:1336–1339, October 1983.

[26] E. L. Raab, M. Prentiss, A. Cable, S. Chu, and D. E. Pritchard. Trapping of neutral sodium atoms with radiation pressure. *Physical Review Letters*, 59:2631–2634, December 1987.

[27] R. J. Cook. Atomic motion in resonant radiation: An application of Ehrenfest's theorem. *PRA*, 20:224–228, July 1979.

[28] S. Chu, J. E. Bjorkholm, A. Ashkin, and A. Cable. Experimental observation of optically trapped atoms. *Physical Review Letters*, 57:314–317, July 1986.

[29] J. D. Miller, R. A. Cline, and D. J. Heinzen. Far-off-resonance optical trapping of atoms. *Physical Review Letters*, 47:R4567–R4570, June 1993.

[30] W. Alt, D. Schrader, S. Kuhr, M. Müller, V. Gomer, and D. Meschede. Single atoms in a standing-wave dipole trap. *Physical Review Letters*, 67(3):033403, March 2003.

[31] M. D. Barrett, J. A. Sauer, and M. S. Chapman. All-Optical Formation of an Atomic Bose-Einstein Condensate. *Physical Review Letters*, 87(1):010404, July 2001.

[32] Satyendra Nath Bose. Plancks gesetz und lichtquantenhypothese. 1924.

[33] Albert Einstein. *Quantentheorie des einatomigen idealen Gases*, volume 20. 1924.

[34] Fritz London. The λ-phenomenon of liquid helium and the Bose-Einstein degeneracy. *Nature*, 141(3571):643, 1938.

[35] N. Bogoliubov. On the theory of superfluidity. *J. Phys*, 11(1):23, 1947.

[36] Mike H. Anderson, Jason R. Ensher, Michael R. Matthews, Carl E. Wieman, Eric A. Cornell, et al. Observation of Bose-Einstein condensation in a dilute atomic vapor. *science*, 269(5221):198–201, 1995.

[37] Kendall B. Davis, M-O. Mewes, Michael R. Andrews, N.J. Van Druten, D.S. Durfee, D.M. Kurn, and W. Ketterle. Bose-Einstein condensation in a gas of sodium atoms. *Physical review letters*, 75(22):3969, 1995.

[38] Dale G. Fried, Thomas C. Killian, Lorenz Willmann, David Landhuis, Stephen C. Moss, Daniel Kleppner, and Thomas J. Greytak. Bose-Einstein condensation of atomic hydrogen. *Physical Review Letters*, 81(18):3811, 1998.

[39] C.C. Bradley, C.A. Sackett, J.J. Tollett, and R.G. Hulet. Evidence of Bose-Einstein condensation in an atomic gas with attractive interactions. *Physical Review Letters*, 75(9):1687, 1995.

[40] Giacomo Roati, Matteo Zaccanti, C. D'Errico, Jacopo Catani, Michele Modugno, Andrea Simoni, Massimo Inguscio, and G. Modugno. K 39 Bose-Einstein condensate with tunable interactions. *Physical review letters*, 99(1):010403, 2007.

[41] Yosuke Takasu, Kenichi Maki, Kaduki Komori, Tetsushi Takano, Kazuhito Honda, Mitsutaka Kumakura, Tsutomu Yabuzaki, and Yoshiro Takahashi. Spin-singlet Bose-Einstein condensation of two-electron atoms. *Physical Review Letters*, 91(4):040404, 2003.

[42] Simon Stellmer, Meng Khoon Tey, Bo Huang, Rudolf Grimm, and Florian Schreck. Bose-Einstein condensation of strontium. *Physical review letters*, 103(20):200401, 2009.

[43] Seiji Sugawa, Rekishu Yamazaki, Shintaro Taie, and Yoshiro Takahashi. Bose-Einstein condensate in gases of rare atomic species. *Physical Review A*, 84(1):011610, 2011.

[44] Markus Greiner, Cindy A. Regal, and Deborah S. Jin. Emergence of a molecular Bose–Einstein condensate from a fermi gas. *Nature*, 426(6966):537, 2003.

[45] Immanuel Bloch, Theodor W. Hänsch, and Tilman Esslinger. Atom laser with a cw output coupler. *Physical Review Letters*, 82(15):3008, 1999.

[46] Edward W. Hagley, Lu Deng, M. Kozuma, J. Wen, Kristian Helmerson, S.L. Rolston, , and William D. Phillips. A well-collimated quasi-continuous atom laser. *Science*, 283(5408):1706–1709, 1999.

[47] Kevin Henderson, Changhyun Ryu, Calum MacCormick, and M.G. Boshier. Experimental demonstration of painting arbitrary and dynamic potentials for Bose–Einstein condensates. *New Journal of Physics*, 11(4):043030, 2009.

[48] S. Gupta, K.W. Murch, K.L. Moore, T.P. Purdy, and D.M. Stamper-Kurn. Bose-Einstein condensation in a circular waveguide. *Physical review letters*, 95(14):143201, 2005.

[49] T.L. Gustavson, A. Landragin, and M.A. Kasevich. Rotation sensing with a dual atom-interferometer sagnac gyroscope. *Classical and Quantum Gravity*, 17(12):2385, 2000.

[50] H. Müntinga, H. Ahlers, M. Krutzik, A. Wenzlawski, S. Arnold, D. Becker, K. Bongs, H. Dittus, H. Duncker, N. Gaaloul, et al. Interferometry with Bose-Einstein condensates in microgravity. *Physical review letters*, 110(9):093602, 2013.

[51] M.D. Lachmann, H. Ahlers, D. Becker, S.T. Seidel, T. Wendrich, and W. Rasel, E.M.and Ertmer. Creating the first Bose-Einstein condensate in space. In *Complex Light and Optical Forces XII*, volume 10549, page 1054909. International Society for Optics and Photonics, 2018.

[52] Mateusz Ernest Zawadzki, P. F. Griffin, Erling Riis, and A. S. Arnold. Spatial interference from well-separated split condensates. *Physical Review A*, 81(4):043608, 2010.

[53] R. J. Sewell, J. Dingjan, F. Baumgärtner, I. Llorente-Garcia, S. Eriksson, Edward A. Hinds, G. Lewis, Prasanna Srinivasan, Zakaria Moktadir, Carsten O. Gollasch, et al. Atom chip for bec interferometry. *Journal of Physics B: Atomic, Molecular and Optical Physics*, 43(5):051003, 2010.

[54] L. Marton. Electron interferometer. *Physical Review*, 85(6):1057, 1952.

[55] G. Möllenstedt and H. Düker. Beobachtungen und messungen an biprisma-interferenzen mit elektronenwellen. *Zeitschrift für Physik*, 145(3):377–397, 1956.

[56] H. Maier-Leibnitz and T. Springer. Ein interferometer für langsame neutronen. *Zeitschrift für Physik*, 167(4):386–402, 1962.

[57] Saul Altshuler and Lee Frantz. Matter wave interferometric apparatus, September 25 1973. US Patent 3,761,721.

[58] David W. Keith, Christopher R. Ekstrom, Quentin A. Turchette, and David E. Pritchard. An interferometer for atoms. *Physical review letters*, 66(21):2693, 1991.

[59] Peter W. Graham, Jason M. Hogan, Mark A. Kasevich, and Surjeet Rajendran. Resonant mode for gravitational wave detectors based on atom interferometry. *Physical Review D*, 94(10):104022, 2016.

[60] D.N. Aguilera, H. Ahlers, B. Battelier, A. Bawamia, A. Bertoldi, R. Bondarescu, K. Bongs, P. Bouyer, C. Braxmaier, L. Cacciapuoti, et al. Ste-quest—test of the universality of free fall using cold atom interferometry. *Classical and Quantum Gravity*, 31(11):115010, 2014.

[61] G. Rosi, F. Sorrentino, L. Cacciapuoti, M. Prevedelli, and G.M. Tino. Precision measurement of the newtonian gravitational constant using cold atoms. *Nature*, 510(7506):518, 2014.

[62] Y. Bidel, N. Zahzam, C. Blanchard, A. Bonnin, M. Cadoret, A. Bresson, D. Rouxel, and M.F. Lequentrec-Lalancette. Absolute marine gravimetry with matter-wave interferometry. *Nature communications*, 9(1):627, 2018.

[63] Bess Fang, Indranil Dutta, Pierre Gillot, Denis Savoie, Jean Lautier, Bing Cheng, C.L. Garrido Alzar, Remi Geiger, Sebastien Merlet, F. Pereira Dos Santos, et al. Metrology with atom interferometry: inertial sensors from laboratory to field applications. In *Journal of Physics: Conference Series*, volume 723, page 012049. IOP Publishing, 2016.

[64] W. Ketterle. Nobel lecture: When atoms behave as waves: Bose-Einstein condensation and the atom laser. *Reviews of Modern Physics*, 74:1131–1151, November 2002.

[65] Dominik Schneble, Masahiro Hasuo, Thomas Anker, Tilman Pfau, and Jürgen Mlynek. Integrated atom-optical circuit with continuous-wave operation. *JOSA B*, 20(4):648–651, 2003.

[66] Changhyun Ryu and Malcolm Geoffrey Boshier. Integrated coherent matter wave circuits. *New Journal of Physics*, 17(9):092002, 2015.

[67] O. Garcia, B. Deissler, K.J. Hughes, J.M. Reeves, and C.A. Sackett. Bose-Einstein-condensate interferometer with macroscopic arm separation. *Physical Review A*, 74(3):031601, 2006.

[68] Dirk Müller, Eric A. Cornell, Marco Prevedelli, Peter D.D. Schwindt, Alex Zozulya, and Dana Z. Anderson. Waveguide atom beam splitter for laser-cooled neutral atoms. *Optics letters*, 25(18):1382–1384, 2000.

[69] M.A. Ol'Shanii, Y.B. Ovchinnikov, and V.S. Letokhov. Laser guiding of atoms in a hollow optical fiber. *Optics communications*, 98(1-3):77–79, 1993.

[70] Michael J. Renn, D. Montgomery, O. Vdovin, D.Z. Anderson, C.E. Wieman, and E.A. Cornell. Laser-guided atoms in hollow-core optical fibers. *Physical review letters*, 75(18):3253, 1995.

[71] Giovanni Luca Gattobigio, Antoine Couvert, Gael Reinaudi, Bertrand Georgeot, and David Guéry-Odelin. Optically guided beam splitter for propagating matter waves. *Physical review letters*, 109(3):030403, 2012.

[72] V. Guarrera, R. Moore, A. Bunting, T. Vanderbruggen, and Y.B. Ovchinnikov. Distributed quasi-bragg beam splitter in crossed atomic waveguides. *Scientific Reports*, 7(1):4749, 2017.

[73] Ron Folman, Peter Krüger, Donatella Cassettari, Björn Hessmo, Thomas Maier, and Jörg Schmiedmayer. Controlling cold atoms using nanofabricated surfaces: atom chips. *Physical Review Letters*, 84(20):4749, 2000.

[74] Y.B. Ovchinnikov. Beam splitters. Patent, December 2015. https://www.ipo.gov.uk/p-ipsum/Case/PublicationNumber/GB2527148.

[75] V. S. Letokhov, V. G. Minogin, and B. D. Pavlik. Cooling and capture of atoms and molecules by a resonant light field. *Soviet Journal of Experimental and Theoretical Physics*, 45:698, 1977.

[76] Rubidium 87 d line data. http://steck.us/alkalidata/. Accessed 23-Oct-2017.

[77] J. Dalibard and C. Cohen-Tannoudji. Dressed-atom approach to atomic motion in laser light: the dipole force revisited. *JOSA B*, 2(11):1707–1720, 1985.

[78] Jean Dalibard and Claude Cohen-Tannoudji. Laser cooling below the doppler limit by polarization gradients: simple theoretical models. *JOSA B*, 6(11):2023–2045, 1989.

[79] Alan L. Migdall, John V. Prodan, William D. Phillips, Thomas H. Bergeman, and Harold J. Metcalf. First observation of magnetically trapped neutral atoms. *Physical Review Letters*, 54(24):2596, 1985.

[80] R. Grimm, M. Weidemüller, and Y. B. Ovchinnikov. Optical Dipole Traps for Neutral Atoms. *Advances in Atomic Molecular and Optical Physics*, 42:95–170, 2000.

[81] L. Allen and J. H. Eberly. *Optical resonance and two-level atoms*. Dover, 1987.

[82] Christopher J Foot et al. *Atomic physics*, volume 7. Oxford University Press, 2005.

[83] Roee Ozeri, Lev Khaykovich, and Nir Davidson. Long spin relaxation times in a single-beam blue-detuned optical trap. *Physical Review A*, 59(3):R1750, 1999.

[84] Takahiro Kuga, Yoshio Torii, Noritsugu Shiokawa, Takuya Hirano, Yukiko Shimizu, and Hiroyuki Sasada. Novel optical trap of atoms with a doughnut beam. *Physical Review Letters*, 78(25):4713, 1997.

[85] Jianping Yin, Yifu Zhu, and Yuzhu Wang. Gravito-optical trap for cold atoms with doughnut-hollow-beam cooling. *Physics Letters A*, 248(5-6):309–318, 1998.

[86] Y. B. Ovchinnikov, I. Manek, A. I. Sidorov, G. Wasik, and R. Grimm. Gravito-optical atom trap based on a conical hollow beam. *EPL (Europhysics Letters)*, 43(5):510, 1998.

[87] Caleb A. Christensen, Sebastian Will, Michele Saba, Gyu-Boong Jo, Yong-Il Shin, Wolfgang Ketterle, and David Pritchard. Trapping of ultracold atoms in a hollow-core photonic crystal fiber. *PHYSICAL REVIEW A Phys Rev A*, 78:033429, 2008.

[88] Michal Bajcsy, S. Hofferberth, Thibault Peyronel, Vlatko Balic, Qiangrong Liang, A. S. Zibrov, Vladan Vuletic, and Mikhail D. Lukin. Laser-cooled atoms inside a hollow-core photonic-crystal fiber. *Physical Review A*, 83(6):063830, 2011.

[89] Y. B. Ovchinnikov, S. V. Shul'ga, and V. I. Balykin. An atomic trap based on evanescent light waves. *Journal of Physics B: Atomic, Molecular and Optical Physics*, 24(14):3173, 1991.

[90] Jonathan P. Dowling and Julio Gea-Banacloche. Evanescent light-wave atom mirrors, resonators, waveguides, and traps. In *Advances in atomic, molecular, and optical physics*, volume 37, pages 1–94. Elsevier, 1996.

[91] E. Vetsch, D. Reitz, G. Sagué, R. Schmidt, S. T. Dawkins, and A. Rauschenbeutel. Optical interface created by laser-cooled atoms trapped in the evanescent field surrounding an optical nanofiber. *Physical review letters*, 104(20):203603, 2010.

[92] C. S. Adams, H. J. Lee, N. Davidson, M. Kasevich, and S. Chu. Evaporative Cooling in a Crossed Dipole Trap. *Physical Review Letters*, 74:3577–3580, May 1995.

[93] VS Letokhov. Narrowing of the doppler width in a standing wave. *ZhETF Pisma Redaktsiiu*, 7:348, 1968.

[94] Vladan Vuletić, Cheng Chin, Andrew J. Kerman, and Steven Chu. Degenerate raman sideband cooling of trapped cesium atoms at very high atomic densities. *Physical Review Letters*, 81(26):5768, 1998.

[95] Isaac F. Silvera. Bose–einstein condensation. *American Journal of Physics*, 65(6):570–574, 1997.

[96] P. Schuck and X. Viñas. Thomas-fermi approximation for Bose-Einstein condensates in traps. *Physical Review A*, 61(4), Aug 2000.

[97] F. Dalfovo, S. Giorgini, L. P. Pitaevskii, and S. Stringari. Theory of Bose-Einstein condensation in trapped gases. *Reviews of Modern Physics*, 71:463–512, April 1999.

[98] Wolfgang Petrich, Michael H. Anderson, Jason R. Ensher, and Eric A. Cornell. Stable, tightly confining magnetic trap for evaporative cooling of neutral atoms. *Physical Review Letters*, 74(17):3352, 1995.

[99] M-O. Mewes, M. R. Andrews, N. J. Van Druten, D. M. Kurn, D. S. Durfee, and W. Ketterle. Bose-einstein condensation in a tightly confining dc magnetic trap. *Physical Review Letters*, 77(3):416, 1996.

[100] Z. T. Lu, K. L. Corwin, M. J. Renn, M. H. Anderson, E. A. Cornell, and C. E. Wieman. Low-velocity intense source of atoms from a magneto-optical trap. *Physical review letters*, 77(16):3331, 1996.

[101] T. W. Hänsch, I. S. Shahin, and A. L. Schawlow. High-resolution saturation spectroscopy of the sodium d lines with a pulsed tunable dye laser. *Physical Review Letters*, 27(11):707, 1971.

[102] D. W. Preston. Doppler-free saturated absorption: Laser spectroscopy. *American Journal of Physics*, 64:1432–1436, November 1996.

[103] Yuri Ovchinnikov and Giuseppe Marra. Accurate rubidium atomic fountain frequency standard. *Metrologia*, 48(3):87, 2011.

[104] Y. B. Ovchinnikov. Compact magneto-optical sources of slow atoms. *Optics Communications*, 249:473–481, May 2005.

[105] Aviv Keshet. Cicero word generator. http://akeshet.github.io/Cicero-Word-Generator/. Accessed 09-Feb-2018.

[106] W. Ketterle, K. B. Davis, M. A. Joffe, A. Martin, and D. E. Pritchard. High densities of cold atoms in a dark spontaneous-force optical trap. *Physical Review Letters*, 70:2253–2256, April 1993.

[107] N. Schlosser, G. Reymond, I. Protsenko, and P. Grangier. Sub-poissonian loading of single atoms in a microscopic dipole trap. *Nature*, 411:1024–1027, June 2001.

[108] W. Neuhauser, M. Hohenstatt, P. E. Toschek, and H. Dehmelt. Localized visible Ba^+ mono-ion oscillator. *Physical Review Letters*, 22:1137–1140, September 1980.

[109] J. Szczepkowski, R. Gartman, M. Witkowski, L. Tracewski, M. Zawada, and W. Gawlik. Analysis and calibration of absorptive images of Bose-Einstein condensate at nonzero temperatures. *Review of Scientific Instruments*, 80(5):053103–053103–7, May 2009.

[110] Fabrice Gerbier, Joseph H. Thywissen, Simon Richard, Mathilde Hugbart, Philippe Bouyer, and Alain Aspect. Critical temperature of a trapped, weakly interacting Bose gas. *Physical review letters*, 92(3):030405, 2004.

[111] E. A. Cornell, J. R. Ensher, and C. E. Wieman. *Experiments in dilute atomic Bose-Einstein condensation*, pages 533–584. World Scientific Publishing Co, 2008.

[112] K. J. Åström and T. Hägglund. Automatic tuning of simple regulators for phase and amplitude margins specifications. *Adaptive Systems in Control and Signal Processing 1983*, page 271–276, Nov 1984.

[113] J. G. Ziegler and N. B. Nichols. Optimum settings for automatic controllers. *Transactions of the ASM*, 64:759,768, Nov 1942.

[114] M. D. Barrett, J. A. Sauer, and M. S. Chapman. All-optical formation of an atomic Bose-Einstein condensate. *Physical Review Letters*, 87(1):010404, 2001.

[115] A. J. Olson, R. J. Niffenegger, and Y. P. Chen. Optimizing the efficiency of evaporative cooling in optical dipole traps. *PRA*, 87(5):053613, May 2013.

[116] W. Ketterle and N. J. V. Druten. Evaporative Cooling of Trapped Atoms. *Advances in Atomic Molecular and Optical Physics*, 37:181–236, 1996.

[117] Krzysztof Gawryluk, Mirosław Brewczyk, Mariusz Gajda, and Kazimierz Rzążewski. Free expansion of a bose–einstein condensate in the presence of a thermal cloud. *Journal of Physics B: Atomic, Molecular and Optical Physics*, 43(10):105303, 2010.

[118] P. D. Lett, W. D. Phillips, S. L. Rolston, C. E. Tanner, R. N. Watts, and C. I. Westbrook. Optical molasses. *Journal of the Optical Society of America B Optical Physics*, 6:2084–2107, November 1989.

[119] A. Vorozcovs, M. Weel, S. Beattie, S. Cauchi, and A. Kumarakrishnan. Measurements of temperature scaling laws in an optically dense magneto-optical trap. *Journal of the Optical Society of America B Optical Physics*, 22:943–950, May 2005.

[120] Tino Weber, Jens Herbig, Michael Mark, Hanns-Christoph Nägerl, and Rudolf Grimm. Bose-Einstein condensation of cesium. *Science*, 299(5604):232–235, 2003.

[121] Toshiya Kinoshita, Trevor Wenger, and David S. Weiss. All-optical Bose-Einstein condensation using a compressible crossed dipole trap. *Physical Review A*, 71(1):011602, 2005.

[122] W. L. Bragg. The diffraction of x-rays by crystals. In *Proc. Cambridge Philos. Soc.*, volume 17, page 43, 1912.

[123] R. Frisch. Experimenteller nachweis des Einsteinschen strahlungsrückstoßes. *Zeitschrift für Physik A Hadrons and Nuclei*, 86(1):42–48, 1933.

[124] Peter J. Martin, Bruce G. Oldaker, Andrew H. Miklich, and David E. Pritchard. Bragg scattering of atoms from a standing light wave. *Physical review letters*, 60(6):515, 1988.

[125] Phillip L. Gould, George A. Ruff, and David E. Pritchard. Diffraction of atoms by light: The near-resonant kapitza-dirac effect. *Physical review letters*, 56(8):827, 1986.

[126] Neil W. Ashcroft, N. David Mermin, and Sergio Rodriguez. Solid state physics, 1978.

[127] Felix Bloch. Über die quantenmechanik der elektronen in kristallgittern. *Zeitschrift für physik*, 52(7-8):555–600, 1929.

[128] J. C. Slater. A soluble problem in energy bands. *Physical Review*, 87(5):807, 1952.

[129] G. D. McDonald, Hannah Keal, P. A. Altin, J. E. Debs, Shayne Bennetts, C. C. N. Kuhn, K. S. Hardman, M. T. Johnsson, J. D. Close, and N. P. Robins. Optically guided linear mach-zehnder atom interferometer. *Physical Review A*, 87(1):013632, 2013.

[130] F. Damon, G. Condon, P. Cheiney, A. Fortun, B. Georgeot, J. Billy, and D. Guéry-Odelin. Band-gap structures for matter waves. *PRA*, 92(3):033614, September 2015.

[131] Immanuel Bloch. Ultracold quantum gases in optical lattices. *Nature Physics*, 1(1):23, 2005.

[132] C. Keller, J. Schmiedmayer, A. Zeilinger, T. Nonn, S. Dürr, and G. Rempe. Adiabatic following in standing-wave diffraction of atoms. *Applied Physics B: Lasers and Optics*, 69:303–309, October 1999.

[133] H. Müller, S. W. Chiow, and S. Chu. Atom-wave diffraction between the Raman-Nath and the Bragg regime: Effective Rabi frequency, losses, and phase shifts. *Physical Review Letters*, 77(2):023609, February 2008.

[134] C. Keller, J. Schmiedmayer, A. Zeilinger, T. Nonn, S. Dürr, and G. Rempe. Adiabatic following in standing-wave diffraction of atoms. *Applied Physics B*, 69(4):303–309, 1999.

[135] Holger Müller, Sheng-wey Chiow, and Steven Chu. Atom-wave diffraction between the Raman-Nath and the Bragg regime: Effective Rabi frequency, losses, and phase shifts. *Physical review A*, 77(2):023609, 2008.

[136] Mark Kasevich, David S. Weiss, Erling Riis, Kathryn Moler, Steven Kasapi, and Steven Chu. Atomic velocity selection using stimulated Raman transitions. *Physical review letters*, 66(18):2297, 1991.

[137] T. Kovachy, P. Asenbaum, C. A. Overstreet, C.and Donnelly, S. M. Dickerson, A. Sugarbaker, J. M. Hogan, and M. A. Kasevich. Quantum superposition at the half-metre scale. *Nature*, 528(7583):530, 2015.

[138] Renée Charrière, Malo Cadoret, Nassim Zahzam, Yannick Bidel, and Alexandre Bresson. Local gravity measurement with the combination of atom interferometry and Bloch oscillations. *Physical Review A*, 85(1):013639, 2012.

[139] Nir Davidson, Heun Jin Lee, Charles S. Adams, Mark Kasevich, and Steven Chu. Long atomic coherence times in an optical dipole trap. *Physical review letters*, 74(8):1311, 1995.

[140] D. McGloin and K. Dholakia. Bessel beams: diffraction in a new light. *Contemporary Physics*, 46(1):15–28, 2005.

[141] Jochen Arlt, T. Hitomi, and K. Dholakia. Atom guiding along Laguerre-Gaussian and Bessel light beams. *Applied Physics B*, 71(4):549–554, 2000.